

INFORMATION TO USERS

This manuscript has been reproduced from the microfilm master. UMI films the text directly from the original or copy submitted. Thus, some thesis and dissertation copies are in typewriter face, while others may be from any type of computer printer.

The quality of this reproduction is dependent upon the quality of the copy submitted. Broken or indistinct print, colored or poor quality illustrations and photographs, print bleedthrough, substandard margins, and improper alignment can adversely affect reproduction.

In the unlikely event that the author did not send UMI a complete manuscript and there are missing pages, these will be noted. Also, if unauthorized copyright material had to be removed, a note will indicate the deletion.

Oversize materials (e.g., maps, drawings, charts) are reproduced by sectioning the original, beginning at the upper left-hand corner and continuing from left to right in equal sections with small overlaps. Each original is also photographed in one exposure and is included in reduced form at the back of the book.

Photographs included in the original manuscript have been reproduced xerographically in this copy. Higher quality 6" x 9" black and white photographic prints are available for any photographs or illustrations appearing in this copy for an additional charge. Contact UMI directly to order.

UMI

A Bell & Howell Information Company
300 North Zeeb Road, Ann Arbor MI 48106-1346 USA
313/761-4700 800/521-0600



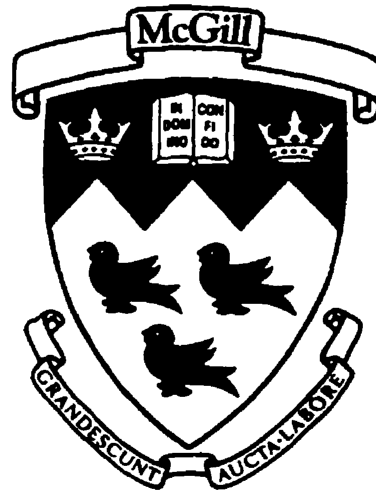
Proximity Sensor Network for Sensor Based Manipulation

John Damianakis

Department of Mechanical Engineering
McGill University, Montreal

April 1997

A Thesis submitted to the Faculty of Graduate Studies and Research in partial
fulfilment of the requirements of the degree of Master of Engineering



©John Damianakis 1997



National Library
of Canada

Acquisitions and
Bibliographic Services

395 Wellington Street
Ottawa ON K1A 0N4
Canada

Bibliothèque nationale
du Canada

Acquisitions et
services bibliographiques

395, rue Wellington
Ottawa ON K1A 0N4
Canada

Your file *Votre référence*

Our file *Notre référence*

The author has granted a non-exclusive licence allowing the National Library of Canada to reproduce, loan, distribute or sell copies of this thesis in microform, paper or electronic formats.

The author retains ownership of the copyright in this thesis. Neither the thesis nor substantial extracts from it may be printed or otherwise reproduced without the author's permission.

L'auteur a accordé une licence non exclusive permettant à la Bibliothèque nationale du Canada de reproduire, prêter, distribuer ou vendre des copies de cette thèse sous la forme de microfiche/film, de reproduction sur papier ou sur format électronique.

L'auteur conserve la propriété du droit d'auteur qui protège cette thèse. Ni la thèse ni des extraits substantiels de celle-ci ne doivent être imprimés ou autrement reproduits sans son autorisation.

0-612-29588-5

To my parents,
Stelios and Elefteria,
for their love and support

Abstract

A Proximity Sensor Network (PSN) consisting of four Infra-Red (IR) sensors was developed in order to track, grasp or manipulate objects with robots. The work is motivated by the need for local high bandwidth sensors at the robot's end effector to provide feedback during the pre-contact stage. Two types of amplitude based IR sensors were designed, an "Electrically Biased Sensor" (EBS) and a "Photon Biased Sensor" (PBS). The PBS sensor has a diameter of 5.55 mm and a range of approximately 9.0 cm . The EBS sensor has a diameter of 7.15 mm and a range of approximately 11.2 cm . Both sensors are robust and inexpensive since they were constructed using low-cost, off the shelf components. The design of the sensor heads, the signal processing electronics and the sensor characteristics will be discussed.

Résumé

Un réseau de capteurs de proximité (PSN) composé de quatre capteurs à l'infrarouge a été développé pour exécuter des tâches de poursuite, de préhension ou de manipulation avec un robot. Ce travail a été motivé par le besoin d'utiliser des capteurs locaux qui peuvent traiter des données rapidement et peuvent être placés au poignet du robot pour fournir une rétroaction pendant la phase de pré-contact. Deux types de capteurs d'intensité infrarouge ont été développés, des capteurs polarisés par la lumière infrarouge (PBS) et des capteurs polarisés électriquement (EBS). Les capteurs PBS ont un diamètre de 5.55 mm et une portée approximative de 9.0 cm . Les capteurs EBS ont un diamètre de 7.15 mm et une portée approximative de 11.2 cm . Les deux capteurs développés sont de construction robuste et peu dispendieux puisqu'ils sont fabriqués à partir de composants commerciaux. La conception des capteurs, l'électronique requise pour le traitement du signal et les caractéristiques des capteurs vont être discutés.

Acknowledgements

I would like to acknowledge the support of the *Fonds pour la Formation de Chercheurs et l'Aide à la Recherche* who made this work possible by granting me an FCAR B1 scholarship.

I would also like to thank a number of people who have helped me in some way put together this thesis. First, I would like to express my sincere gratitude to Gregory Petryk, who worked on the manipulation part of this project. Without his I/O code, this work would not have been possible. Also, Greg's urgency helped me focus on the critical tasks required to complete this project. I also would like to thank Mojtaba Ahmadi, although not a member of the Autonomous Manipulation Laboratory, he always stopped working to offer help. Gladys Ho and Eric Young were two undergraduate students who developed the HC11 code and were a great help with any problems concerning the HC11. I would like to thank my advisor Martin Buehler for having the vision to see this work through. His advice throughout the duration of this work proved to be invaluable. I would also like to thank Joey Mennitto for introducing me to Martin Buehler.

I would like to thank my wife Anna for providing the support at home that is necessary when working on such a project. I also would like to acknowledge the help of my brother Stefanos, who provided me with a great deal of software advice. My special thanks also goes out to the rest of my family, my parents, sister, niece and nephew for their love and support throughout my studies. Finally, I thank God for looking over me and providing me with patience and wisdom.

Contents

1	Introduction	1
1.1	Proximity Sensing	1
1.2	Historical Background	4
1.3	Progress at McGill	9
1.4	Author's contributions	9
1.5	Organization of the thesis	10
2	Proximity Sensor Technology	11
2.1	Triangulation Principle	12
2.2	Phase Modulation	13
2.3	Amplitude Modulation	15
3	Proximity Sensor Network	18
3.1	Sensor Requirements	18
3.2	Sensor Head Design	20
3.2.1	Photon Biased Sensor Head	22
3.2.2	Electron Biased Sensor Head	26
3.3	Driving Electronics	28
3.4	Signal Processing Electronics	31
3.4.1	Stage 2: Gain Scheduling	35
3.4.2	Stages Three to Five	37
3.5	HC11 Microcontroller	41

4	Experimental Results	46
4.1	Experimental Set-Up	46
4.2	Characterization Curves	49
4.2.1	Sensor Calibration	49
4.2.2	Data Fitting	50
4.3	Ambient Light and Biasing Effects	52
4.4	Modulating Frequency Effects	62
4.4.1	Effect on PSN Output	62
4.4.2	Effect on DC Output of Phototransistor	63
4.5	Object Size Effects	65
4.6	Lobe Size Determination	67
4.7	Signal Drift	68
5	Conclusions	71
A	Optek Data Sheets	73
A.1	73
A.2	75
A.3	77
A.4	79
A.5	81

List of Figures

2.1	The geometry of triangulation-based sensors. The distance of the object is a function of the distance travelled by the IR beam.	12
2.2	The geometry of a phase-based sensor. The distance of the object is a function of the phase difference between LED-a and the signal received by the photodiode.	14
2.3	The geometry of an amplitude-based sensor. The LED's emission cone and the phototransistor's receiving cone define the sensors usable region.	16
2.4	The bell shaped output curve of an AM sensor.	17
3.1	Response of the OPTTEK OP644SL phototransistor taken from the OPTTEK Technologies Data Book [10]	21
3.2	A PBS Sensor head and its three components, a modulated AC LED, a DC biasing LED and a phototransistor	23
3.3	A top view and side view of a PBS head.	24
3.4	A photo of three PBS sensor heads. The two outer ones have no outer aluminium tube.	26
3.5	An EBS Sensor which has four LEDs (AC) placed above a larger phototransistor.	26
3.6	A top view and side view of an EBS head.	27
3.7	Version 1 of the LED driving electronics implemented on the PSN board dedicated to the PBS heads.	29

3.8	Version 2 of the LED driving electronics implemented on the PSN board dedicated to the EBS heads.	30
3.9	The driving signal at the LED's anode for an EBS head using its signal processing electronics. This corresponds to point A in Fig. 3.8.	32
3.10	The driving signal at the LED's emitter for an EBS head using its signal processing electronics. This corresponds to point B in Fig. 3.8.	32
3.11	Signal processing electronics for phototransistor receiver.	33
3.12	The raw signal present at the emitter of the phototransistor. This corresponds to point 1 in Fig. 3.11.	34
3.13	The signal after $E1$ or point 2 in Fig. 3.11.	35
3.14	Sectioning the response curve of the sensor and assigning specific gains to each portion.	36
3.15	The state machine which determines the gain for each sensor.	36
3.16	The signal after $E2$ or point 3 in Fig. 3.11.	38
3.17	The signal after $E3$ or point 4 in Fig. 3.11.	40
3.18	The signal after the half-wave rectifier, point 5 in Fig. 3.11.	40
3.19	The signal after $E4$ or point 6 in Fig. 3.11.	41
3.20	HC11 input/output structure.	42
3.21	Main program flow structure.	43
3.22	Interrupt subroutine flow structure.	44
3.23	A photo of the PSN board (actual size).	45
4.1	Current experimental platform, a PPR actuated robot ("Calvin") and a unactuated RRR robot ("Hobbes"). Courtesy: G. Petryk.	47
4.2	Relationship between global and local sensor variables.	49

4.3 Raw data obtained from PBS sensor #1 (top). Fitted sensor output as a function of distance (middle left). Fitted sensor output as a function of orientation (middle right). Error in curve fitting raw data as a function of distance (bottom left). Error in curve fitting raw data as a function of orientation (bottom right). 53

4.4 Raw data obtained from PBS sensor #2 (top). Fitted sensor output as a function of distance (middle left). Fitted sensor output as a function of orientation (middle right). Error in curve fitting raw data as a function of distance (bottom left). Error in curve fitting raw data as a function of orientation (bottom right). 54

4.5 Raw data obtained from PBS sensor #3 (top). Fitted sensor output as a function of distance (middle left). Fitted sensor output as a function of orientation (middle right). Error in curve fitting raw data as a function of distance (bottom left). Error in curve fitting raw data as a function of orientation (bottom right). 55

4.6 Raw data obtained from PBS sensor #4 (top). Fitted sensor output as a function of distance (middle left). Fitted sensor output as a function of orientation (middle right). Error in curve fitting raw data as a function of distance (bottom left). Error in curve fitting raw data as a function of orientation (bottom right). 56

4.7 Raw data obtained from EBS sensor #1 (top). Fitted sensor output as a function of distance (middle left). Fitted sensor output as a function of orientation (middle right). Error in curve fitting raw data as a function of distance (bottom left). Error in curve fitting raw data as a function of orientation (bottom right). 57

4.8	Raw data obtained from EBS sensor #2 (top). Fitted sensor output as a function of distance (middle left). Fitted sensor output as a function of orientation (middle right). Error in curve fitting raw data as a function of distance (bottom left). Error in curve fitting raw data as a function of orientation (bottom right).	58
4.9	Raw data obtained from EBS sensor #3 (top). Fitted sensor output as a function of distance (middle left). Fitted sensor output as a function of orientation (middle right). Error in curve fitting raw data as a function of distance (bottom left). Error in curve fitting raw data as a function of orientation (bottom right).	59
4.10	Raw data obtained from EBS sensor #4 (top). Fitted sensor output as a function of distance (middle left). Fitted sensor output as a function of orientation (middle right). Error in curve fitting raw data as a function of distance (bottom left). Error in curve fitting raw data as a function of orientation (bottom right).	60
4.11	The effect of increasing the DC component of the collector current of the phototransistor on the sensor signal with an object maintained at a constant distance.	61
4.12	The effect of increasing the modulating frequency on the sensor with an object maintained at a constant distance.	63
4.13	The sensor at three different stages (a) at the LED (b) the theoretical signal returned by a diffuse surface (c) the signal measured by the phototransistor.	64
4.14	The DC offset of the raw signal for one PBS and one EBS sensor. . .	65
4.15	The effect of increasing the size of the object on the sensor output using one PBS sensor (left) and one EBS sensor (right).	66
4.16	The effect of sweeping across at a constant sensor-object distance for a PBS sensor (left) and an EBS sensor (right).	68

LIST OF FIGURES

4.17 The effect of drift on the sensor signal for PBS sensor #2 (left) and PBS sensor #3 (right).	69
4.18 The effect of drift on the sensor signal for EBS sensor #3 (left) and EBS sensor #4 (right).	69

Chapter 1

Introduction

1.1 Proximity Sensing

From the very start of robotics, the layman has envisioned robots to be fully autonomous and intelligent machines capable of mimicking himself. The engineer, however, struggled to perform even a simple task such as a pick and place operation. Today, this dream is closer to being realized, and the key to achieving a robot capable of interacting in an unknown environment is the development of satisfactory sensory information. Unfortunately, we are still at the point where a simple task such as juggling a ball still poses a challenge for the robot and the engineer.

Sensory information is critical for robots interacting with unknown environments, such as in space and deep-sea exploration where à priori knowledge of the environment is difficult to obtain. Operating a robot in space using teleoperation from a ground station to perform a delicate task such as turning a screw is rendered extremely difficult due to inherent time delays. Sensory feedback is also required for performing such tasks as precision robot assembly, surface following, collision avoidance and obstacle avoidance.

Local sensing, that is sensing the proximity between the robot gripper and an object in the 0 – 10 *cm* range, can be accomplished using infra-red (IR) proximity

sensors. Local sensing provides a means to reduce the signal bandwidth and increase the robot's accuracy and dextrous capabilities. The use of IR proximity sensors for collision avoidance and motion planning in unstructured environments is implemented and thoroughly discussed in [6].

Possible industrial applications of proximity sensors include manufacturing tasks such as lifting objects off a conveyer or from another robot, live-wire maintenance and satellite retrieval. Teleoperated robots are currently equipped with only global sensors such as cameras and haptic sensors such as force feedback sensors. Many operators have trouble during the pre-contact phase. Proximity sensors could be used to automate the grasping task once the operator positions the end-effector within a few centimetres of the object. This would reduce the time required to perform operations and reduce the skill level required by the operator.

Robots are able to function efficiently in a stationary environment but their performance in unstructured dynamic environments is still poor. The main problem encountered in dynamic environments is acquiring information about the changing surroundings fast enough to react to these changes. Dynamic grasping is a simple task which is a subset of many more complicated manoeuvres in a dynamic environment.

A smooth grasp of a moving object is a basic task that requires a dextrous robot equipped with accurate, high bandwidth sensors. Using low bandwidth sensors, such as cameras, significantly hinders the robot's tracking capabilities. A significant amount of research is being done on dynamic grasping using global sensors such as CCD cameras and laser range finders [14, 24, 19, 27, 26, 25, 1]. Cameras and laser range finders are quite large and also suffer from occlusion of the object. In order to tackle this problem, engineers attach the camera near the robot end-effector. Unfortunately, occlusion of the object is still a problem at certain robot poses. This occurs more frequently as the object approaches the robot end-effector. The pre-grasp stage is crucial to the success of the task. Not having access to sensory information at this

time poses a problem. Placing small IR sensors inside the robot's end effector will provide continuous information during this pre-contact stage.

The advantages of using active, amplitude based IR proximity sensors are that they are small, rugged, fast and inexpensive. The sensor is small since it is made of only two components, an LED and a receiver such as phototransistor or PIN diode. Both components are manufactured in packages as small as 1.57 mm in diameter. The components can be placed side by side, thus making it possible to build a sensor with an overall diameter of 5.55 mm . The sensors are rugged since there are no moving parts and no external mirrors or lenses. The sensor components are also very fast, operating in the 200 kHz to 5 MHz range. Finally, each component costs under $\$5\text{ US}$.

The sensor signal is a function of three parameters: sensor-object distance, angle between sensor beam and object surface and object surface properties such as colour and surface finish. The sensor signal is also sensitive to ambient light conditions. As a result, the use of such sensors in industry has been limited to binary outputs. The goal is to develop a method to estimate the object position and surface properties in real-time. This will be done by developing a network of four sensors and fusing the data using an extended Kalman filter. The former task is described in this thesis, while the latter is the topic of a companion thesis [23].

Equipping a robot with several types of sensors is also being investigated. In this way, a robot could use a camera to acquire object information when the object is far away, proximity sensors for local feedback and tactile sensors to provide sensory information once the object is grasped. Incorporating all these sensors on a robot will provide continuous sensory feedback of the environment, thus making autonomous operation a possibility.

1.2 Historical Background

Some of the first work using optical proximity sensors in robotic applications was done in 1961 by Heinrich A. Ernst at M.I.T., [7]. Ernst used a computer controlled mechanical hand, equipped with both electro-optical proximity sensors and binary tactile sensors. The motor of the parallel jaw gripper was also equipped with a low resolution potentiometer for position feedback. The hand was programmed to perform particular tasks such as pick and place operations. The proximity sensors were used in a binary fashion; they simply indicated the presence or absence of an object.

After Ernst's work, Johnston [11] and Bejczy [3] at the Jet Propulsion Laboratory in Pasadena California also used electro-optical proximity sensors for robotic applications. Johnston described three types of sensors; an amplitude modulated (AM) sensor, a triangulation based sensor or multipoint sensing and a cooperative multiaxis sensor. Two types of AM sensors were described, one that simply generates a present-not-present (binary) output and one that generates an (analog) output as a function of object distance. The binary sensor's emitted beam forms an ellipsoid-shaped sensitive volume permanently focused at a few centimetres in front of the sensor. The other, does not focus the beam, but defocusses and widens the beam. The amplitude of the received signal is then a function of the object distance, orientation and surface properties. The accuracy of the sensor was determined to be a few tenths of a millimetre.

The multipoint sensor replaces the receiver or transmitter with a semiconductor array. For a detector array, the position of the reflected beam on the array is mapped to object distance. Finally, a cooperative sensor is used only in environments where the object is known in advance. The sensor head consists of three LEDs, a light collecting telescope lens and a detector with four electrically independent quadrants. A reflector must also be placed on the object. The sensor indicates the position and orientation with respect to the reflector in terms of six independent analog signals. Calibration results of the above sensors that would accurately map sensor signal to

object distance were not presented. The effect of orientation was not discussed, either.

Bejczy [3] incorporated the proximity sensors with a vision system to provide acoustical feedback in telerobotic operations. The author used the AM sensor developed by Johnston to generate a variable pitch tone to indicate the changing output voltage and hence the distance between the proximity sensor and the object. Calibration of the sensors was not performed.

In [5], Catros et al. also incorporated IR sensors with a teleoperated manipulator to perform automatic grasping when the manipulator is within the region of the object. The authors used fibre optic proximity sensors supplied by a company called SAGEM. Orientation and surface properties effects were acknowledged but not taken into account in the sensor model. A simple $1 - d$, non-linear model where the sensor output varied as a function of object distance was used to characterize the sensors. No sensor characterization data was presented.

Balek and Kelley [2] used gripper mounted proximity sensors for robot feedback control. A hierarchical control scheme was implemented to perform four general tasks: approaching and departing objects, collision avoidance, orientation of the end-effector to the object normal and orientation in the remaining two degrees. AM sensors are used and the authors described the effects of orientation and surface properties on the sensor's output but no characterization data or model of the sensor output was presented. The surface properties of the object used were estimated à priori in order to estimate the object's distance and orientation.

In [17], Marszalec gave an overall description of optical *fibre* proximity sensor characteristics and their incorporation on a robot gripper. He showed that the magnitude of the received signal is a function of the object's distance, orientation and surface properties. The sensor parameters were found to be the diameter of the optical fibre, fibre separation and the angle of the optical fibres in the sensor head.

A fibre optic proximity sensor that measures object-sensor distance using the magnitude of the received signal was discussed by Li in [16]. The sensor head had a diameter

of only 3.5 mm and weighed only 20 g, including the weight of the cable. The sensor's range was determined to be approximately 8.5 cm. The sensor was modelled by the following nonlinear function

$$\psi = \frac{a}{d^2} + b \quad (1.1)$$

where

d is the sensor-target distance

b represents the offset effect in the sensor output

$$a = \frac{\pi\gamma_s}{3} (1 - \cos^6 \beta_s)$$

γ_s depends on the photometric effect of the sensor and object

β_s depends on the aperture of the sensor head

The sensors were tested to determine the effects of object colour, object orientation and ambient light. It was found that only the surface properties of the object affected the sensor's output significantly. In fact, the surface properties only affected the value of parameter a in the sensor model. Thus, the value of parameter a can be used to determine the surface properties of the object. The object orientation had little effect on the sensor's signal. A target orientation of 30° increased parameter a by only 11%. Therefore, the sensors were calibrated in a $(1 - d)$ fashion as a function of object distance using a milling machine that had a position accuracy of ± 0.02 mm. The data was then curve fitted using the least squares method. Determining the object's distance was achieved using à priori knowledge of the shape and surface properties of the object and by processing the sensor's nonlinear output using a Kalman filter.

Cheung and Lumelsky [6] developed a control scheme for obstacle avoidance by incorporating a sensitive skin consisting of IR proximity sensors on a robotic manipulator. The sensor system was discussed. Amplitude modulated IR sensors are used to provide an analog indication of obstacle proximity. The authors presented a detailed description of the electrical hardware required: such as the signal processing

technique employed to filter ambient light noise and demodulate the received signal. The authors did not characterize the sensors, but simply used the analog output of the sensor as an indication of the object distance. The authors acknowledged that the sensor output will be affected by the size, shape and colour of the object.

Masuda [18] presented a proximity sensor that used the phase shift of the received signal to measure distance, angle or orientation depending on the mode of operation. The sensor was made up of six LED's in a cross shaped pattern with the phototransistor in the centre. In any mode of operation, the output is a function of the amplitude of the input signals and the spacing of the LED's with respect to the phototransistor *only*. The surface reflectivity is *not* a factor, **assuming** the surface is diffuse. Goldenberg et al. [21] performed several experiments on sensors similar to Masuda's and showed that the design parameters do in fact affect the performance of the sensor. An optimal sensor was developed based on two objectives weighted 3:1 respectively: sensor sensitivity and sensor range. This is done by maximizing a weighted objective function where the criteria are normalized. Finally, experiments were carried out using the optimal sensor configuration in order to perform calibration and resolution analysis. Accuracy analysis was performed by repeating the experiments five times and comparing the actual object distances to the calculated ones.

A basic description of phase modulated (PM) and amplitude modulated (AM) optical proximity sensors is presented by Benhabib et al. in [4]. A proximity sensor can be constructed using a combination of LED's and phototransistors which is capable of operating in PM and AM mode. Only an AM mode sensor was constructed and tested. A method is then proposed that makes the sensors more robust to variations in surface-reflection characteristics. The method proposed is comprised of a combination of three different methodologies: integration of distance and orientation sensors, a novel polarization-based optical-filtering approach and active sensing.

Okada and Rembold [20] developed a proximity sensor based on the time of flight of the emitted IR beam using the triangulation method. A proximity sensor was

constructed using a spiral-shaped light emitting mechanism. The IR beam lights up a point on an object through a slit cut in a rotating disk. The distance is determined as a function of the slit's shape and the time required for the photodiode to receive a signal. The advantage of this method is that distance is not affected by the object's surface properties or by the angle of inclination since the measurement is based on the existence of a received signal and not its magnitude.

Kanade and Sommer [13] developed a sensor similar to that developed by Okada and Rembold but without any moving parts. The operating range is from 4 *cm* to 5 *cm*. The sensor is based on illumination and triangulation and uses multiple LED's and a PIN-diode area sensor chip for detecting spot positions in a plane. The directions of the beams were aligned to form a cone converging at 4.5 *cm*. A plane can be fitted through the six different 3 - *d* points obtained from the six LED's and the sensor-object distance and orientation of a small region on the object surface can be calculated.

In [9], Hirzinger described a multisensory gripper used for space robotics equipped with 15 sensory components. The author used triangulation based laser range finders with a range of 3 - 50 *cm*. The size of the sensor head was approximately half the size of a match box. The nonlinear control system adapts the transmitter's intensity as a function of the object's reflective properties. This was done within 10 μs and with a range of intensities between 1 and 4000. The laser light emitted is collimated by a lens and has a diameter of approximately 1 *mm*. The resolution of this sensor is between 0.1 % to 3 %, for near and far objects respectively.

Elgazzar et al. [15] presented the results of an extensive search for a cost-effective light-based range sensor. The sensor was used in mobile robotics to perform object detection. The main goal was to find a sensor that was off-the-shelf or that may be assembled with little modification. Two types of sensors were tested: industrial light based sensors and auto-focus modules used in cameras. The sensors were tested for sensitivity to target colour, axial response in bright sunlight, effect of object ori-

entation, effect of bright sunlight on sensor output and the sensitive volume was determined. These type of sensors were not suitable for our application since they are quite large and could not be placed inside a robotic finger and also have a range in the order of several metres with a deadband in the order of several *cm*. This deadband is much too large for our application.

1.3 Progress at McGill

Research in autonomous manipulation began at McGill University in 1992 at the Autonomous Manipulation Laboratory (AML). One of the projects is to package a Proximity Sensor Network (PSN) using small, inexpensive and rugged infrared sensors to perform local sensing for robotic manipulation. The development of a Kalman filter to fuse the sensor information is crucial to its success. A detailed description of the sensory fusion for object manipulation can be found in the master's thesis of Gregory Petryk, [23] and in [22]. Sensor fusion is used to estimate the object's albedo parameter on-line as well as the pose of the object, that is the object's position and local surface angle. The surface properties of the object used is also limited to materials that do not exhibit specular reflection, such as a mirror or a metallic object, as well as to those that do not absorb infrared radiation, such as a black coloured surface or fur. The goal is to place our sensor in the fingers of a robotic hand along with a tactile sensor and to use these in conjunction with a global sensor such as a camera or a laser rangefinder. Such a system has the potential to accomplish many dextrous robotic tasks.

1.4 Author's contributions

The author joined AML, which is headed by Professor Martin Buehler, in March 1994. At that time only some preliminary work in sensor characterization had been performed. The AML lab did not have a platform to perform experiments or sensors

with appropriate signal processing electronics. My contributions included developing two types of IR, amplitude based sensor heads and the accompanying signal processing electronics capable of gain scheduling and filtering of ambient light. This Proximity Sensor Network is the first amplitude modulated multi-sensor network that permits accurate object localization. The author also developed a planar test bed consisting of a planar-planar-revolute robot with the dual capabilities of sensor characterization and planar dynamic manipulation. When performing manipulation experiments, the electrically actuated PPR robot is equipped with a parallel jaw gripper that was developed by I. Abdul-Baki. The objects used for manipulation are placed on a revolute-revolute-revolute robot that is not actuated but equipped with high resolution encoders to provide accurate position feedback. The RRR robot was designed and constructed by Imad Kaderi, a summer student.

1.5 Organization of the thesis

The organization of the thesis is as follows. The following chapter (Chapter 2) contains a detailed description of the various measurement principles for electro-optical proximity sensors. Chapter 3 discusses the IR proximity sensors and the signal processing electronics developed. The results obtained from experimentation are presented in Chapter 4. Finally, Chapter 5 contains conclusions as well as proposed future work.

Chapter 2

Proximity Sensor Technology

There are various types of proximity sensors developed today that use different physical principles, such as magnetic, electric-field, acoustic or sonar and electro-optical. The advantages of using amplitude-based electro-optical proximity sensors is that they are small enough to fit in the fingers of a robotic gripper and the sensor output is independent of the material of the object. Also, electro-optical sensors have a range that is large enough to provide a smooth transition between global sensors, like cameras, and tactile sensors. The disadvantages of electro-optical sensors is their dependence on the object's surface properties such as surface finish and colour, their dependence on the object's orientation and their sensitivity to ambient light. Also, the output of an electro-optical sensor is a nonlinear function of distance. Currently, electro-optical sensors are being used in industry to provide information as to the presence or absence of an object. Our interest is to develop electro-optical sensors to provide continuous 3-D proximity information.

Electro-optical sensors fall under one of three categories, namely, triangulation, phase modulation (PM) or amplitude modulation (AM). These three methods are the topic of discussion in this chapter in Sec. 2.1, Sec. 2.2, Sec. 2.3, respectively.

2.1 Triangulation Principle

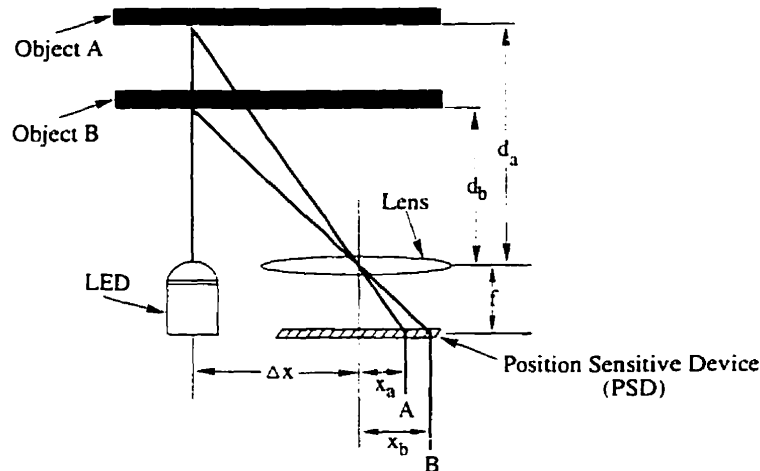


Figure 2.1: The geometry of triangulation-based sensors. The distance of the object is a function of the distance travelled by the IR beam.

Proximity sensors that are based on the triangulation principle are made up of one LED, one focusing lens and a Position Sensitive Device (PSD). The distance of the object is determined by the position of the light beam on the PSD (see Fig. 2.1). Knowledge of the distance between the LED and the PSD (Δx), the focal length of the lens (f) and the trajectory of the light beam can be used to perform triangulation to determine the distance of the object from the sensor. The distance of object A in Fig. 2.1 is expressed as

$$d_a = \frac{\Delta x}{x_a} f$$

where f is the focal length of the lens, Δx is the horizontal distance between the LED and PSD centre and x_a is the position of the reflected light beam measured from the PSD centre. The factors that must be considered when designing a triangulation based sensor are the size of the PSD, the distance between the LED and the PSD as well as the intensity of the LED. There is a trade-off when designing a triangulation

based sensor. The distance between the LED and PSD device as well as the size of the PSD determine the effectiveness of the sensor. A large separation increases the sensor's range but also increases the deadband at close range. A large PSD or a lens with a small focal length is necessary for operation of the sensor at close distances.

The ideal model for such a sensor makes certain assumptions. The light beam is a line and therefore the projected spot a point. The optics do not distort or defocus the light beam. The PSD determines the position of the spot in a linear fashion. In reality, the light beam is not a line but a cone and the projected spot not a point but a circle with a certain area. The intensity of this circle is greatest in the centre and therefore the PSD must be accurate in determining the centre of this circle as the point of interest. PSDs also do not contain a continuous sensitive surface. Therefore, the number of sensing elements of the PSD determine the resolution of the sensor.

2.2 Phase Modulation

Proximity sensors developed on the principle of phase modulation are presented in [4, 21, 18]. This type of sensor consists of two LEDs and one photodiode and is shown in Fig. 2.2. The mechanical design parameters are the distances a and b and angle θ . The electrical design parameters are the intensities A and B of LED-a and LED-b, respectively. Both LEDs are modulated at a particular frequency that is selected above the electrical line frequency of 60Hz but at 90 degrees with respect to each other. The phase difference between the signal received by the photodiode and the modulated signal at LED-a is a function of the sensor geometry, the intensity of light generated by the LEDs and the distance between the object and the sensor. This relationship is derived in [18] and presented in (2.1). This relationship shows that the distance between the object and robot is directly proportional to the phase shift between the generated signal at LED-a and the received signal and is not affected by the albedo parameter which is a function of the object's surface properties.

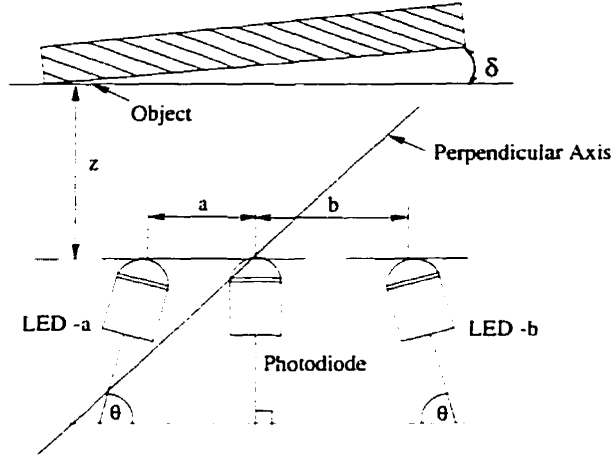


Figure 2.2: The geometry of a phase-based sensor. The distance of the object is a function of the phase difference between LED-a and the signal received by the photodiode.

$$\phi = \tan^{-1} \left[\frac{B}{A} \left(\frac{a^2 + z^2}{b^2 + z^2} \right)^{3/2} \right] \quad (2.1)$$

where A , B are the intensities of LED-a and LED-b, respectively, ϕ is the phase difference between LED-a and the received signal at the photodiode and z is the distance between the sensor and the object.

The effect of the object orientation on the signal is not discussed for this sensor. Instead, to eliminate the effect of orientation on the received signal, the authors in [21, 18] add four more LEDs on the same plane as LED-a and LED-b, two along the same axis and two along a perpendicular axis (Fig. 2.2). Using these four extra LED's, it is possible to measure the orientation of the object with respect to the sensor. The relationship between these two additional pairs of LED's and the angle between the axis along which these new sensors are placed and the object is

$$\phi' = \tan^{-1} \left[\frac{B'}{A'} \left(\frac{z - b \tan \delta}{z + b \tan \delta} \right) \right] \quad (2.2)$$

where A' , B' are the intensities of LED-a' and LED-b', respectively, ϕ' is the phase difference between LED-a' and the received signal at the photodiode, z is the distance

between the sensor and the object and δ is the angle between the object and the axis along which the two LED's were placed

In [21], the authors attempted to determine the design parameter required to maximize the performance of the sensor. One can easily observe that the values of the distances a and b must not be equal in order not to simplify (2.1). The design parameters were determined experimentally by maximizing the value of a weighted combination of two objectives: large range and sensitivity of the sensor. It was determined experimentally that the optimum values were, $A = 40 \text{ mA}$, $B = 83.5 \text{ mA}$, $a = 4 \text{ mm}$, $b = 9 \text{ mm}$ and $\theta = 70^\circ$. The authors calibrated the sensors with respect to distance but they did not take any measurements at constant distances while varying the orientation of the object to verify that the sensor distance estimation is unaffected by the object's orientation. Finally, the following assumptions were made about the sensor and object: The LED's have a wide emission angle, the photodiode has a narrow receiving angle and the object is perfectly diffuse and does exhibit specular reflections.

2.3 Amplitude Modulation

Sensors based on the principle of Amplitude Modulation (AM) rely on the surface of the object to exhibit diffuse reflection. A diffuse surface is usually rough in texture and an ideal diffuse surface reflects an incoming beam equally in all directions. Although light is reflected in all directions, the intensity of the light is not uniform in all directions. The intensity of light is greatest at 90° to the object surface or along the normal at the point where the light spot is projected. The intensity of light then diminishes as the angle increases according to the findings of Heinrich Johann Lambert [12], who determined this function to be

$$I = I_0 \cos \theta_0 \quad (2.3)$$

Therefore, the orientation of the object with respect to the sensor has a significant affect and diminishes the signal according to the above specified function. The effective sensing area of an AM sensor is determined by the effective areas of its components, the LED and phototransistor, and their placement with respect to each other. A typical configuration of an AM sensor along with the relevant design parameters is shown in Fig. 2.3. The LED emits an IR beam at a particular angle and the phototransistor detects IR light within a predefined area. The overlap of these two regions determines the effective range of the sensor.

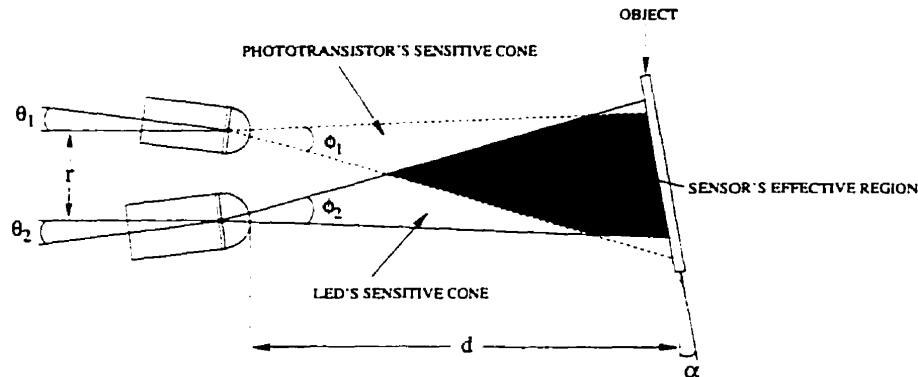


Figure 2.3: The geometry of an amplitude-based sensor. The LED's emission cone and the phototransistor's receiving cone define the sensors usable region.

In Fig. 2.3, it is also evident that the sensing area of the sensor can be modified by changing the mechanical parameters, θ_1 , θ_2 , and r . In order to maximize the range for such a sensor, θ_1 and $\theta_2 = 0$ or placed parallel to each other and r is minimized.

The amplitude of an AM sensor is a function of the distance of the object, the angle of the object's surface normal with respect to the sensor beam and the surface properties of the object. The following function is used to model an AM sensor

$$v = f(d, \alpha, \lambda) \quad (2.4)$$

where v is the output voltage of the sensor, d is the distance between the sensor and the object, α is angle between the sensor beam and object surface and λ is the albedo

parameter which depends on the surface properties of the object.

A typical output curve of an AM sensor with varying distance but constant orientation is shown in Fig. 2.4. Since the output curve of such a sensor is not monotonic, only the portion of the curve with $x \geq x_{min}$ is used. This results in deadband region. Fortunately, this problem is easily solved by simply recessing the sensor head by x_{min} , which is usually in the order of several millimetres. The useful region is also limited to $x \leq x_{max}$, which is a function of the curve's gradient and noise level.

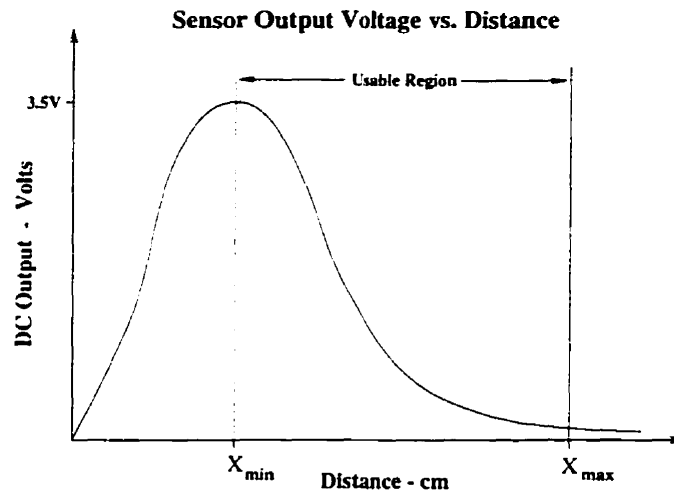


Figure 2.4: The bell shaped output curve of an AM sensor.

If this curve was to be obtained at a different orientation, the shape would remain the same but it would simply be scaled down as angle α increases. Finally, the same holds true for the albedo parameter. The effect of the albedo parameter on the output curve is that it simply scales this curve up for very diffuse, IR reflective surfaces such as white paper and it scales the curve down for less optimum surfaces, such as coloured objects. Therefore, the albedo parameter can be thought of as a constant scaling factor or gain, capturing the IR reflectivity of a surface.

Chapter 3

Proximity Sensor Network

This chapter contains a detailed description of the sensor head design, as well as the PSN hardware. Sec. 3.1 describes the requirements the sensors developed needed to satisfy, as well as the reasoning behind the selection of using AM sensors. The design of the EBS and PBS sensor heads is discussed in Sec. 3.2. The electronic circuit used to drive the LEDs and the signal processing electronics used to condition the raw sensor signal is the topic of discussion in Sec. 3.3 and Sec. 3.4, respectively. The final topic of the chapter is presented in Sec. 3.5 and describes the use of a microcontroller in the PSN to perform multiplexing, gain scheduling and communication to a host computer.

3.1 Sensor Requirements

Our goal was to build proximity sensors that were inexpensive, small, rugged and provided data at a high bandwidth. By placing several of these sensors in the fingers of a robotic hand or gripper, manipulation and dynamic grasping experiments can be performed. A Proximity Sensor Network (PSN) which consists of four sensors was built. The sensors work on the principle of Amplitude Modulation (AM). The effect of the object's surface properties is eliminated by using knowledge of the object geometry

and then using an Extended Kalman Filter to estimate the albedo parameter on-line.

The sensors that were to be developed needed to satisfy the following requirements

- small size, less than 8 mm in diameter
- range of approximately 10 cm
- PSN bandwidth of at least 500 Hz
- inexpensive, total cost under $\$1000$
- rugged
- insensitive to ambient light conditions

The reason an AM sensor was selected to be developed is simply because it was reasonable to assume that all the above requirements could be achieved. It would be possible to build an AM sensor head with a diameter as small as 5.55 mm . Such a size would be virtually impossible using phase modulation or triangulation. The smallest size PSD presently available is built by Hamamatsu and has a length of 6 mm . As a result, the smallest possible sensor that could be built would be 11 mm , assuming a 1 mm spacing between the LED and PSD, the LED is 2 mm in diameter and the protective tube has thickness of 1 mm . A second problem that would be encountered is in the lens required for such a sensor. The deadband of the sensor is equal to the focal length of the lens. Therefore, since only a small deadband is desired, a very small lens would be needed. Using a very small lens would make it difficult to physically place in position. Also, a small lens may not focus the incoming beam sufficiently. As for Phase Modulation (PM), as described in Chapter 2.2, it was found in [21] that the sensor's performance is optimized if $a = 4\text{ mm}$ and $b = 9\text{ mm}$, see Fig. 2.2. Thus, it would be impossible to obtain the required size of 8 mm since the overall size of the sensor would be at least 20 mm . Finally, two assumptions were made as to the operating conditions. First, the sensors will be operated at approximately room

temperature. Second, the receiver will not be used in a manner in which it would saturate, such as pointing it directly into the sun or other light sources.

3.2 Sensor Head Design

Once the mode of operation of the sensor head is selected, the individual component types must then be determined. There is no wide selection of emitters available, therefore, a light emitting diode (LED) was a logical choice. Due to its small size, the OP224 LED from OPTEK was used for all the sensors developed. Its characteristics are, an outside diameter of 1.57 mm , a rise time of 500 ns and a fall time of 250 ns . Furthermore, the data sheets for the OP224 LED can be found in Sec. A.5. The selection of the type of receiver is not so simple. There are three types of receivers from which to choose: photodarlington, phototransistor and PIN diodes.

	<i>Darlington</i>	<i>Transistor</i>	<i>Transistor</i>	<i>PIN Diode</i>
<i>Part Number</i>	OP305SL	OP644SL	OP804SL	OP900SL
<i>Diameter</i>	1.57 mm	1.57 mm	4.75 mm	1.57 mm
<i>Rise Time</i>	1.3 ms	2.5 μs	2.0 μs	100 ns
<i>Fall Time</i>	0.6 ms	2.5 μs	2.0 μs	100 ns
<i>Load Resistance (R_L)</i>	1k	1k	.1k	1k
<i>On-State Collector Cur.</i>	14 mA	7 mA	7 mA	N/A

Table 3.1: Data from OPTEK Technology Data book [10]

The characteristics of each of these receivers are displayed in Table 3.1 and their data sheets can be found in Sec. A.1, Sec. A.2, Sec. A.3 and Sec. A.4, respectively. It is evident looking at the Current vs. Irradiance curves found in Chapter A that a photodarlington is four orders of magnitude more sensitive than the phototransistor and the PIN diode. For example, at 4 mW/cm^2 of irradiance, the outputs of a *OP305SL* photodarlington, a *OP644SL* phototransistor and a *OP900SL* PIN diode

are 50 mA , 1.1 mA , $2.5\text{ }\mu\text{A}$, respectively.

The speed of these devices differs as well. The total rise time and fall time of the *OP305SL* photodarlington, *OP644SL* phototransistor and *OP900SL* PIN diode can be compared by looking at the Rise Time and Fall Time vs. Load Resistance curves found in Chapter A. It was found that at $1\text{ k}\Omega$ of load resistance, the total rise and fall time for the *OP305SL*, *OP644SL* and *OP900SL* were 1.9 ms , $5\text{ }\mu\text{s}$ and 200 ns , respectively.

Therefore, the following can be concluded. The photodarlington is the most sensitive device but also the slowest. The PIN diode is the fastest device but also the least sensitive. The phototransistor performs in between the photodarlington and PIN diode, it is more sensitive than the PIN diode but less sensitive than the photodarlington. It exhibits similar features with respect to speed.

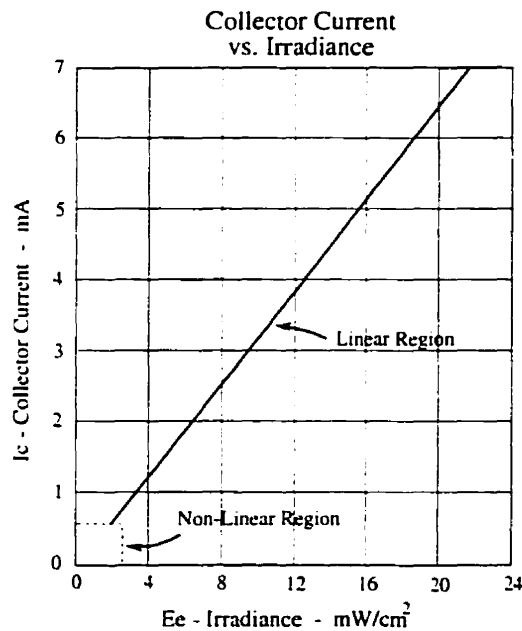


Figure 3.1: Response of the OPTEK OP644SL phototransistor taken from the OPTEK Technologies Data Book [10]

The disadvantage of using a phototransistor or photodarlington is that the first part of their response curve is non-linear as shown in Fig. 3.1. The data sheets given

by the manufacturer and presented in Chapter A do not clearly indicate this. The initial non-linear response of the receiver is undesirable since operation in that region would distort the sensor's AC signal. A PIN diode however, exhibits a linear response throughout its entire range.

It was determined through preliminary testing that a phototransistor would yield a larger range than a PIN diode. A photodarlington was not used since it would be bandwidth limited if modulated at 25 kHz . Therefore, the initial non-linearity of the phototransistor must be avoided. Two methods were used to eliminate this problem: 'photon' biasing or 'electrical' biasing. 'Electrical' biasing is possible only if the package of the phototransistor permits access to the base connection. The *OP644SL* has a diameter of 1.57 mm and is the smallest package available from OPTTEK. This particular package does not allow for access to the base pin. Similar small package sizes from other manufacturers also do not allow for access to the base pin of the phototransistor. The *OP804SL* is a larger package with an outside diameter of 4.75 mm . In this case, the package allowed for easy access to the base pin of the phototransistor.

3.2.1 Photon Biased Sensor Head

The first sensor head that was built relied on 'photon' biasing to eliminate the non-linear effect of the phototransistor. This was implemented by exposing the phototransistor to a constant amount of IR light. The Photon Biased Sensor (PBS) was built by strategically placing a second LED (the "DC LED") to supply enough constant IR light to surpass the non-linear region but not an excess amount so as not to saturate the phototransistor or limit the available range. There are two figures that show the make-up of such a sensor, Fig. 3.2 and Fig. 3.3. As can be seen in Fig. 3.3, the biasing LED was actually filed in order to fit the required dimensions. It would have been possible to move the AC LED and phototransistor radially outwards in order to create more space for the DC LED. Such a design was tested and it was determined

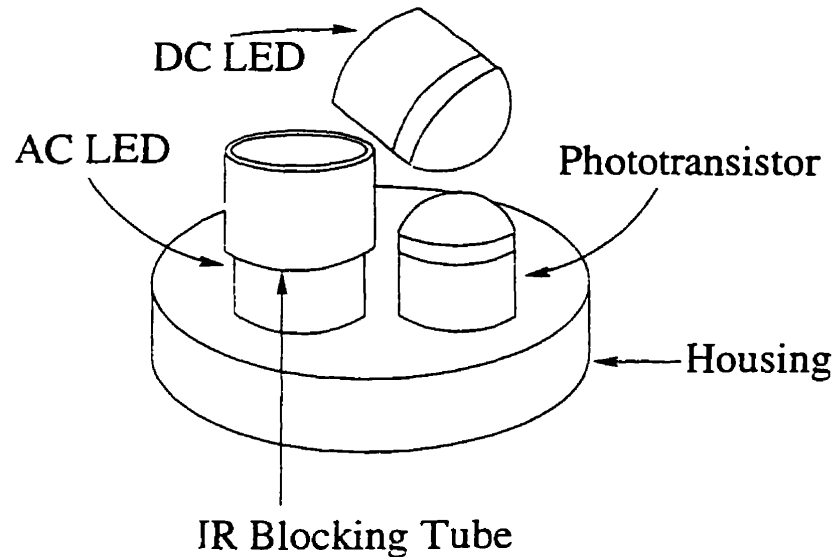


Figure 3.2: A PBS Sensor head and its three components, a modulated AC LED, a DC biasing LED and a phototransistor

that placing the AC components near the wall of the outside tube generated a great deal of cross talk. This cross talk, which originated from AC IR rays bouncing off the inner wall of the tube, was sensed by the phototransistor. Cross talk is undesirable and must be minimized since it limits the sensor range by reducing the voltage range of the sensor.

The PBS sensor was designed so that there was at least 0.6 mA of collector current when the DC biasing LED was placed approximately at an angle of 55° to the sensor housing surface. The DC LED was placed away from the area above the phototransistor in order not to physically block the incoming signal from reaching the phototransistor. The DC biasing LED was fixed to the housing and held in position using standard one step epoxy.

One problem encountered while constructing the PBS sensor head was that the LEDs emitted outwards from the top and also all around its circumference. This radial IR beam generated cross talk between the AC LED and the phototransistor. Double sided copper board used in the electronics industry was used as the housing

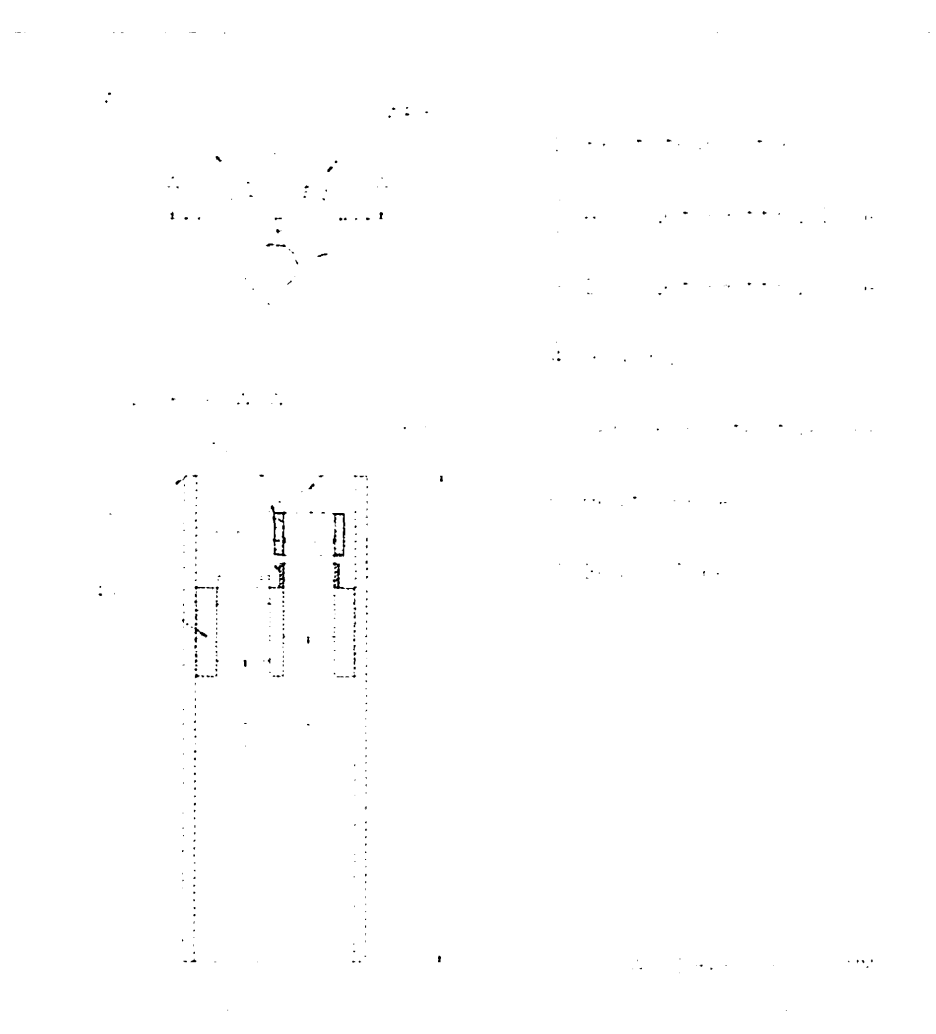


Figure 3.3: A top view and side view of a PBS head.

material. Although copper is a good IR blocker, the material separating the copper layers is not. Therefore, the housing did not eliminate the cross talk generated by the radial signal. Other sensor housing materials, such as black delrin which is a hard plastic, were investigated in an attempt to eliminate this effect. The problem with such a housing was that making the electrical connections to the components proved to be too difficult. Wires were connected directly on the components only after the components were glued in place. The heat generated during soldering melted the small plastic housing. There was no way to solder first and then to place the components since soldering the wires in place affected the geometry of the components. Therefore, having a double sided board and soldering the components to the copper surface, then connecting the wires was the 'easiest' and most reliable method to place the sensor in a housing structure with connecting wires exiting the bottom of the housing.

Although using the copper board solves the problem of the placement of components, it still does not solve the cross talk problem. This was done by placing the AC LED slightly higher than the phototransistor and wrapping it with black shrink wrap on the area below the connecting pins and soldering on a small copper tube around the area above this pin. The shrink wrap and the copper tube blocked all radial IR beams.

Finally, this housing, with the components fixed in position, was placed inside an aluminium tube with an outside diameter of 5.55 mm . The tube was added in order to make the sensor more rugged and also to allow for easy insertion of the sensor head in an appropriately sized hole. This configuration proved to be quite rugged, withstanding several mishaps. A photo of several PBS sensor heads with and without the outside tube is shown in Fig. 3.4.

Although the PBS worked quite well, building the sensor proved to be quite difficult and cumbersome. The main difficulty was related to the placement of the "DC LED". Therefore, a new method to bias the phototransistor had to be found.

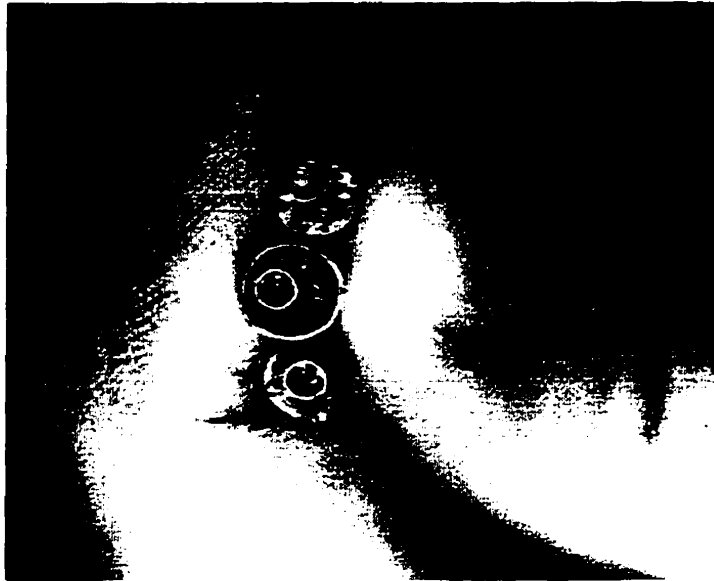


Figure 3.4: A photo of three PBS sensor heads. The two outer ones have no outer aluminium tube.

3.2.2 Electron Biased Sensor Head

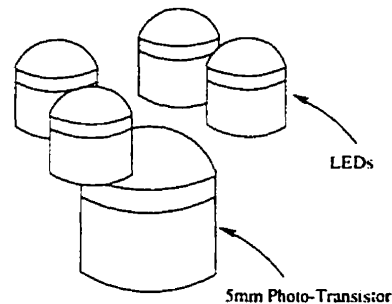


Figure 3.5: An EBS Sensor which has four LEDs (AC) placed above a larger photo-transistor.

The second type of sensor built was an “Electron” Biased Sensor (EBS) which uses electric current to achieve the required biasing. Since the *OP644SL* phototransistor package does not give access to the base pin of the transistor, using another package type was investigated. It was found that the smallest package offering access to the base pin of the transistor was the *OP804SL* whose outside diameter of 4.75 mm was

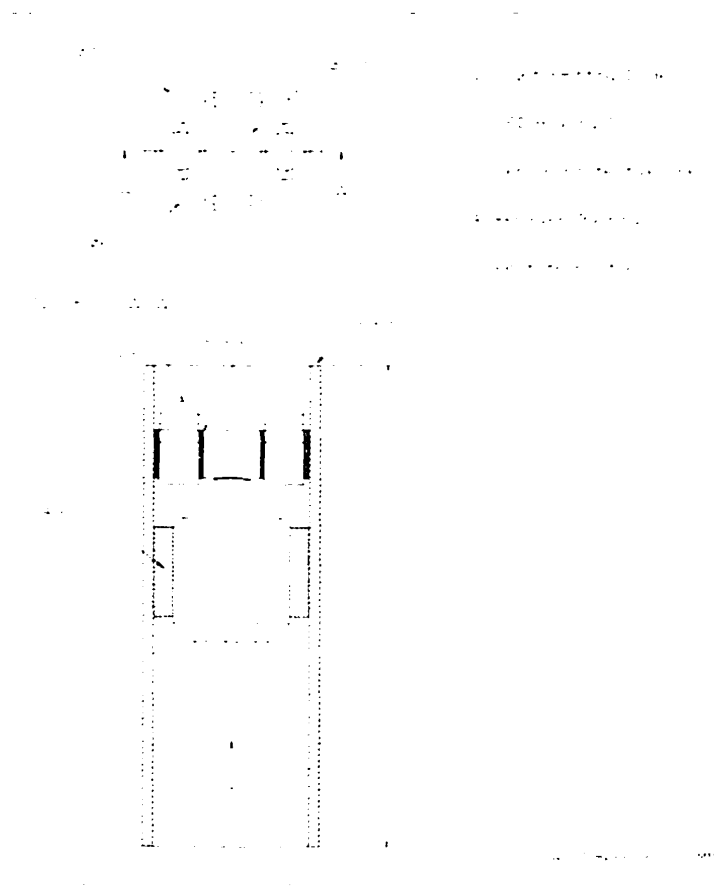


Figure 3.6: A top view and side view of an EBS head.

much larger compared to the original size of 1.57 mm . Since the overall size of the sensor was required to be less than 8 mm , a new design for such a sensor would be needed. That is, placing the phototransistor and LED side-by-side was not feasible due to the size limitation.

An EBS sensor was designed using 4 LEDs and one *OP804SL* phototransistor as shown in Fig. 3.5. The LEDs had an outside diameter of 1.57 mm . The LEDs were symmetrically placed in a plastic housing disc. The phototransistor was inserted from below the disc, see Fig. 3.6. As a result of using such a geometry, the overall sensor size was kept within specifications. The AC coupling was eliminated by simply painting the outer and inner surfaces of the LED housing disc. The same material was used for the disc as was used for the PBS housing. Thus, the top and bottom copper surfaces were free from IR penetration but the surface in contact with the outer tube and the inner surface of the disc did not block IR radiation. Therefore, these two surfaces were painted with a thin layer of black paint in order to block any radial IR radiation.

Finally, this whole package was then placed in a brass tube with an outer diameter of 7.15 mm . Brass was used here instead of aluminium only because the brass was more readily available at this size. Although, the LED housing disc partially covered the receiver, there was a sufficient opening in the disc centre that a significant signal was measured with an object placed at 10 cm from the sensor head. Building the EBS sensor was much easier compared to the PBS sensor and also less time-consuming. The calibration curves showing the respective ranges for both the PBS and EBS sensors are presented in the following chapter.

3.3 Driving Electronics

In order to filter out ambient light, the LEDs must be modulated at a frequency above 60 Hz . We selected to modulate the LEDs at 25 kHz . The reason 25 kHz was selected will be discussed in Chapter 4. If the sensors are physically placed in such a way that there is an overlap of their respective sensing regions, then there exists the

possibility of cross talk between sensors. One solution is to modulate the sensors at different frequencies. Fortunately, cross-talk between sensors does not exist for the PSN since only one sensor is active at any given moment. Multiplexing the sensors is an easy way to eliminate cross-talk. Unfortunately, multiplexing is not possible for a larger network consisting of many sensors since the system bandwidth would decrease drastically.

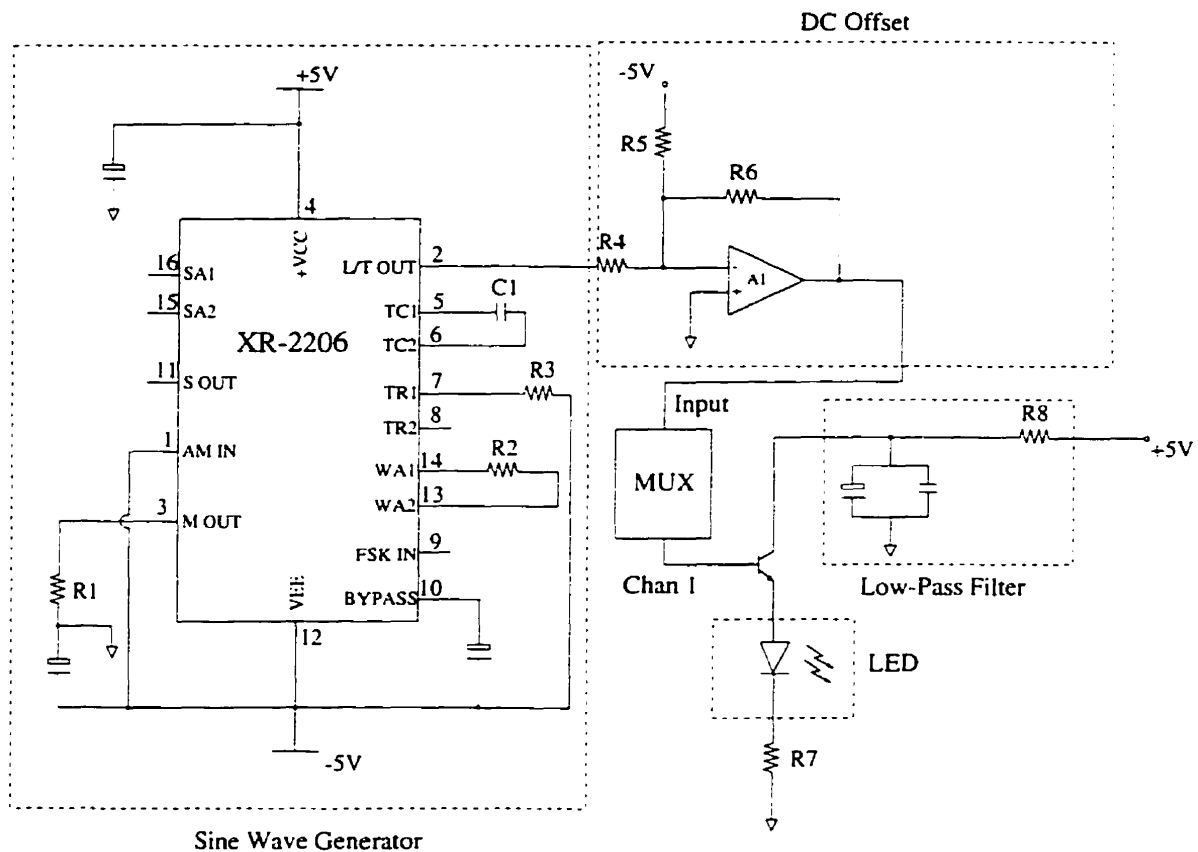


Figure 3.7: Version 1 of the LED driving electronics implemented on the PSN board dedicated to the PBS heads.

A sine wave tuned to the desired modulating frequency is generated using the XR2206 chip, a function generator chip made by the XAR Corporation. This waveform is then offset in order to compensate for the voltage drop across the transistor that was used to regulate the current through the LED. The supply voltage to the transistor's collector is low-pass filtered in order to remove any noise that would affect

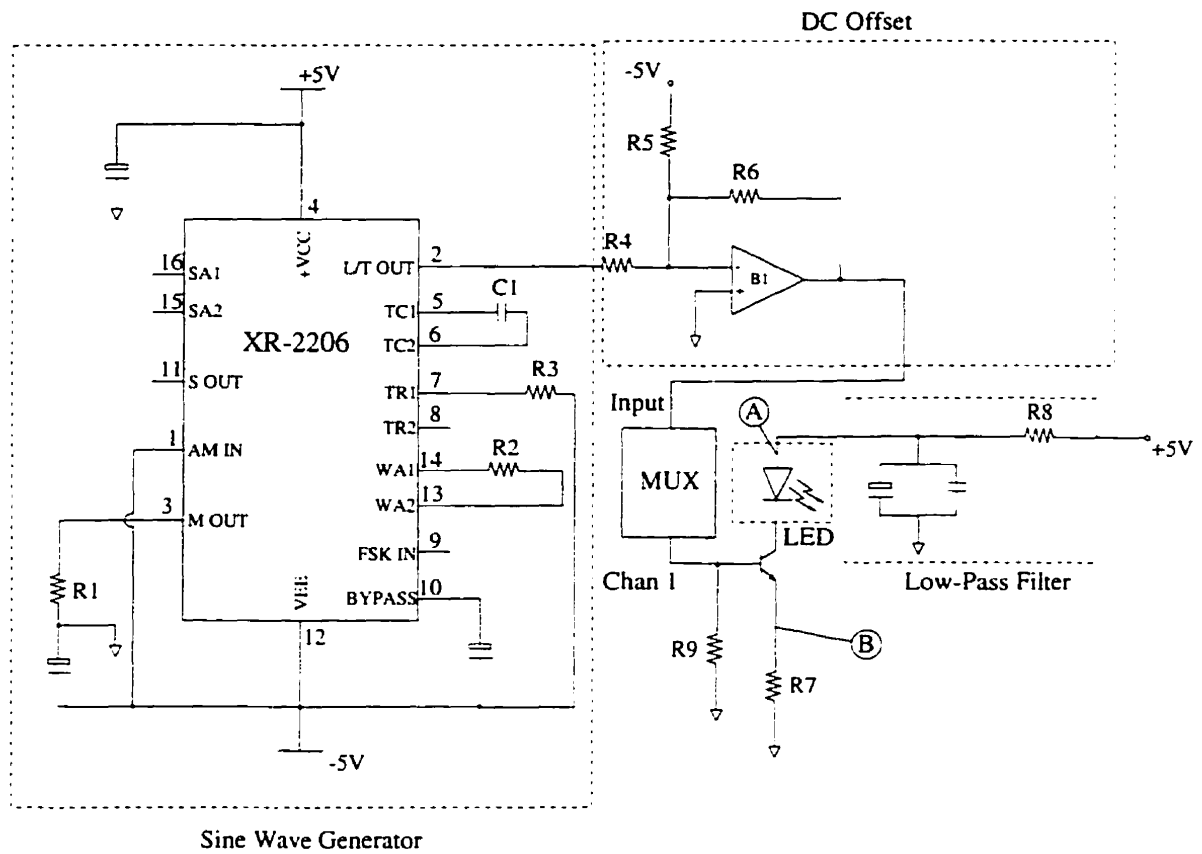


Figure 3.8: Version 2 of the LED driving electronics implemented on the PSN board dedicated to the EBS heads.

the amount of current through the LED. A multiplexer is used to select between the appropriate sensor and it is controlled by the HC11 microcontroller. The driving circuit presented in Fig. 3.7 was the original circuit developed and is used only with the PBS sensor heads. The circuitry implemented with the EBS sensor is slightly different and is presented in Fig. 3.8. The difference between these circuits is that the LED is placed in the collector of the transistor rather than with the load resistor. This change improves transient response and maintains a more constant current through the LEDs, since the collector current (and thus the IR emitted intensity) is only a function of the base voltage and the emitter resistor R_7 , and not the varying LED voltage. Fig. 3.9 shows the driving signal at the LED's anode, point A in Fig. 3.8. There is a transient associated with turning on the LEDs, but the total "On" time is sufficient for the signal to reach steady state. The signal at the emitter of the phototransistor, point B in Fig. 3.8, is shown in Fig. 3.10. In order for the collector to supply the required current, the following rule of thumb is used

$$V_e + 1.0 < V_c.$$

Looking at the signal at the emitter, the maximum voltage is 0.8 V while the minimum voltage drop at the collector is 3.6 V. Therefore, in our case there is no problem as far as supply current is concerned.

3.4 Signal Processing Electronics

The phototransistor detects the intensity of the IR signal returned by a diffuse object which reflects the LEDs' outgoing beam. The phototransistor converts this light energy into a current that flows through from the collector to the emitter. This current should be converted to a DC signal that varies between 0–5 V. The electronic circuit that accomplishes this is made up of five discrete stages and is shown in Fig. 3.11. The first stage converts the current generated by the incoming IR beam into a voltage using resistor R_1 . A sample signal at the emitter of the phototransistor, or point 1 in

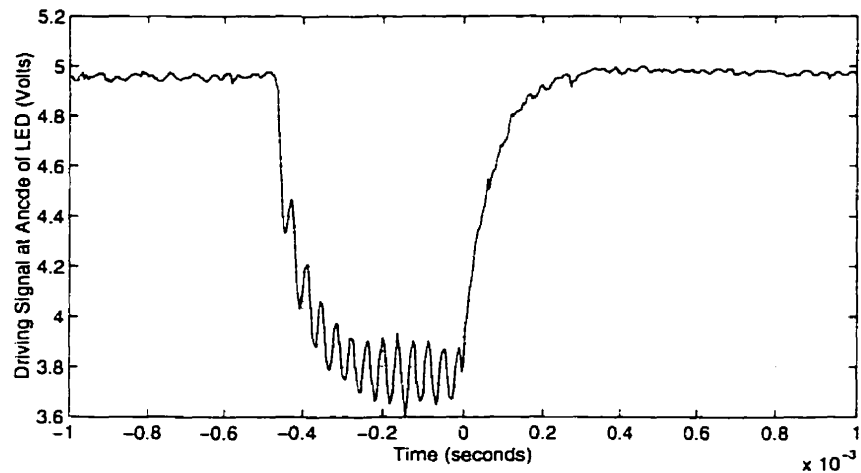


Figure 3.9: The driving signal at the LED's anode for an EBS head using its signal processing electronics. This corresponds to point A in Fig. 3.8.

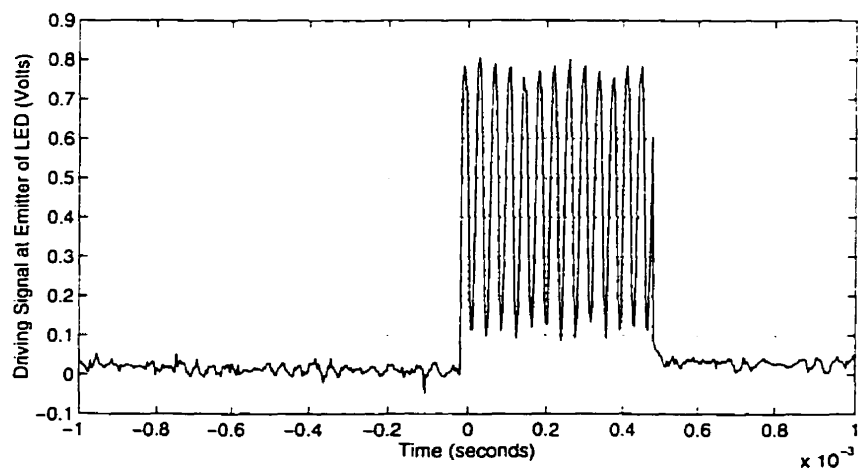


Figure 3.10: The driving signal at the LED's emitter for an EBS head using its signal processing electronics. This corresponds to point B in Fig. 3.8.

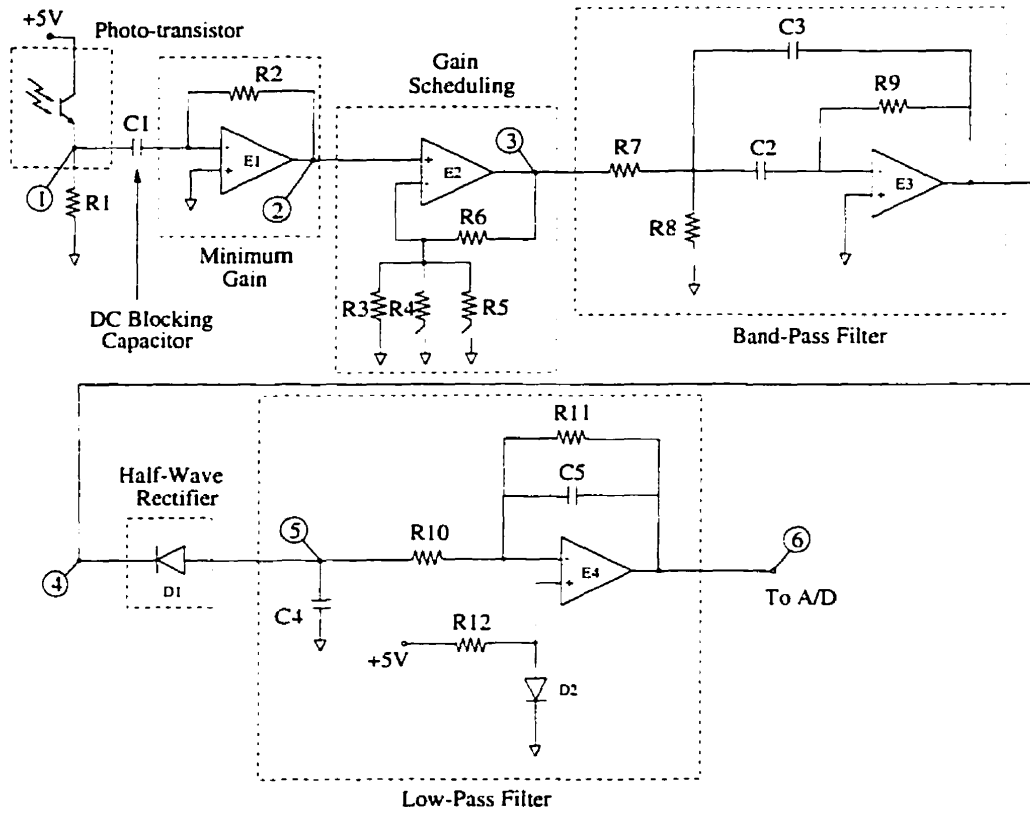


Figure 3.11: Signal processing electronics for phototransistor receiver.

Fig. 3.11, with an object at approximately 4 cm from the sensor is shown in Fig. 3.12. The signal is very weak and the SNR is approximately 1.5. Conditioning this raw signal is crucial to the success of accurately estimating the distance and orientation of the object.

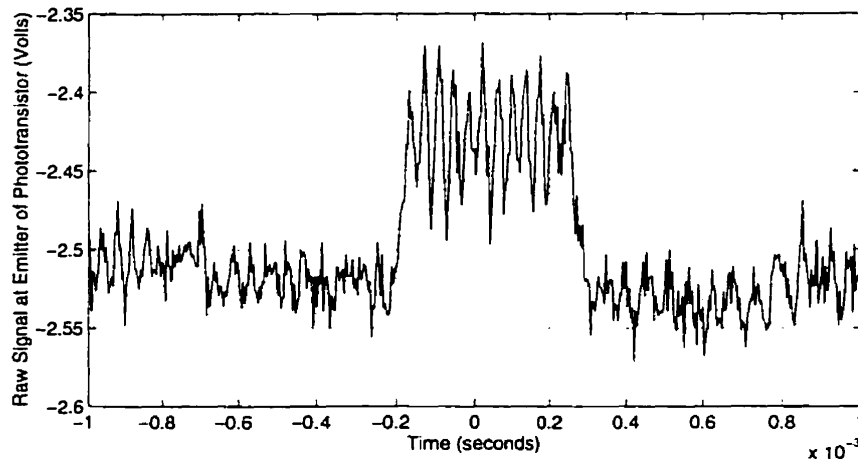


Figure 3.12: The raw signal present at the emitter of the phototransistor. This corresponds to point 1 in Fig. 3.11.

C_1 in Fig. 3.11 is used to block any DC offset the signal might have incurred. Note that this capacitor is not sufficient to remove the 60 Hz signal introduced from interior lighting. The last part of the first stage consists of a constant gain amplifier, $E1$, whose gain is determined by R_2 . A sample signal after $E1$, or point 2 in Fig. 3.11, is shown in Fig. 3.13. The environmental conditions, that is position and orientation of the object, were kept constant for all sampled signals throughout this chapter. The object was placed at 90° to the sensor, at approximately 4 cm from the sensor. In Fig. 3.13, it is evident that the signal has no DC component and has been amplified slightly. The SNR remains roughly the same as in the previous stage, approximately 1.5.

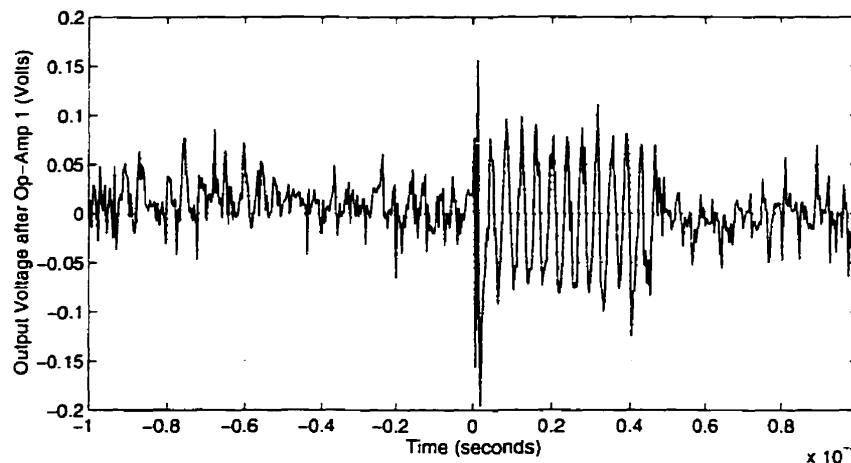


Figure 3.13: The signal after $E1$ or point 2 in Fig. 3.11.

3.4.1 Stage 2: Gain Scheduling

The second stage of the signal processing electronics consists of a variable gain stage, in order to increase the effective resolution of the A/D conversion. This will be discussed further in Sec. 3.5. A variable gain is needed since applying a constant large gain in order to maximize the sensor's range would saturate the sensor at close distances. Using a lower gain would not maximize the sensor's range. The variable gain stage is adjusted according to the current object position.

The output curve of an AM sensor is shown in Fig. 3.14. This bell-shaped curve was divided into three regions, the low-gain region, the medium-gain region, and the high-gain region. At first, it is assumed the object is out of range and the gain is set to high. Then the gain remains high until the output signal increases to a value greater than 3.48 V . At this point, the gain is decreased to the medium gain. The gain is set to the low gain if the sensor signal increases past 3.48 V again or is set back to high if the signal decreases below 0.3 V . The state machine showing this logic is shown in Fig. 3.15.

Selecting the switching points for this variable gain stage is very difficult. The procedure used to do this is the following. First, the sensor was run with the PSN set to the low gain. All components are then adjusted to set the PSN output to the

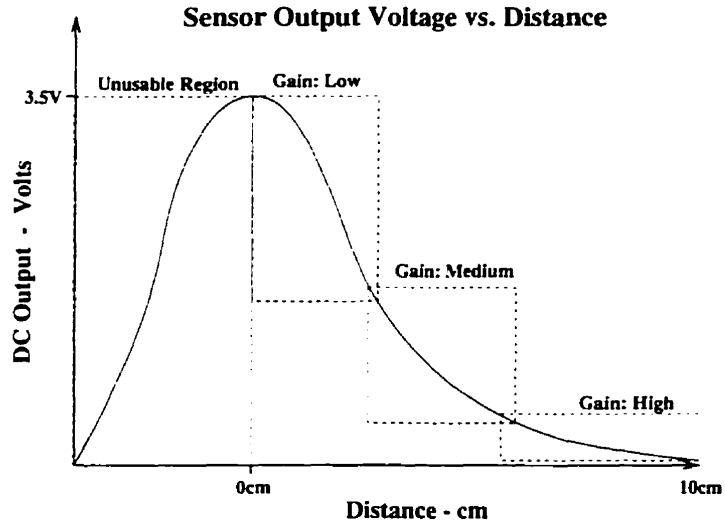


Figure 3.14: Sectioning the response curve of the sensor and assigning specific gains to each portion.

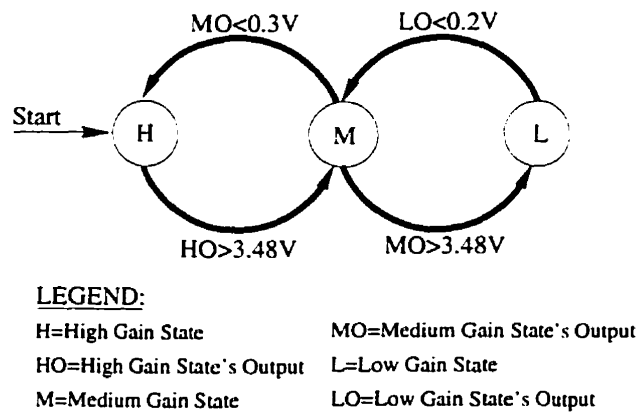


Figure 3.15: The state machine which determines the gain for each sensor.

maximum possible once a paper is placed in a position which maximizes the raw sensor signal. That is, at this object position, the PSN outputs $3.5 V$, the raw sensor signal is the maximum possible and the gain is kept at low. This defines all components in Fig. 3.11 except R_4 and R_5 . Once this is done, the medium gain is selected such that at the switching point the sensor output for the medium gain is approximately twice the noise level below the maximum PSN output of $3.5 V$. That is, a sensor output of $0.2 V$ for the low gain corresponds to $3.3 V$ at the medium gain for a noise level of $0.1 V$. Therefore, the overlapping region is set to twice the noise level, which in this case is $0.2 V$. This is done because if the hysteresis region is too small, a ringing effect will occur with the gain switching back and forth at the switching point simply due to noise effects and not to object motion. Selecting a large hysteresis region limits the maximum high gain possible and thus the range of the sensor. Finally, this procedure is repeated to set the high gain.

The variable gain stage is implemented using an op-amp and a multiplexer, shown in Fig. 3.11. The gain for this stage is

$$\text{Variable Gain} = 1 + \frac{R_6}{(R_3 || R_4 || R_5)} \quad (3.1)$$

The above equation is interpreted as follows. If the low gain is selected the denominator of the second term is simply R_3 . This term is then $R_3 || R_4$ for the medium gain and $R_3 || R_5$ for the high gain. The appropriate gain is selected by the HC11 microcontroller by monitoring the sensor's output. How this is done will be discussed in more detail in section 3.5. A sample signal taken after $E2$, or point 3 in Fig. 3.11, is shown in Fig. 3.16. The signal has been considerably amplified and the SNR remains approximately 1.5.

3.4.2 Stages Three to Five

The last three stages consist of a band-pass filter, half-wave rectifier and a low-pass filter, as shown in Fig. 3.11. The band-pass filter is a single op-amp, multiple-feedback

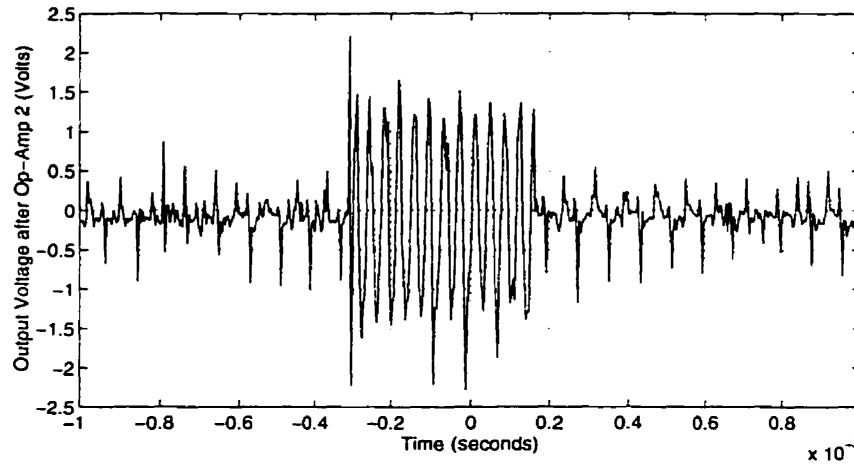


Figure 3.16: The signal after $E2$ or point 3 in Fig. 3.11.

design, tuned to the frequency of approximately $f_o = 25\text{ kHz}$ in order to allow only the modulated signal to pass through, [8]. The following design steps were used to select the components of the filter. The first step is to let $C_2 = C_3$ and then select a standard value near

$$\left(\frac{10}{f_o}\right) \mu F$$

where, $f_o = \frac{\omega_o}{2\pi}$ is the filter frequency. Then,

$$R_7 = \frac{Q}{H_o \omega_o C_3}$$

$$R_8 = \frac{Q}{(2Q^2 - H_o) \omega_o C_3}$$

$$R_9 = \frac{2Q}{\omega_o C_3}$$

Rearranging the above equations, it is possible to relate the filter bandwidth (Q), filter frequency (ω_0) and filter gain (H_0) to the components as follows

$$Q = \sqrt{\frac{R_9}{4} \left(\frac{1}{R_7} + \frac{1}{R_8} \right)} \quad (3.2)$$

$$\omega_o = \frac{\sqrt{\frac{1}{R_7} + \frac{1}{R_8}}}{C_3 \sqrt{R_9}} \quad (3.3)$$

$$H_o = \frac{R_9}{2R_7} \quad (3.4)$$

For our filter, it was desired to have a gain as close to one as possible. The value of Q determines the width of the band-pass region. A higher Q value generates a narrower filter band which is preferable since no other frequencies are of interest. Unfortunately, selecting a higher Q value also increases the time required for the filter to converge. If the filter does not converge within the “on-time” of the sensor, the filter would distort the signal.

R_7	R_8	R_9	C_2	C_3	H_o	Q	f_o
7.5 k Ω	240 Ω	16 k Ω	3.6 nF	3.6 nF	1.067	4.15	22.9 kHz

Table 3.2: *Band-pass filter specifications*

The band-pass filter was designed with $Q = 5$ and $H_o = 1$. The final specifications of the filter are summarized in table 3.2. The differences arise from the fact that discrete analog components were used to implement the filter. A sample signal taken after $E3$, or point 4 in Fig. 3.11, is shown in Fig. 3.17. The noise level has been significantly reduced with the signal having a SNR of approximately 12. It is also evident from this figure that the filter requires roughly four cycles before convergence.

Before the sensor’s signal can be fed to the HC11’s A/D converter, the signal must be converted from AC to DC . This is the task of the last two stages. The first stage is a half-wave rectifier and is implemented using a simple diode (Fig. 3.11). There are two reasons why a full-wave rectifier was not implemented. The first is due to physical constraints. The PSN board is required to be as small as possible since it will reside on the robot’s wrist, near the fingers. In order to implement a full-wave rectifier, extra circuitry would have been required, thus, increasing the size of the board. Another reason why a full-wave rectifier is not necessary is that the last stage

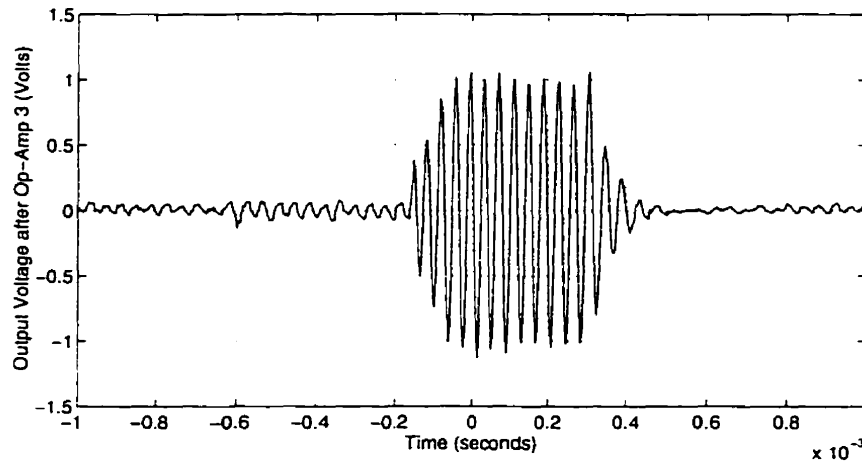


Figure 3.17: The signal after $E3$ or point 4 in Fig. 3.11.

is a low-pass filter whose output generated a signal with an acceptable noise level. Therefore, in this case, a simpler circuit was sufficient to provide the performance required. A sample signal taken after the half-wave rectifier, or point 5 in Fig. 3.11, is shown in Fig. 3.18.

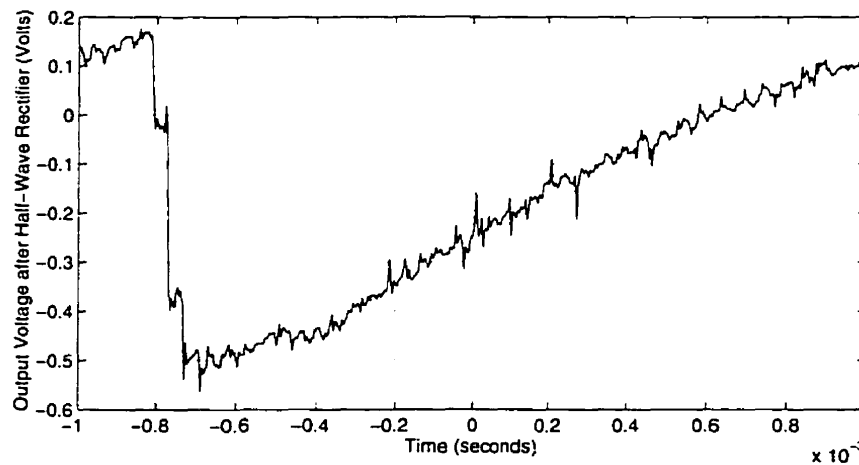


Figure 3.18: The signal after the half-wave rectifier, point 5 in Fig. 3.11.

The last stage of the signal processing circuitry consists of a first order, single op-amp, inverting low-pass filter, see Fig. 3.11. The corner frequency of the low-pass filter must be set so that the filter's rise time is much less than the on-time of each sensor. The on-time of each sensor was $480 \mu\text{s}$ and the corner frequency of this filter

was set at 5.5 kHz . A lower corner frequency would result in a smaller ripple but the filter would not converge on time.

There is one last detail to this filter that merits mentioning. The positive terminal is set to 0.6 V instead of ground. This is done because the half-wave rectification diode will not conduct until the signal at 4 in Fig. 3.11 reaches 0.6 V . Therefore, part of the initial signal is lost and as a result the range of the sensor is reduced. Since our objective is to maximize the sensor's range, this problem is solved by setting the positive pin of $E4$ to 0.6 V . Therefore, since the range of the signal at 4 is $[0, -3.5]\text{ V}$, the diode will conduct throughout this range. A sample signal taken after $E4$, or point 6 in Fig. 3.11, is shown in Fig. 3.19. The noise level on the output signal is less than 100 mV . This signal is sampled by the HC11 microcontroller at -0.1 ms in Fig. 3.19.

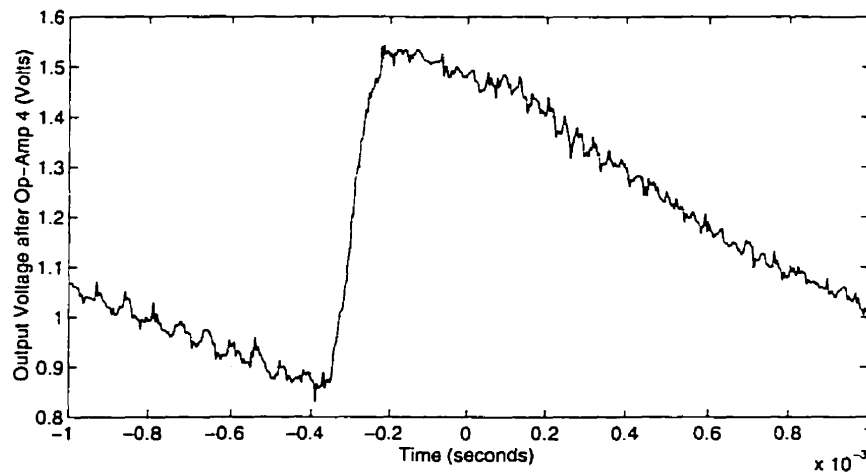


Figure 3.19: The signal after $E4$ or point 6 in Fig. 3.11.

3.5 HC11 Microcontroller

The drastic reduction in size and cost of single-chip microcontrollers has made it possible to develop our PSN board using the 8 bit Motorola MC68HC11E2 microcontroller chip. The job of the microcontroller is to continuously read the analog signals from

the sensors and transmit this data to an external host for further processing upon request.

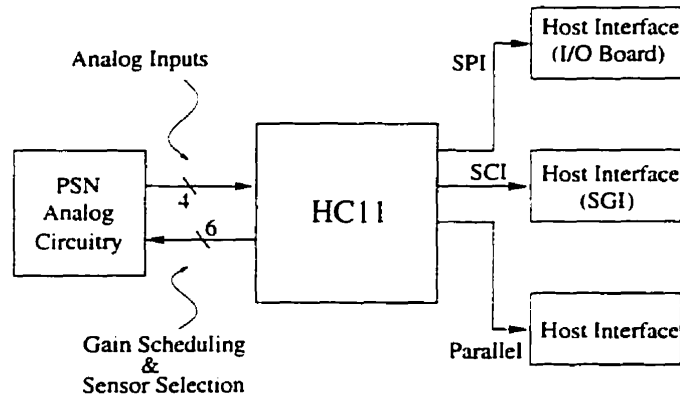


Figure 3.20: HC11 input/output structure.

In Fig. 3.20, a block diagram shows all the external connections to the HC11. The HC11 receives as input the four analog signals from the signal processing electronics as well as an interrupt signal from the host once data is requested. The HC11 outputs the gain settings and turns on the appropriate sensor using six control lines or six bits. The HC11 also outputs the sensor data to the host once it receives an interrupt signal.

The block diagram showing the structure of the main program stored in the HC11's 2 kilobytes of EEPROM memory is shown in Fig. 3.21. Once the user presses the reset button located on the PSN board, the program begins to execute. The program first initializes its registers, variables and communications. Then, the gain for each of the sensors is set to high. That is, it is assumed that the object is initially out of range of all four sensors. The program then enters an infinite loop where the data from the sensors is continuously monitored and the gains are continuously updated until the host requests this data. Once this request is made, the HC11 enters an interrupt subroutine which provides the host with the latest sensory information. Two sets of data are written to memory to two different arrays. This is done so that if data is requested by the host when the HC11 is writing sensory data to memory, a complete

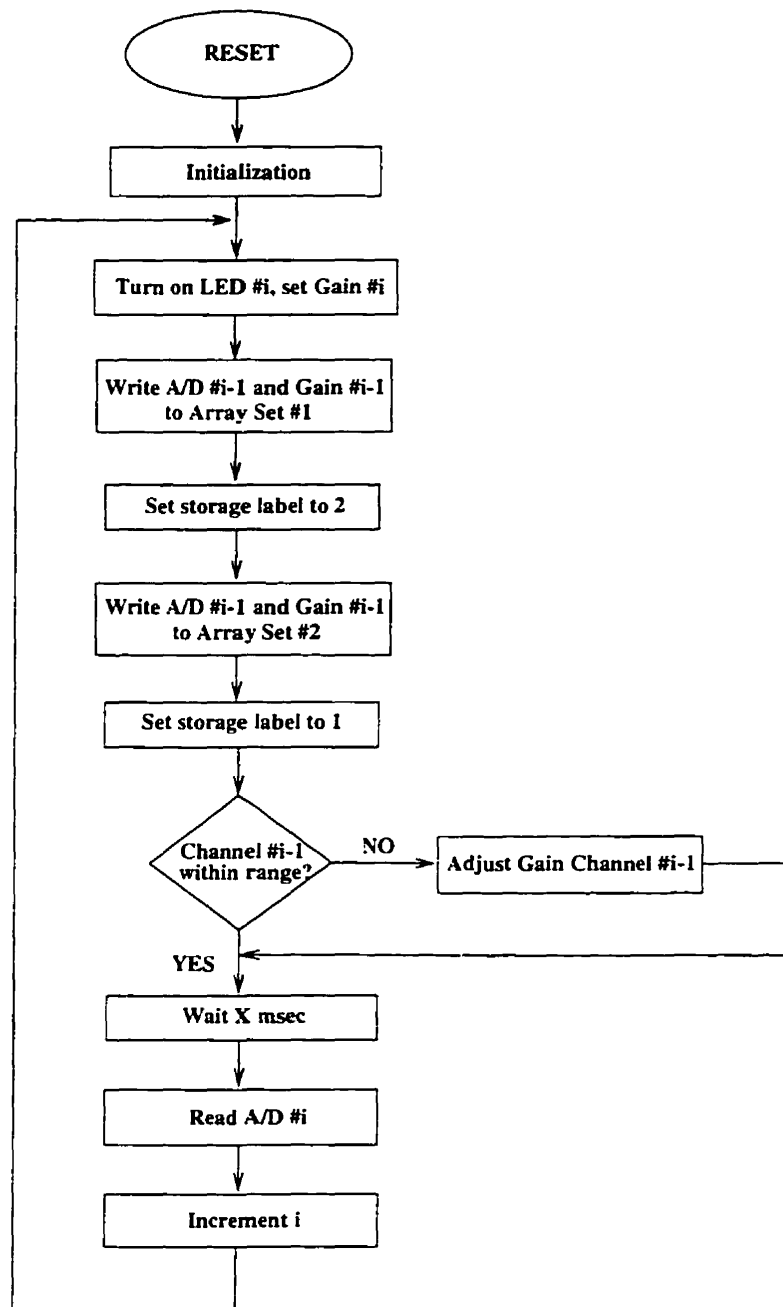


Figure 3.21: Main program flow structure.

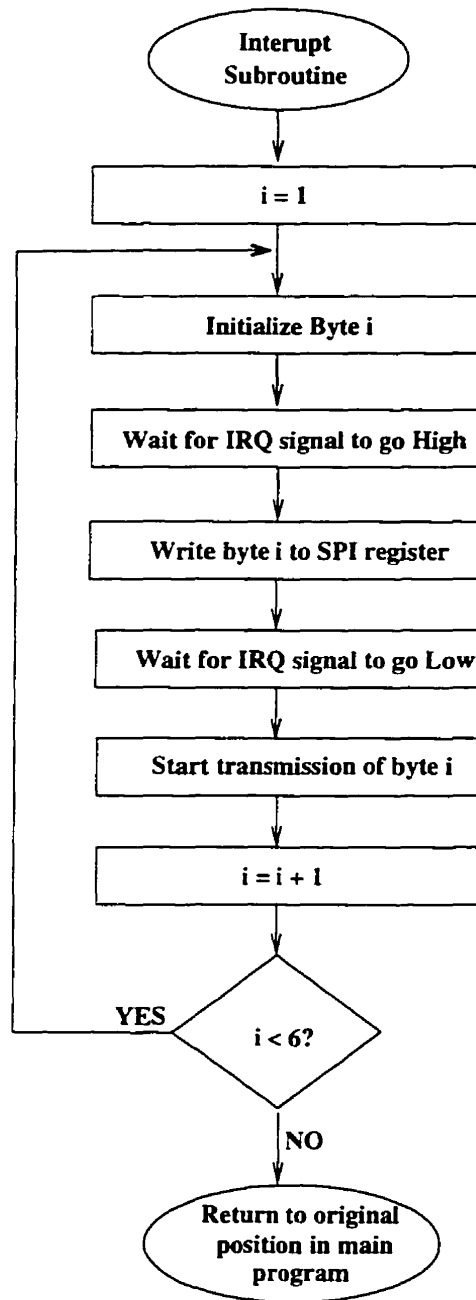


Figure 3.22: Interrupt subroutine flow structure.

set of data is still available to the host. Once this information is transmitted, the program returns to the main program, at the point where it left off.

The interrupt service subroutine used for communicating with a host using SPI communication is shown in Fig. 3.22. The same signal is used to trigger the interrupt subroutine and to synchronize the transmission of the data. A total of 5 bytes are transmitted, 4 bytes are used for the sensor signals and one byte encodes the gain for each channel.

Since the output of the PSN saturates at 3.5 V , the range of the 8 bit A/D's of the HC11 were set between $[0.6, 3.5]$ Volts. Therefore, if there was no gain scheduling implemented, the resolution of the data obtained would be 11 mV . That is, 1 count of the A/D would correspond to 11 mV . By adding gain scheduling, the resolution is improved by approximately 3 times since there are three regions that vary between roughly $[0.6, 3.5]$ Volts.

A photo of the PSN board is shown in Fig. 3.23. All the components used were in a surface mount package in order to reduce the physical size of the board. The development cost for the PSN and sensors was approximately \$350, well below the limit of \$1000 specified in Sec. 3.1.

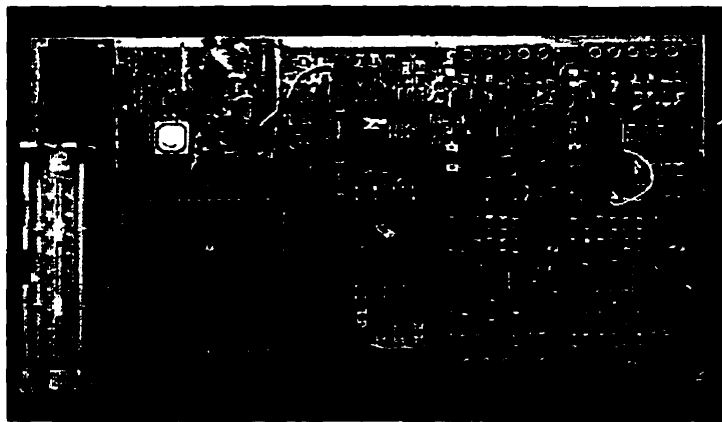


Figure 3.23: A photo of the PSN board (actual size).

Chapter 4

Experimental Results

In this chapter, a description of the experimental procedures and experimental results obtained is presented. In Sec. 4.1, the experimental set-up is described. Both the EBS and PBS sensors are characterized and a sensor model is presented in Sec. 4.2. Testing the sensor's performance under varying ambient light condition is the topic of Sec. 4.3. In Sec. 4.4, the effect of changing the modulating frequency on the sensor signal is investigated. Sec. 4.5 and Sec. 4.6 analyze the effect of emitting a divergent IR beam. Signal drift is the last topic and is discussed in Sec. 4.7

4.1 Experimental Set-Up

The planar experimental set-up shown in Fig. 4.1 was constructed to provide a platform where manipulation and dynamic grasping experiments could be performed. The same test-bed was used to calibrate the sensors as well as gather the experimental data that is presented in this chapter. The set-up consists of two robots, an unactuated RRR robot with high resolution encoders, referred to as "Hobbes" in the figure, and a PPR actuated robot, referred to as "Calvin". "Hobbes" is used to calibrate "Calvin" in a closed loop fashion. "Calvin" is used for manipulation experiments by placing an object on the R-stage and moving the object with respect to the sensors

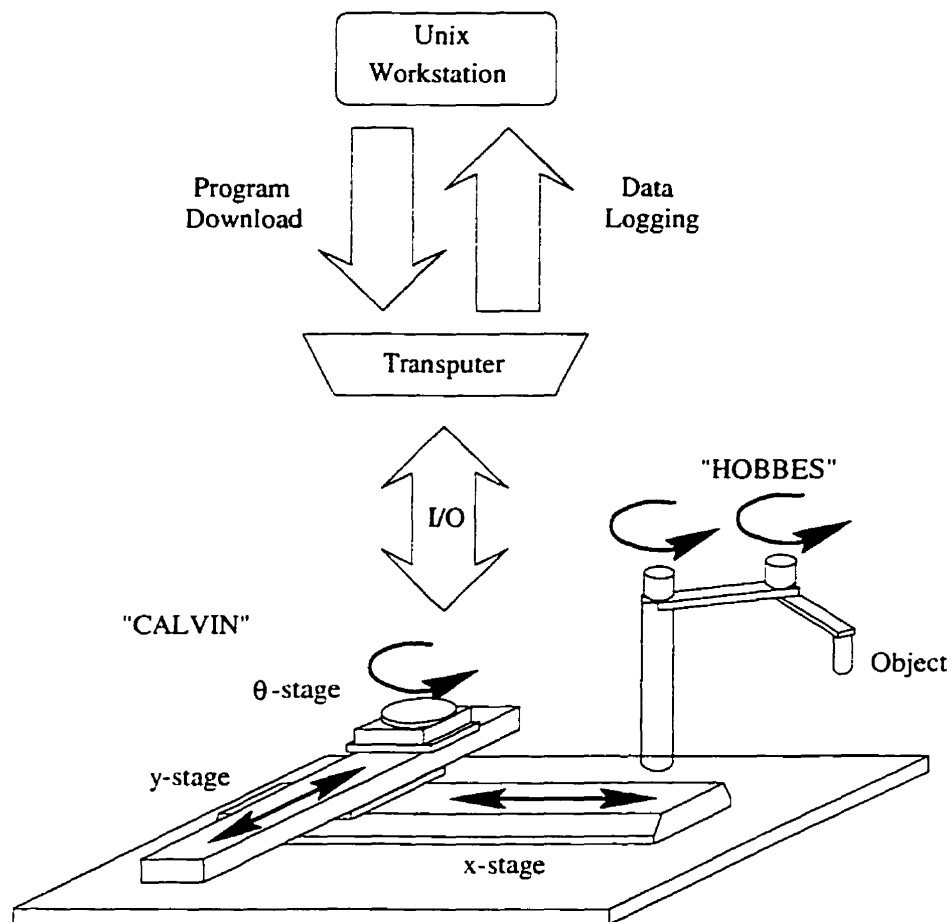


Figure 4.1: Current experimental platform, a PPR actuated robot ("Calvin") and a unactuated RRR robot ("Hobbes"). Courtesy: G. Petryk.

placed in a fixture attached to the base plate. Grasping experiments are performed by placing a parallel jaw gripper on the R-stage equipped sensors and the desired object to track on "Hobbes". Dynamic grasping experiments are the only instance where "Hobbes" is used.

	<i>Travel</i>	Drive train	<i>Peak Motor Torq.</i>
<i>X-Stage</i>	600mm	Belt (1 rev = 90 mm)	4.1Nm
<i>Y-Stage</i>	300mm	Ball Screw (20mm lead)	1.8Nm
<i>θ-Stage</i>	360°, 127mm ϕ	Worm Gear (36:1)	.35Nm

Table 4.1: *Specifications of the PPR robot, "Calvin"*

"Hobbes"' link lengths are 400mm and 200mm for links "one" and "two" respectively. All three encoders have a resolution of 50800 counts/revolution. The last link of "Hobbes" has zero length since it is only used to orient the attached object. Table 4.1 contains a summary of the characteristics of "Calvin's" three components. All three of "Calvin's" motors are equipped with 4096 counts/rev optical encoders. Servo-amplifiers were used to supply the motor currents. The servo-amplifiers were equipped with custom A/D and D/A physically placed inside the servo-amplifiers in order to avoid transmitting analog signals through long cables to and from the transputer network.

Both robots are connected to a transputer network which is made up of one T800 INMOS© processor and one T222 INMOS© processor. An Ethernet connection was established between the transputers and a workstation. Programs were downloaded onto the transputers in order to execute the experiments. Data was uploaded from the transputers in order to post-process the experimental results.

4.2 Characterization Curves

4.2.1 Sensor Calibration

To use the sensors, the output voltage must be related to the variable to be sensed. In this case distance. Unfortunately, the output is also a function of the object's orientation as well as surface properties. Thus, these also must be included in the relation. This relation is the *sensor model* and was derived, in a parametrized form, and then fitted to a set of calibration data. The fit was then validated by error analysis.

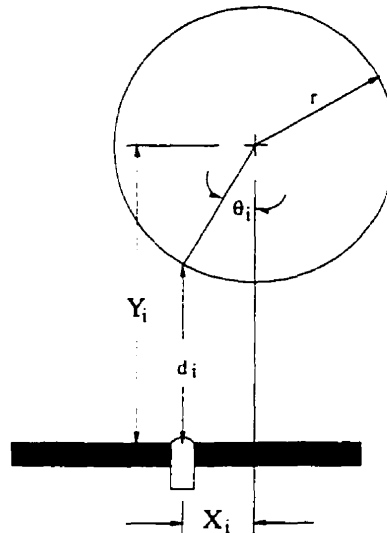


Figure 4.2: Relationship between global and local sensor variables.

The calibration data was obtained by sweeping a circular object with a radius of 32.75mm , covered with white paper, at various positions in front of the sensor. The area swept by the object's centre occupied a 60mm wide, 250mm long rectangle in front of the sensor. Fig. 4.2 shows the relationship between the global coordinates (X, Y) of the centre of the circle and the local sensor coordinates (d, θ) . The analytical relationship between the global coordinates and the local sensor coordinates can be expressed as

$$\theta_i = \arcsin\left(\frac{X_i}{r}\right) \quad d_i = Y_i - r \cos(\theta_i) \quad (4.1)$$

where d_i is the object-sensor distance, θ_i is the angle between the sensor beam and object surface and i denotes the i^{th} sensor since several sensors were calibrated. The *arcsin* function is undefined for $\|X_i\| > r$, therefore the data which did not satisfy this inequality was ignored. The result is a data set of sensor output vs. distance and angle. The albedo parameter or reflectance gain was assumed to be unity for the calibrated object.

To perform this procedure, each sensor was mounted, in turn, on a stationary fixture whose orientation with respect to the planar robot's workspace was known. The object was mounted on the robot. Thus, its position could be measured with an accuracy of 0.02mm , using the robot's actuator encoders. The robot was then commanded to sweep horizontally across the fixed sensor head at a constant sensor-object distance. The object is then positioned at a new sensor-object distance and a new horizontal sweep, in the opposite direction, is performed. The previously described rectangle is the area through which the object is moved.

4.2.2 Data Fitting

Once the data had been collected and transformed into a usable form, it was fit to a parametrized function using a recursive, least squares algorithm. The model used to characterize the sensors' output is

$$h_i(d_i, \theta_i, \lambda) = \frac{\lambda \beta_{1,i}}{(d_i + \beta_{4,i})^{\beta_{2,i}}} \cos(\beta_{3,i} \theta_i) \quad (4.2)$$

where λ is the albedo parameter and $\beta_{1-4,i}$ are the calibration parameters. This model was first developed by Petryk in [23]. The surface was assumed to be Lambertian and as stated in (2.3) and in [15] and [16], the sensor output was assumed to vary with the *cosine* of the angle between the sensor beam and object surface. The three dimensional plot of the raw data collected for the four PBS sensors can be found

in Figs. 4.3 to 4.6 and the same plots are shown in Figs. 4.7 to 4.10 for the EBS sensors. These figures also show the orthogonal projections of the surface fit plot of the function and the error in curve fitting the data.

<i>Sensor</i>	β_1	β_2	β_3	β_4
<i>PBS #1</i>	1327	2.050	0.9682	15.36
<i>PBS #2</i>	980.8	2.034	0.9019	14.62
<i>PBS #3</i>	1025	2.116	0.9260	13.38
<i>PBS #4</i>	780.2	1.912	0.9438	15.52
<i>EBS #1</i>	2115	2.066	0.9637	19.45
<i>EBS #2</i>	5761	2.220	0.9702	25.15
<i>EBS #3</i>	24184	2.521	0.9858	30.70
<i>EBS #4</i>	11341	2.365	0.9764	27.38

Table 4.2: Value of parameters for all 4 PBS and all 4 EBS sensors

To determine the “goodness of fit” of the calibration procedure, the error surface between the raw data points and the calibrated surface was examined. Plots of the orthogonal projections of the error surface are also presented in Figs.4.3 to 4.10.

As can be seen in the previously mentioned error in curve fitting data, the fit has systematic errors. The regions of high error occur between $\theta = \pm 60^\circ$ because of the gain descheduling of the raw signal. One can clearly see a ridge in the sensor output surface at $d \approx 20mm$ corresponding to the change from low gain to high gain. The errors in the regions of high target-object angle are due to the unmodelled conical shape of the sensor’s emitted infra-red light. Thus, at large distances a detectable signal is registered even though the object is out of the sensor’s visual axis.

The range of each sensor was determined by examining its characterization curve and determining the distance at which the signal reached a level that was 97.5% of the difference between the maximum signal and the value to which the output converges as the object is moved away. The results are tabulated and shown in Table

4.3. The average range of the PBS sensors was 9.0 *cm* and the average range of the EBS sensors was 11.2 *cm*. The average range of the PBS sensors did not satisfy the specified requirement of 10 *cm*, although PBS sensor #4 was within the requirements. Therefore, this shows that it would be possible to manufacture a PBS sensor whose range is greater than 10 *cm*.

All EBS sensors met the range specification. Since the shape of the characterization curves for all sensors is dictated by physics, they all have the same shape. The maximum sensor output is 3.5 *V*, which was set by the PSN gains. Therefore, any difference in the range of the sensors is attributed to the amount of noise in the signal. The EBS sensors emit a more intense IR beam which decreases the signal noise since a lower gain is required to amplify the raw signal to 3.5 *V*.

	<i>PBS #1</i>	<i>PBS #2</i>	<i>PBS #3</i>	<i>PBS #4</i>	<i>EBS #1</i>	<i>EBS #2</i>	<i>EBS #3</i>	<i>EBS #4</i>
<i>Range</i>	9.1 <i>cm</i>	8.8 <i>cm</i>	7.6 <i>cm</i>	10.5 <i>cm</i>	10.6 <i>cm</i>	11.8 <i>cm</i>	11.1 <i>cm</i>	11.4 <i>cm</i>

Table 4.3: *The effective range of all eight sensors developed*

4.3 Ambient Light and Biasing Effects

Both ambient light and constant biasing current affect the sensors in the same way; there is an increase in the base line or DC voltage at R_1 in Fig. 3.11. Therefore, the ability of the PSN to filter ambient light was investigated by simply varying the base current of the phototransistor. For the PBS sensor, this could not be done since there was no access to the base pin. Instead, ambient light was used to increase the DC component of the collector current. For the EBS sensor, a constant current was applied at the base pin of the phototransistor.

In Fig. 4.11, the distance between the object and the sensor was kept constant while the DC component of the collector current was varied for one PBS and one EBS sensor. It can be seen that the output signal initially increases as the DC component of the

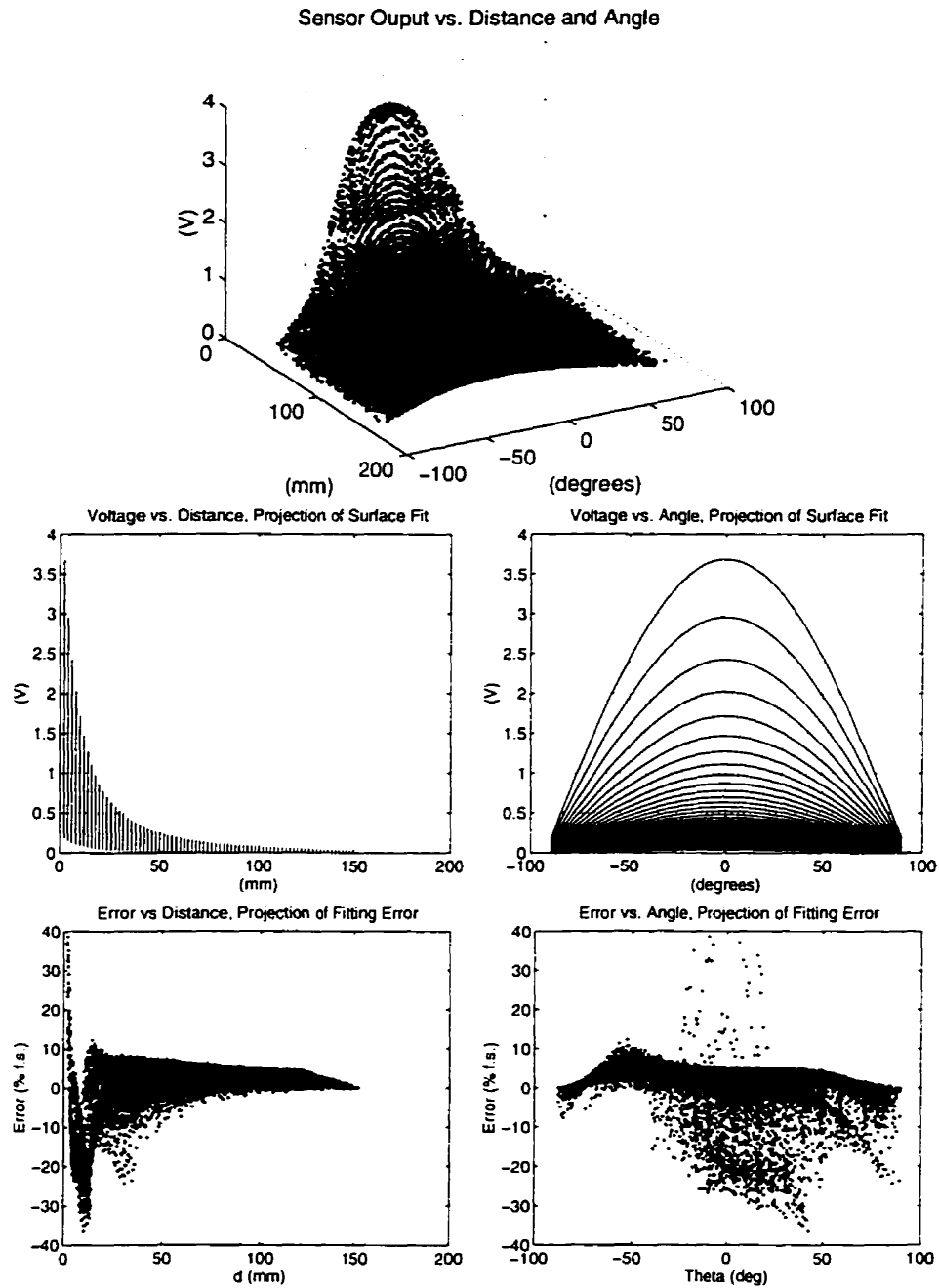


Figure 4.3: Raw data obtained from PBS sensor #1 (top). Fitted sensor output as a function of distance (middle left). Fitted sensor output as a function of orientation (middle right). Error in curve fitting raw data as a function of distance (bottom left). Error in curve fitting raw data as a function of orientation (bottom right).

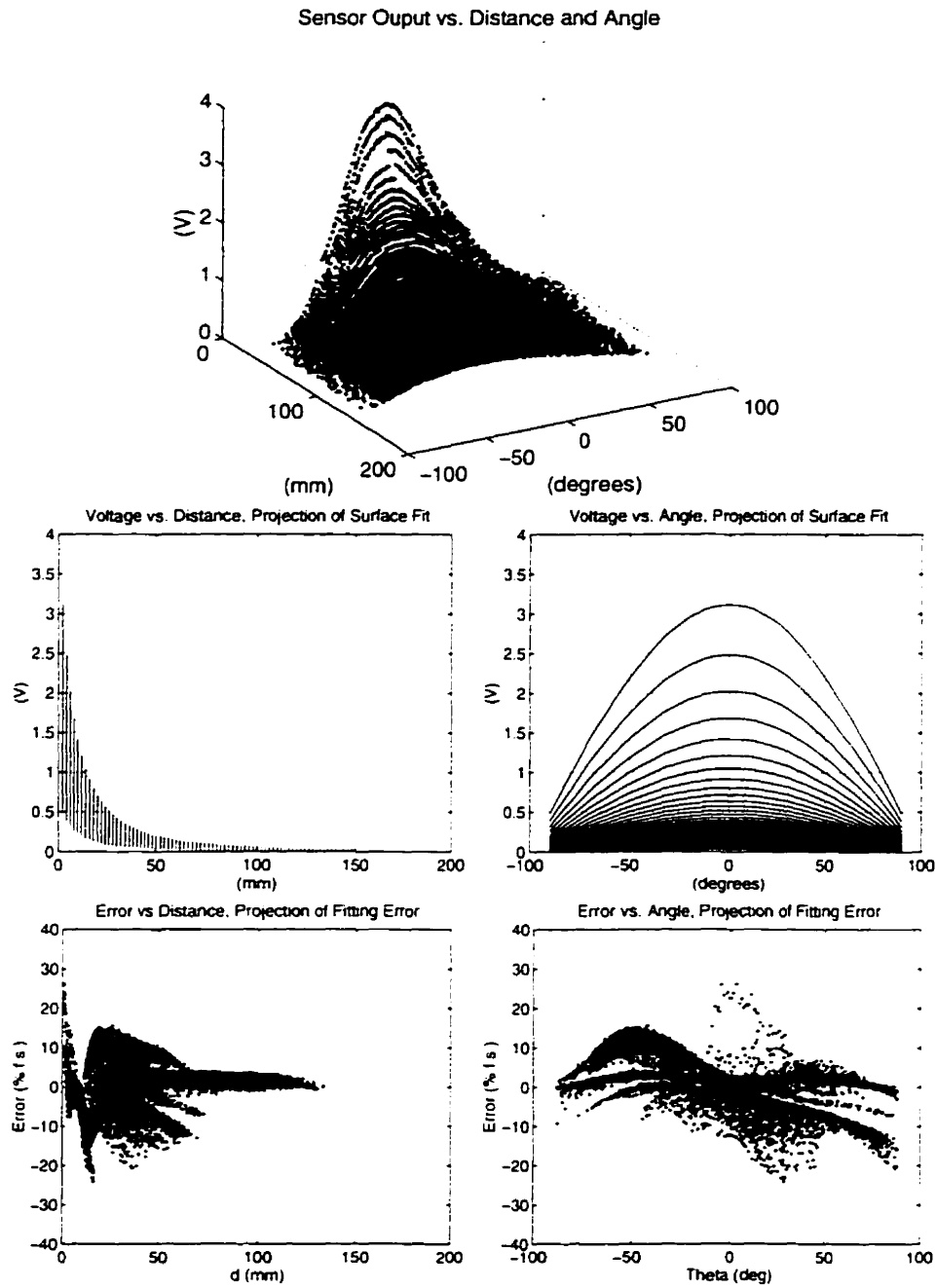


Figure 4.4: Raw data obtained from PBS sensor #2 (top). Fitted sensor output as a function of distance (middle left). Fitted sensor output as a function of orientation (middle right). Error in curve fitting raw data as a function of distance (bottom left). Error in curve fitting raw data as a function of orientation (bottom right).

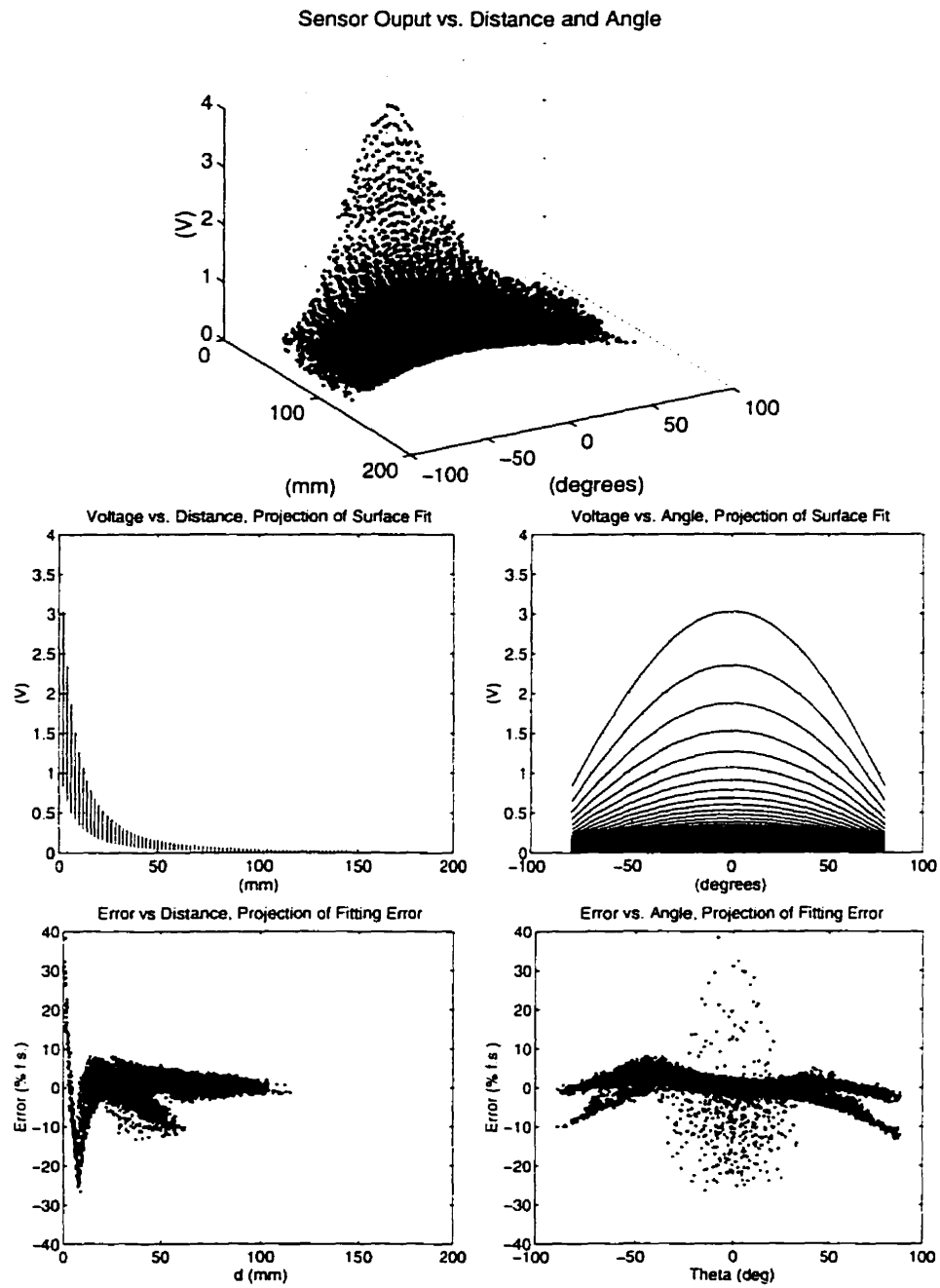


Figure 4.5: Raw data obtained from PBS sensor #3 (top). Fitted sensor output as a function of distance (middle left). Fitted sensor output as a function of orientation (middle right). Error in curve fitting raw data as a function of distance (bottom left). Error in curve fitting raw data as a function of orientation (bottom right).

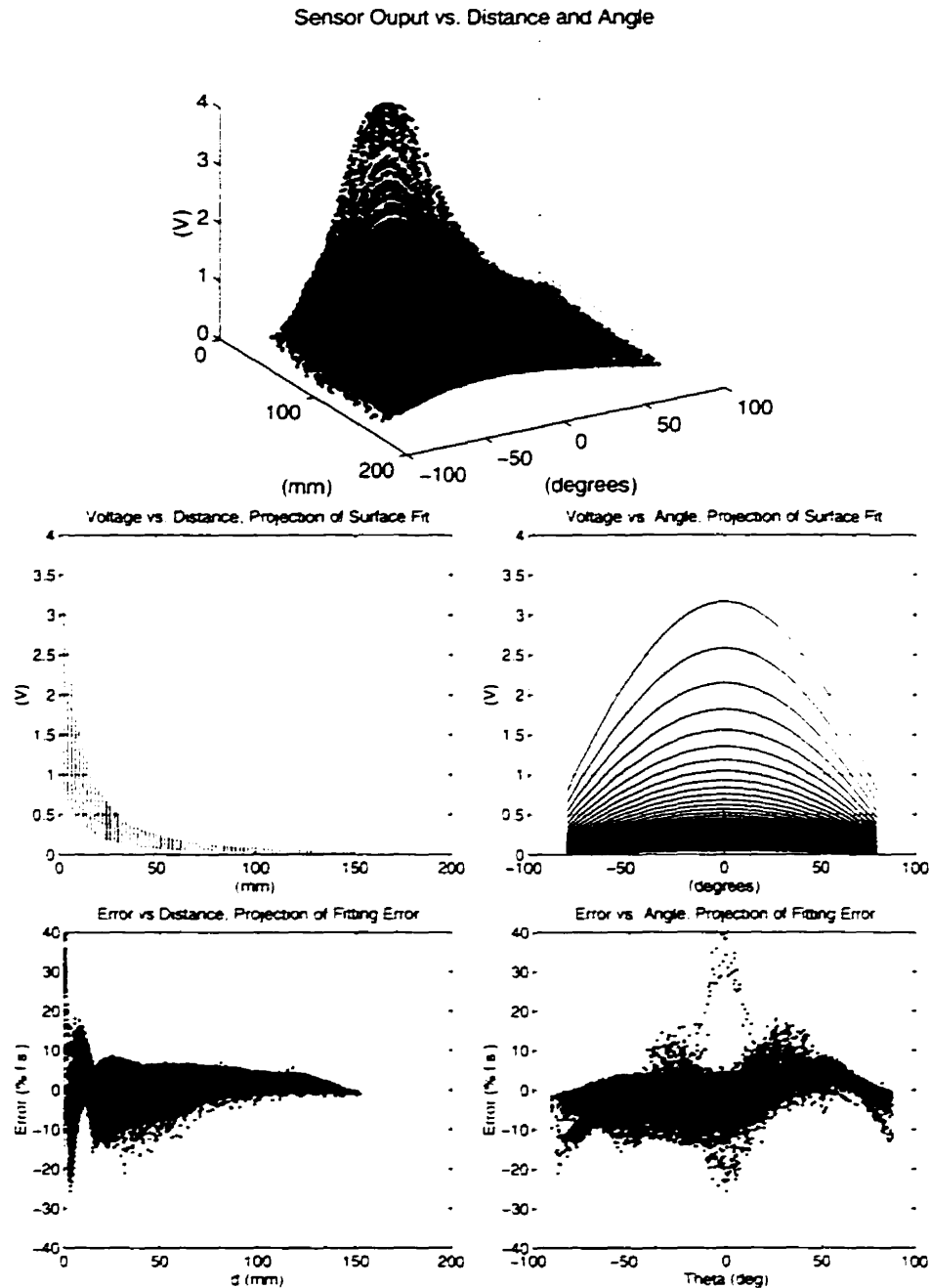


Figure 4.6: Raw data obtained from PBS sensor #4 (top). Fitted sensor output as a function of distance (middle left). Fitted sensor output as a function of orientation (middle right). Error in curve fitting raw data as a function of distance (bottom left). Error in curve fitting raw data as a function of orientation (bottom right).

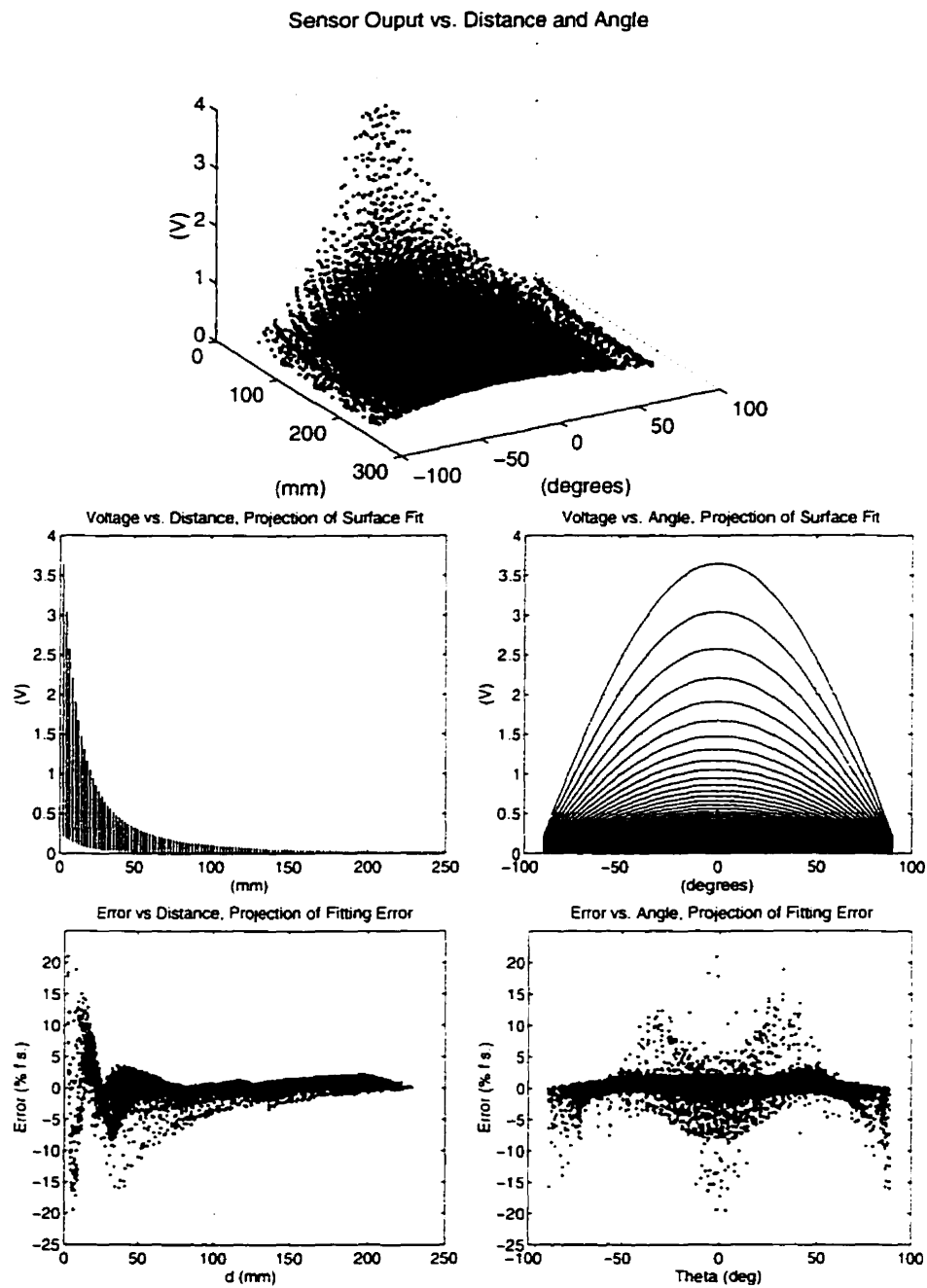


Figure 4.7: Raw data obtained from EBS sensor #1 (top). Fitted sensor output as a function of distance (middle left). Fitted sensor output as a function of orientation (middle right). Error in curve fitting raw data as a function of distance (bottom left). Error in curve fitting raw data as a function of orientation (bottom right).

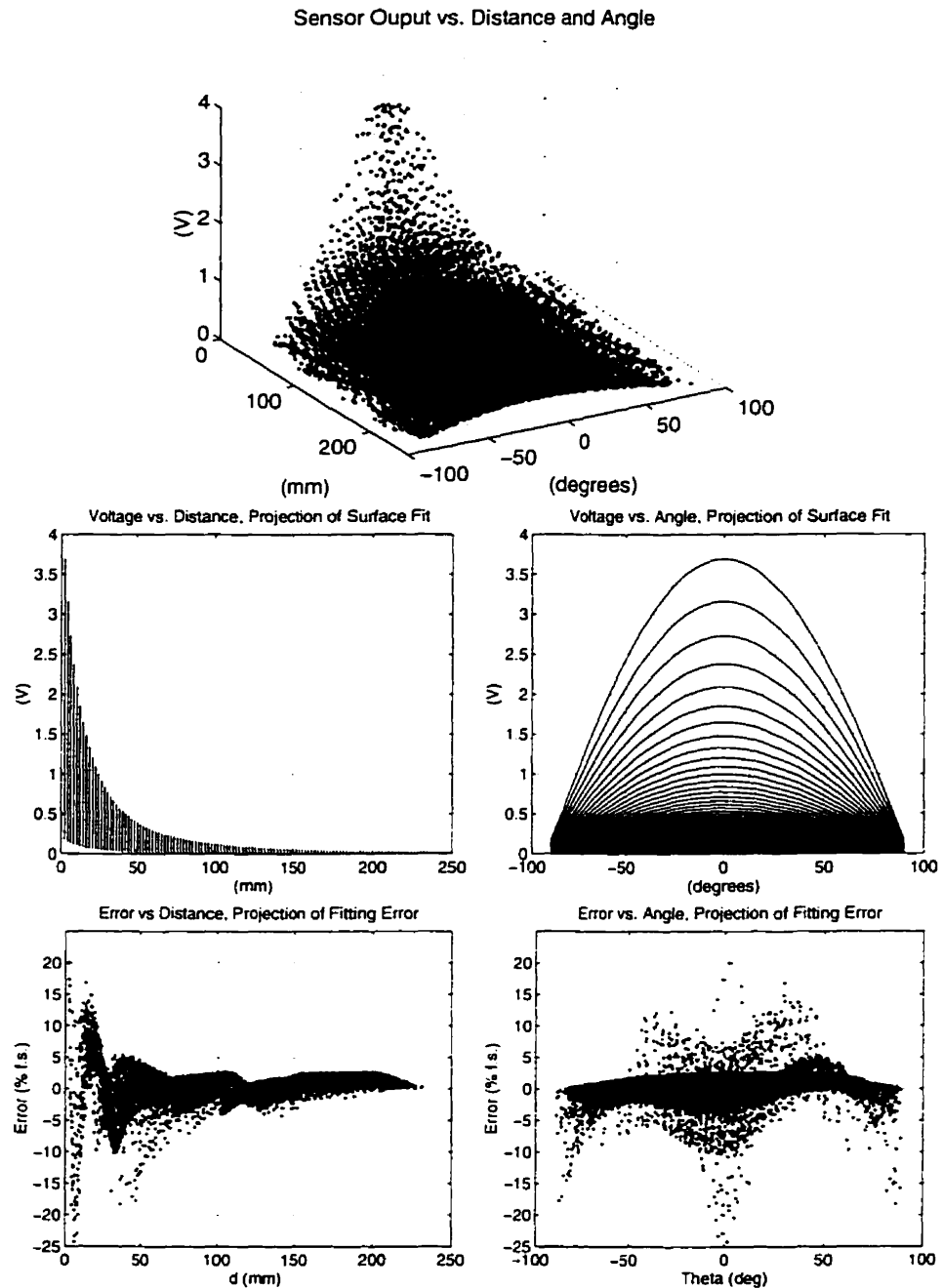


Figure 4.8: Raw data obtained from EBS sensor #2 (top). Fitted sensor output as a function of distance (middle left). Fitted sensor output as a function of orientation (middle right). Error in curve fitting raw data as a function of distance (bottom left). Error in curve fitting raw data as a function of orientation (bottom right).

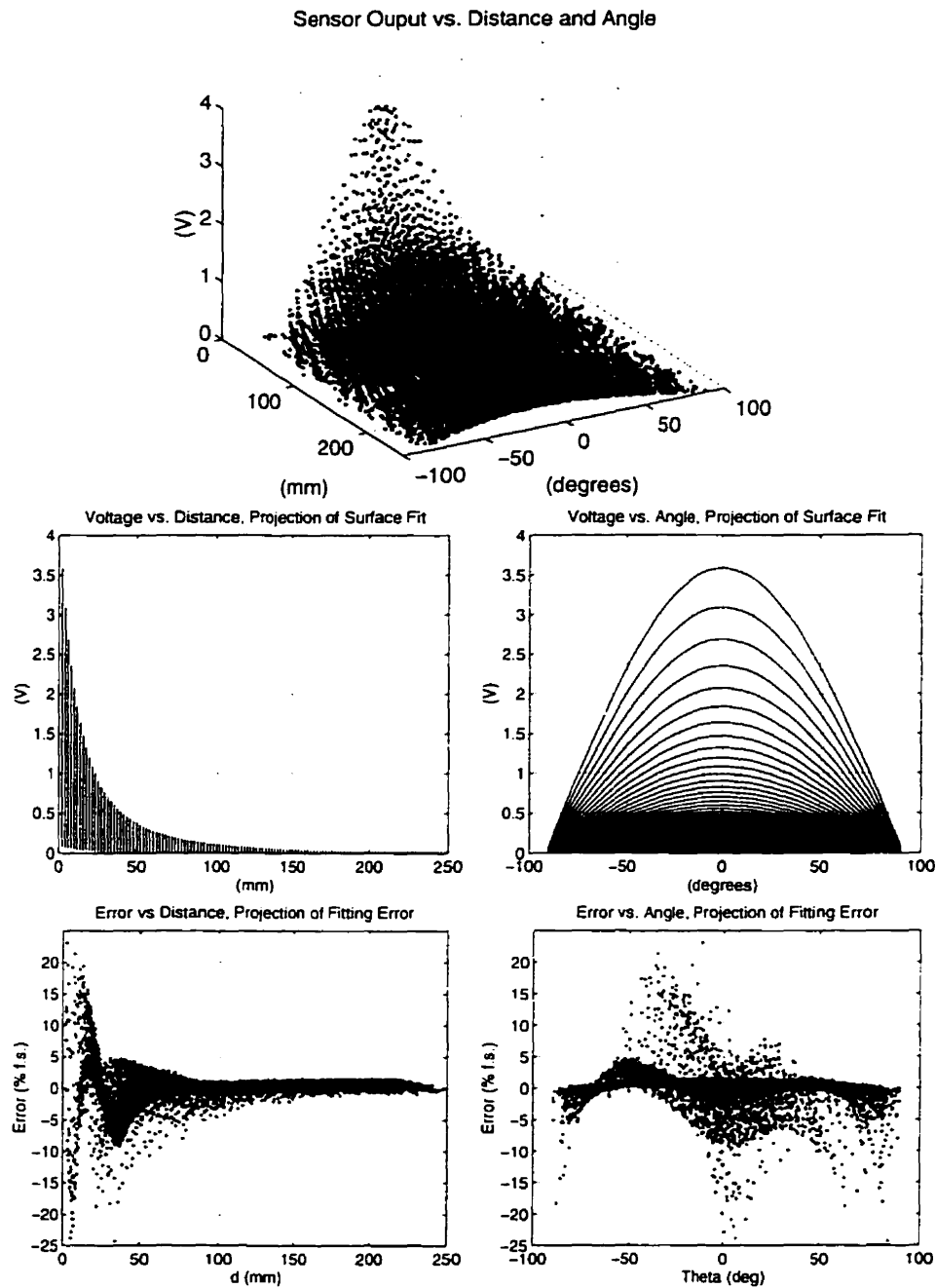


Figure 4.9: Raw data obtained from EBS sensor #3 (top). Fitted sensor output as a function of distance (middle left). Fitted sensor output as a function of orientation (middle right). Error in curve fitting raw data as a function of distance (bottom left). Error in curve fitting raw data as a function of orientation (bottom right).

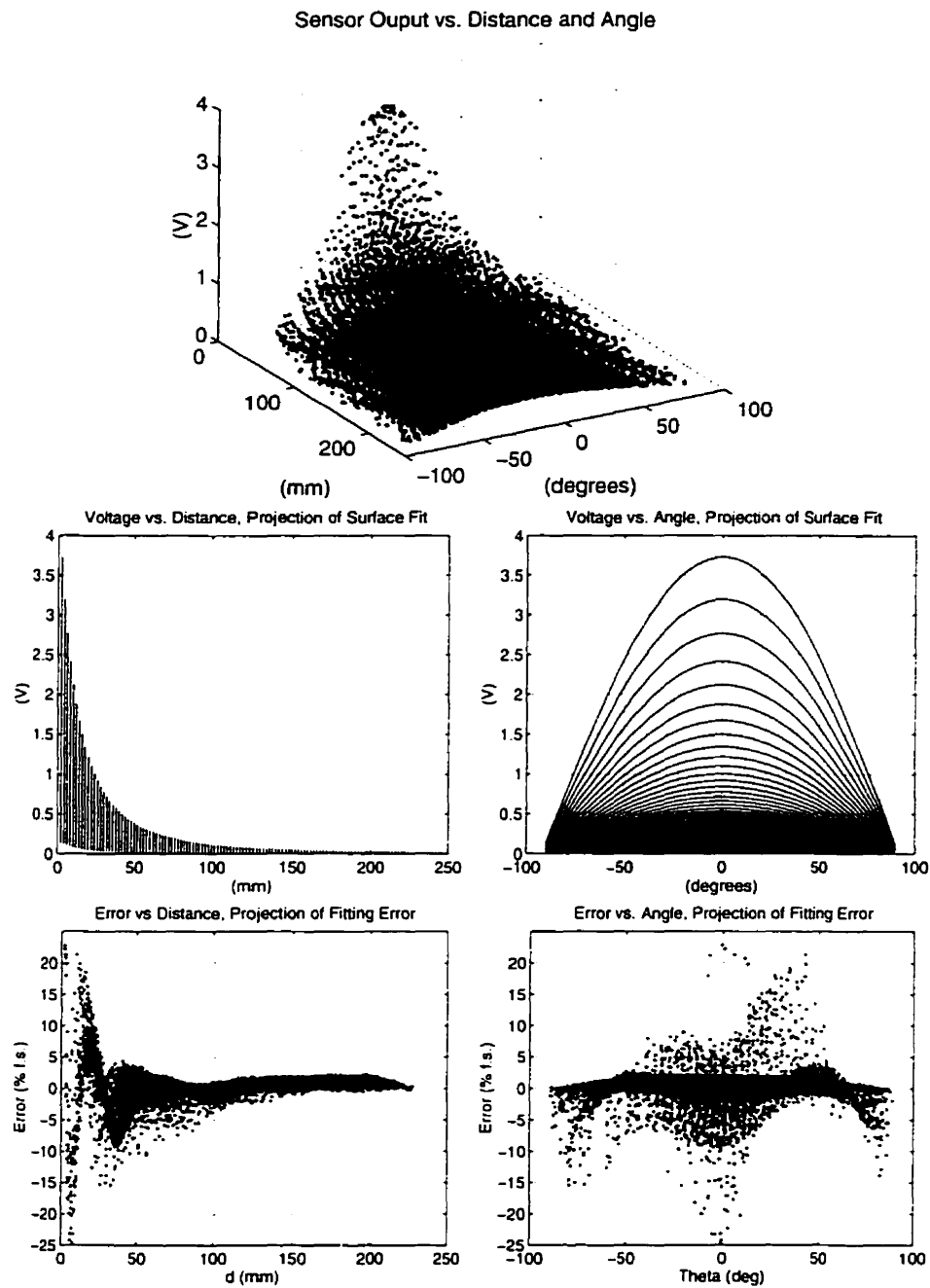


Figure 4.10: Raw data obtained from EBS sensor #4 (top). Fitted sensor output as a function of distance (middle left). Fitted sensor output as a function of orientation (middle right). Error in curve fitting raw data as a function of distance (bottom left). Error in curve fitting raw data as a function of orientation (bottom right).

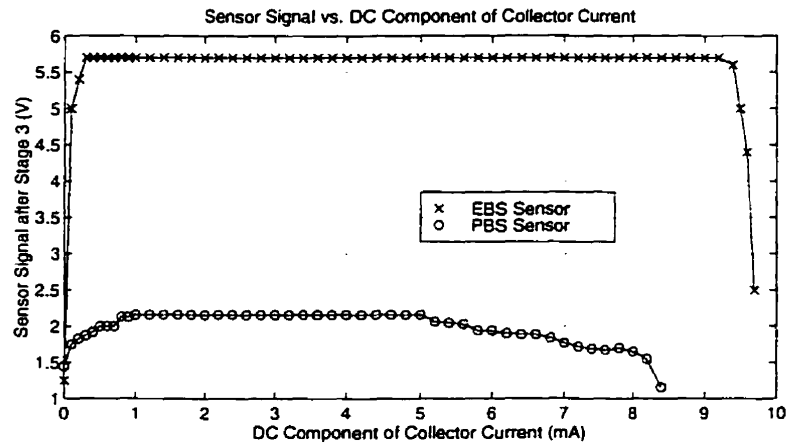


Figure 4.11: The effect of increasing the DC component of the collector current of the phototransistor on the sensor signal with an object maintained at a constant distance.

collector current increases. This is due to the non-linear effect of the phototransistor, an increase in gain of the phototransistor caused by the increase in collector current. Once the minimum DC current in the collector is supplied, referred to as minimum “biasing” current, the linear region is attained and the sensor’s signal remains constant as the DC component of the collector current or ambient light intensity increases. Finally, if the collector current is increased by a large amount, the phototransistor is saturated and the output signal of the sensor starts to drop off.

The EBS sensor output shown in Fig. 4.11 remains constant over a larger range of collector DC current levels compared to the PBS sensor. The PBS sensor signal begins to drop off at a significantly lower current level. This difference can be attributed to the two different phototransistors used. That is, the *OP644SL* used in the PBS sensor does not respond as well as the *OP804SL*, used in the EBS sensor. The ambient light data presented in Fig. 4.11 is in milliamps of current through the collector of the phototransistor. This data can be converted to irradiance using the data sheets provided in Appendix A. For the *OP644SL*, the solar constant, 135.3 mW/cm^2 , which is the solar energy incident on a surface oriented normal to the sun’s rays when the earth is at its mean distance from the sun, would correspond to 42.3 mA . Therefore,

the sensors can operate without any problem under indoor lighting conditions but would be inoperative if pointed directly into the sun.

These curves show that a minimum “biasing” current is required in order to successfully filter ambient light effects. The PBS sensors require a “biasing” current of approximately 1 mA while the EBS sensors only require as little as 0.3 mA . Finally, an excessive amount of ambient light renders the sensors inoperable. The PBS sensor signal begins to attenuate at 5 mA of collector current where as the EBS sensor signal drops off sharply at 9.2 mA . The EBS sensor performance in terms of ambient light rejection is much better than the PBS sensor since its signal remains constant over a larger range of current levels.

4.4 Modulating Frequency Effects

4.4.1 Effect on PSN Output

The LEDs are modulated at a fixed frequency of 25 kHz . The bandwidth of the EBS phototransistor is approximately the same as the modulated frequency. The PBS phototransistor’s speed is approximately 200 kHz . The effect of changing the frequency for a given constant output signal of the sensor was tested. The frequency selected to modulate the LED must be large enough to allow the band-pass filter to successfully filter the 60 Hz ambient light signal. Modulating the signal at very high speeds would surpass the bandwidth of the given phototransistor. If this is done, the sensor output is attenuated and as a result the range of the sensor is diminished. Modulating at a low frequency is undesirable since the overall speed is reduced due to that ten to twelve cycles of the modulated signal are required for the filters to settle and thus obtain a constant *DC* signal.

The following experiment was carried out to investigate the effect of the modulating frequency on the sensor output. An object was placed at a constant distance from the sensor and the output of the PSN was recorded as the modulating frequency was

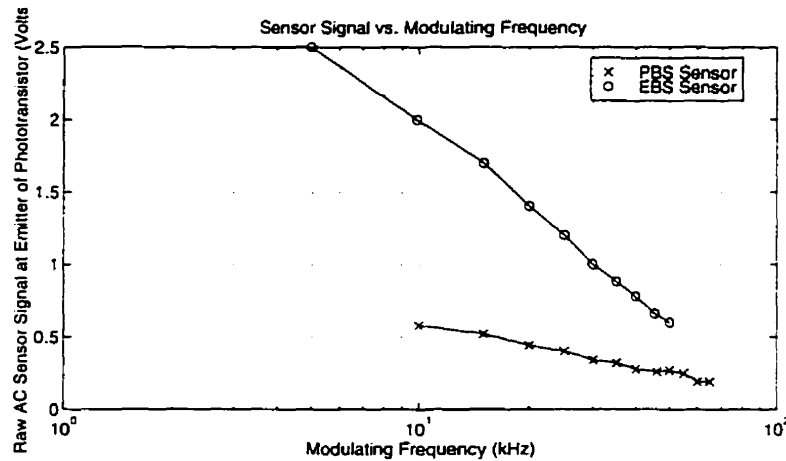


Figure 4.12: The effect of increasing the modulating frequency on the sensor with an object maintained at a constant distance.

varied. The results for one PBS sensor and one EBS sensor are shown in Fig. 4.12.

The output signal is maximum at the lowest frequency and varies approximately linearly with respect to the logarithm of frequency. Therefore, selecting the optimum modulating frequency is a trade-off. A higher modulating frequency is desirable since this would increase the PSN's bandwidth. A lower modulating frequency reduces the PSN's bandwidth but also increases the sensor's signal and, thus, range. Since the initial specifications of the PSN stated that the PSN bandwidth should be no less than 500 Hz , this bandwidth was used to calculate the minimum modulating frequency possible. Therefore, since the filters required thirteen cycles per "on-time" to converge, the lowest possible modulating frequency is 25 kHz . In order to maximize the sensor response, 25 kHz was used as the modulating frequency.

4.4.2 Effect on DC Output of Phototransistor

Determining the effect of modulating at 25 kHz on the DC signal generated by the phototransistor is investigated here. The transformation the original signal emitted by the LED goes through before it is processed by the analog electronics is shown in Fig. 4.13. The original signal is modulated at 25 kHz and has a certain DC offset since

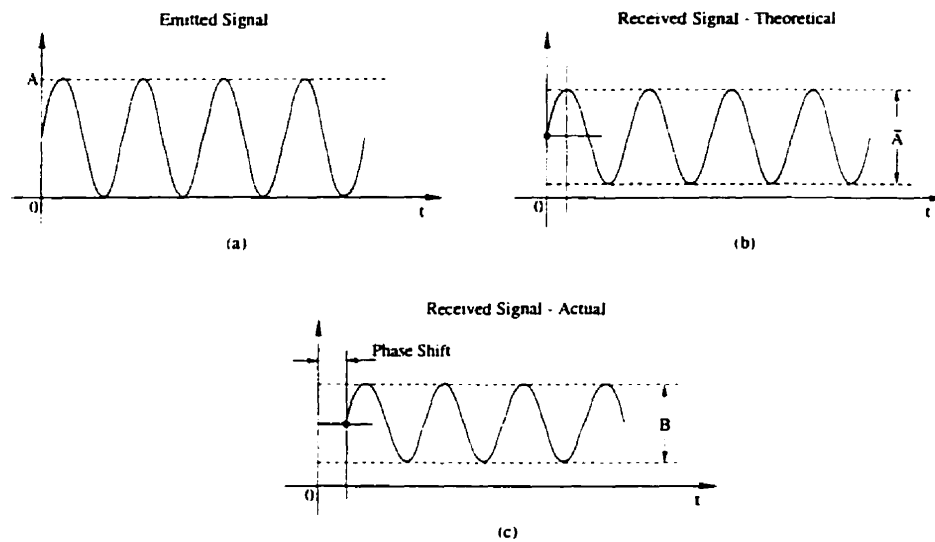


Figure 4.13: The sensor at three different stages (a) at the LED (b) the theoretical signal returned by a diffuse surface (c) the signal measured by the phototransistor.

it is impossible to modulate light around zero. The signal is reduced in amplitude as it undergoes diffuse reflection from the object's surface. Finally, the signal is detected by the phototransistor which acts as a low-pass filter. That is, the frequencies at which the sensor detects a signal are limited by the devices' bandwidth. Therefore, the final signal measured is attenuated slightly depending on the bandwidth of the phototransistor and also experiences a phase shift, Fig. 4.13(c). The signal measured by the phototransistor contains a *DC* offset, X . This offset is a function of the object distance. That is, as the sensor signal increases, the *DC* shift also increases. Characterizing this *DC* shift is the focus of this section.

The *DC* component of the sensor's raw signal was measured as the sensor-object distance was varied. This experiment was performed using one PBS and one EBS sensor. The results from this experiment are presented in Fig. 4.14.

From this data, it can be seen that the PBS sensor has a much smaller *DC* component than the EBS sensor. This can be attributed to the larger signal being transmitted by the four LEDs in the EBS sensor compared to the one in the PBS sensor. Also, the EBS phototransistor has a larger surface area, so it detects a larger portion of

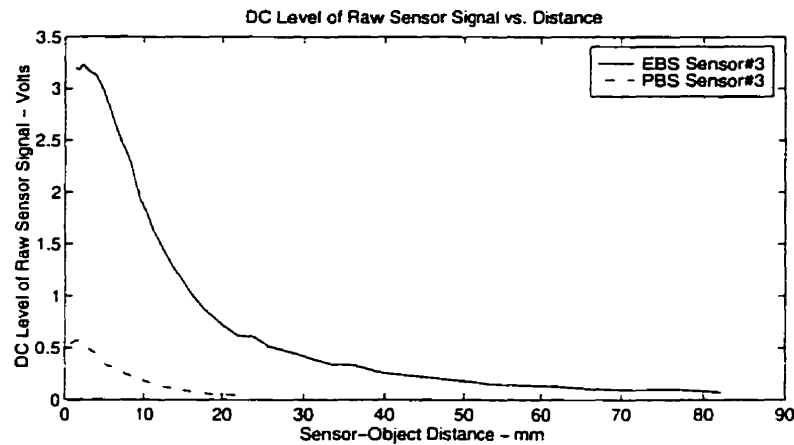


Figure 4.14: The DC offset of the raw signal for one PBS and one EBS sensor.

the incoming signal. A larger sensor output infers a larger DC component. This DC component is filtered from the AC signal along with the ambient light disturbances. This signal may affect the range of the sensor since the signal is shifted closer to the upper limit of $3.5V$. The only way to avoid saturating the signal is to use a larger voltage range on the phototransistor. This did not pose a problem for the EBS sensor since the range used was $[-5, 3.5]$ Volts.

4.5 Object Size Effects

The LEDs used emit an IR beam at a narrow angle: 80% of the LED intensity is within a 15° cone. As a result, the size of the object the sensor can detect varies as the distance of the object from the sensor changes. The effect of varying the object size on the sensor's output is shown in Fig. 4.15. The object used was a square plane with each edge measuring either 1 cm , 2 cm , 4 cm or 6 cm . The test was performed using one PBS sensor and one EBS sensor.

The data shows that as the object size increases from 4 cm to 6 cm , the change in sensor signal is small. But, as the object size decreases below 4 cm , the sensor signal is increasingly reduced. For the PBS sensor, the signal remains constant up

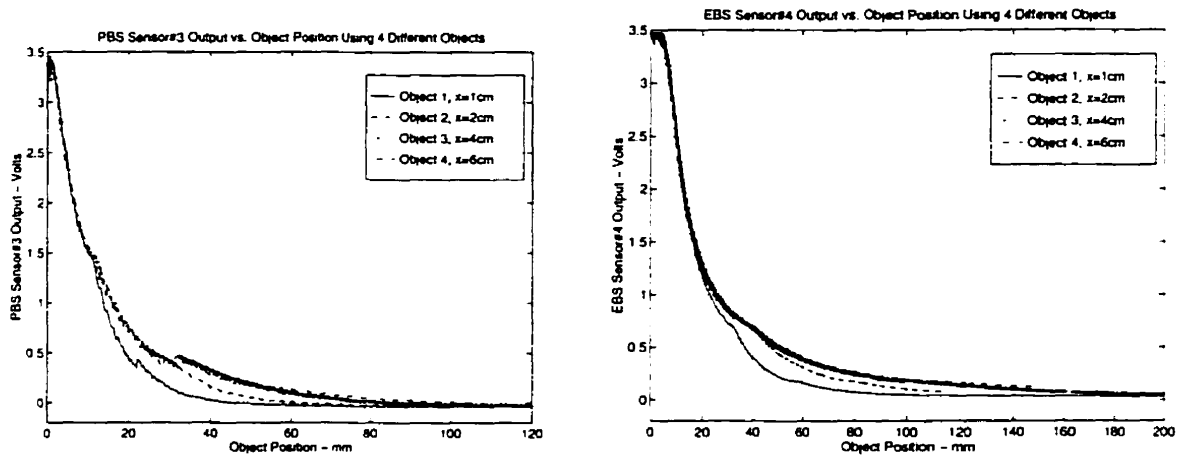


Figure 4.15: The effect of increasing the size of the object on the sensor output using one PBS sensor (left) and one EBS sensor (right).

to 15 mm and then begins to drop off for smaller objects. The signals then begin to converge again at approximately 80 mm. The signals are initially the same for all objects since the beam is quite narrow at close distances. As the distance increases, a larger object is required to reflect the larger sensor beam. At very large distances, the sensor signal converges to a zero reading. Similar characteristics can be seen for the EBS sensor. The results of this test are tabulated in Table 4.4 which can be used as guide in selecting an appropriately sized object at various sensor-object distance operating ranges.

In order to obtain a consistent signal throughout the range of the sensor, a large object should be used. Using a smaller object also reduces the range of the sensor. This problem can be resolved if the emitted beam is collimated. In this case, the minimum object size required for detection throughout the sensor's range would remain constant.

<i>Distance</i>	Minimum Object Size (PBS Sensor)	Minimum Oject Size (EBS Sensor)
10 mm	2 cm	1 cm
20 mm	2 cm	2 cm
32 mm	4 cm	2 cm
44 mm	4 cm	4 cm
57 mm	6 cm	4 cm
110 mm	6 cm	6 cm

Table 4.4: A tabulated guide to the minimum object size required at different sensor-object distances in order to maintain the sensor signal

4.6 Lobe Size Determination

Using a non-collimated beam also results in a beam whose effective area varies as a function of sensor-object distance. The following experiment was performed in order to investigate the effect of using a diverging beam. The sensor signal was recorded as the object was moved from left to right while maintaining the perpendicular sensor-object distance constant. This was done at several sensor-object distances using both one PBS sensor and one EBS sensor. The resulting experimental data is presented in Fig. 4.16. The curves at each sensor-object distance are normalized since their relative amplitudes would make it impossible to compare them.

The plots show that at the closest distance of 1 mm, the signal drops off sharply as the object moves out of the sensor's view. As the sensor-object distance increases, the drop-off in the signal becomes more gradual due to the increase in the area of the emitted signal. The data also shows that that the width of the sensed region also increases. This sensor characteristic may pose a problem when performing manipulation in a 2 - d or 3 - d environment at large sensor-object distances. Since the horizontal distance of the object was not incorporated in the sensor model, this signal drop at a constant sensor-object distance may be misinterpreted by the Kalman filter

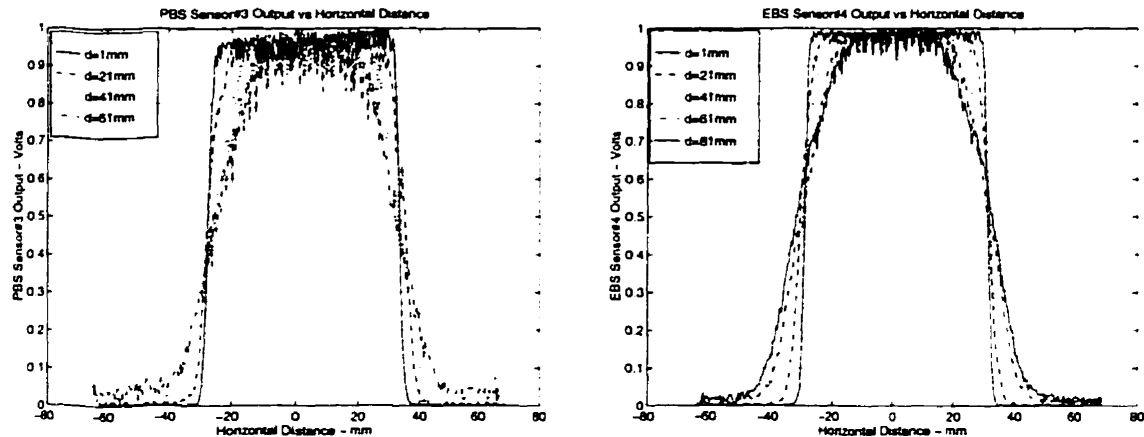


Figure 4.16: The effect of sweeping across at a constant sensor-object distance for a PBS sensor (left) and an EBS sensor (right).

as a change in sensor-object distance or a change in the orientation of the object. Such a misinterpretation may lead to a filter which does not converge. On the other hand, this effect also serves as means to incorporate noise in the Kalman filter in order to determine its robustness. This problem can be avoided by collimating the emitted beam.

4.7 Signal Drift

The effect of signal drift over a long period of time was investigated. Since the LEDs are being driven hard, the heat generated by the LEDs increases the temperature of the sensor heads. This increase in temperature affects the performance of the photo-transistor and as a result the sensors require a certain period of time for their signals to reach a steady state. The sensor output as a function of time while maintaining constant object conditions for four different sensors are presented in Fig. 4.17 and Fig. 4.18. The sensor data was filtered using a second order butterworth low-pass filter with a cut-off frequency of 160 Hz. This was done to clearly show the signal drifting from its initial value.

The following is observed when examining the data taken from the four sensors:

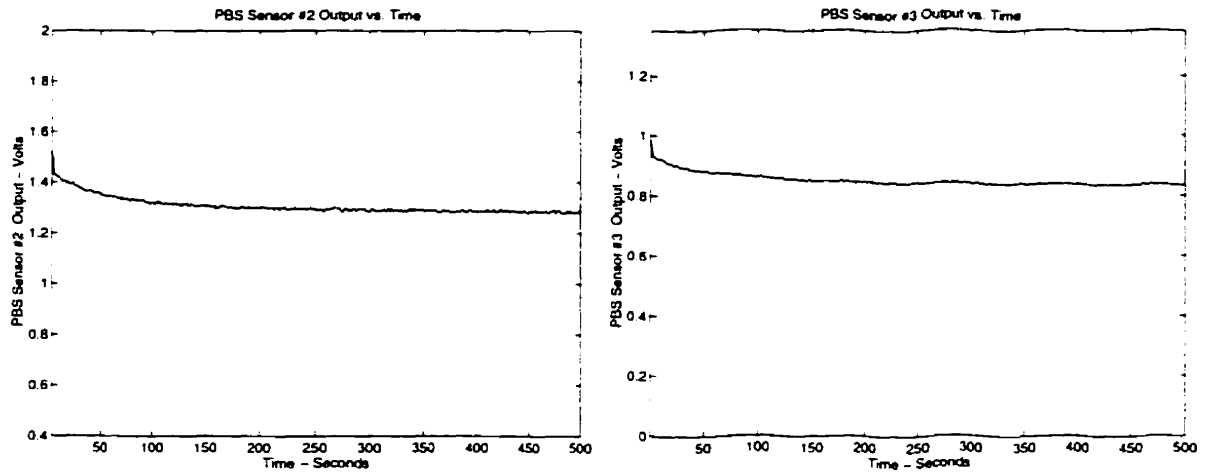


Figure 4.17: The effect of drift on the sensor signal for PBS sensor #2 (left) and PBS sensor #3 (right).

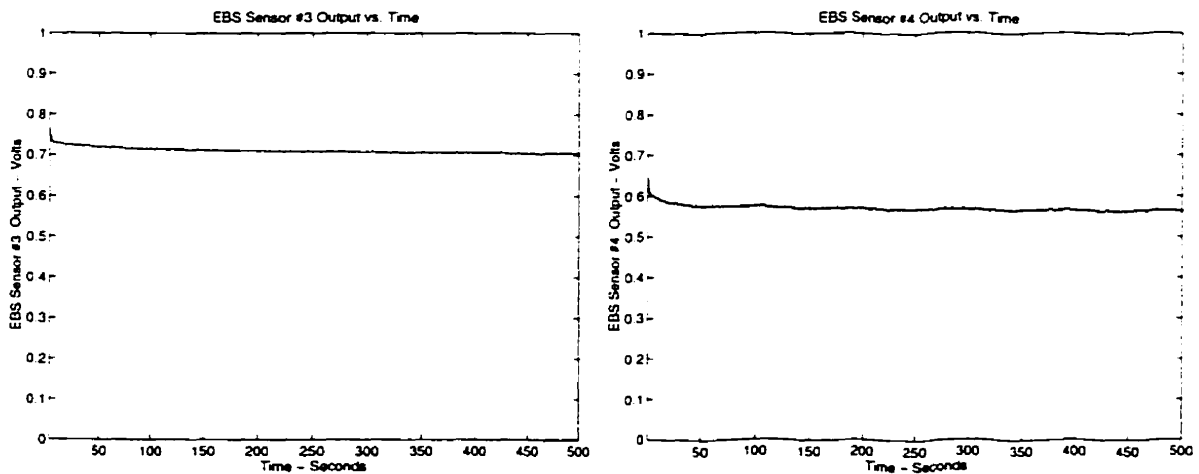


Figure 4.18: The effect of drift on the sensor signal for EBS sensor #3 (left) and EBS sensor #4 (right).

PBS sensor #2 has the largest percent decrease in signal of 18.9%; EBS sensor #3 has the lowest percent decrease in signal of only 8.0%. The PBS sensors drift by a larger amount compared to the EBS sensors. All sensor signals settle within 350 seconds. This experiment was actually run for over 15 minutes , but since no change was found after 350 seconds, the data was cut at 500 seconds for presentation purposes. The results from this experiment pointed out the need for the sensors to be turned on 10 minutes prior to data gathering.

Chapter 5

Conclusions

The main goal of this work was to develop local proximity sensors that could be inserted in the fingers of robotic hand. The sensors would be used in performing manipulation and dynamic grasping experiments. A set of criteria for the sensors was specified. In order to satisfy these requirements, a Proximity Sensor Network was built made up of four infra-red, intensity based proximity sensors. Two types of sensor heads were built, a 'Photon' biased and an 'Electrically' biased sensor. The average range of the PBS sensors was 9.0 *cm*. The average range of the EBS sensors was 11.2 *cm*. The use of four LEDs in the EBS sensor compared to one in the EBS sensor did not drastically increase the range of the sensor. This is expected since the shape of the characterization curve remains the same. That is, the slope at which the signal drops-off remains unchanged and increasing the intensity of the emitted signal will not affect the sensor's range significantly. Therefore, reducing the sensor's noise level is crucial to maximizing its range. Finally, the EBS sensors developed satisfied the specified requirements, whereas the PBS sensors did not attain the specified range.

The accuracy of an individual sensor was not investigated since they are not intended to be used in this way. They are intended to be used as a network and therefore the accuracy of the network is more indicative of the sensor's performance. In [23], the PSN along with an Extended Kalman Filter were used to perform object localiza-

tion. The object geometry is known and its reflective properties or albedo parameter is estimated on-line. The accuracy of the network depends on the object position, object velocity, sensor arrangement and filter parameters. An accuracy of 1 mm in object position was easily obtained using the PSN hardware.

Although the PSN developed performed very well, certain changes should be made to further improve its performance. First, a new layout of the PSN board is required since the original circuit that was constructed does not resemble the final circuit, so certain changes were patched together. The board also operates using a power source with a voltage between $\pm 7.5\text{ V}$ and $\pm 30\text{ V}$. Implementing a unipolar power source would allow the use of a simpler power source such as a battery.

The sensor heads themselves also have room for improvement. The main criteria for making sensor heads are size, ruggedness, consistency and ease of manufacturing. The current heads were quite small, 5.55 mm for the PBS sensor heads and 7.2 mm for the EBS sensor heads. But, even smaller heads are still desirable. Since the manufacturing process was quite tedious and performed manually, the consistency between sensor heads was not very good. Improvement is needed. Finally, the manufacturing process was very difficult and simplifying it is necessary, especially for the PBS sensor heads.

Using gain scheduling is a good way to increase the SNR, and in turn increases the range of the sensor. Unfortunately, the characteristics of each sensor must be almost identical in order to minimize the time to select and tune each gain and switching point. Implementing potentiometers instead of resistors for the components used to tune the gain scheduling is necessary for the next generation PSN board. This would allow the user to fine tune the gains whenever necessary without changing anything on the board. The author also suggests that a simpler way to increase the resolution of the sensor is to use a 12 bit analog-to-digital converter and eliminate gain scheduling and its complexities altogether.

Appendix A

Optek Data Sheets

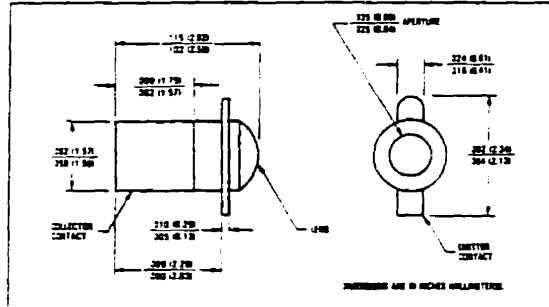
Product Bulletin OP300SL
July 1989 Replaces January 1985



A.1

NPN Silicon Photodarlington

Types OP300SL, OP301SL, OP302SL, OP303SL, OP304SL, OP305SL



Features

- Narrow receiving angle
- Variety of sensitivity ranges
- Enhanced temperature range
- High current gain
- Ideal for direct mounting in PC boards
- Mechanically and spectrally matched to the OP123 and OP223 series devices

Description

The OP300SL through OP305SL series devices consist of NPN silicon photodarlington mounted in hermetically sealed "Pin" type packages. The narrow receiving angle provides excellent on-axis coupling. Photodarlington are normally used in applications where light signal levels are low and more current gain is needed than is possible with phototransistors.

Replaces

OP300 series

Absolute Maximum Ratings (T_A = 25°C unless otherwise noted)

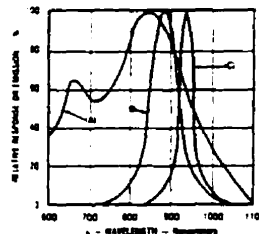
Collector-Emitter Voltage	15.0V
Emitter-Collector Voltage	5.0V
Storage Temperature Range	65°C to +150°C
Operating Temperature Range	65°C to +125°C
Soldering Temperature (5 sec. with soldering iron)	260°C (1/2)
Power Dissipation	50mW ⁽¹⁾
Continuous Collector Current	50mA

Notes:

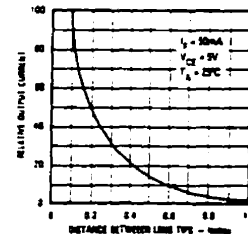
- (1) Refer to Application Bulletin 111 which discusses proper techniques for soldering Pin type devices to PC boards.
- (2) RMA flux is recommended. Duration can be extended to 10 sec. max. when flow soldering.
- (3) Derate linearly 0.5mW/°C above 25°C.
- (4) Junction temperature maintained at 25°C.
- (5) Light source is an unfiltered tungsten cube operating at C_T = 2870°K or equivalent infrared source.

Typical Performance Curves

Spectral Response of OP300-OP305 vs. GaAlAs and GaAs



Coupling Characteristics of OP123 and OP300



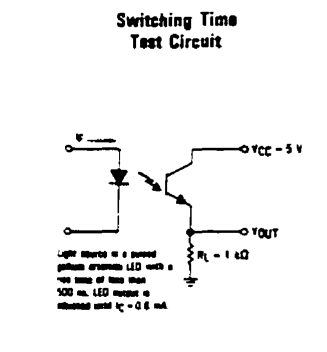
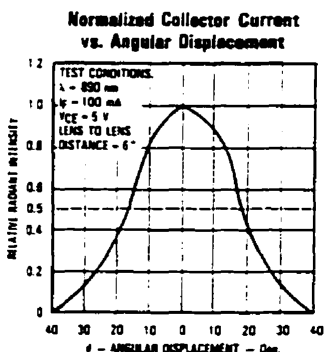
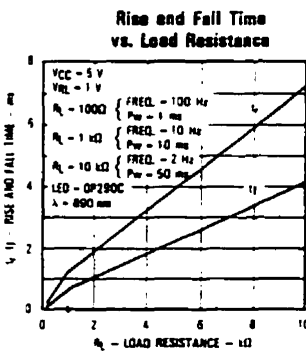
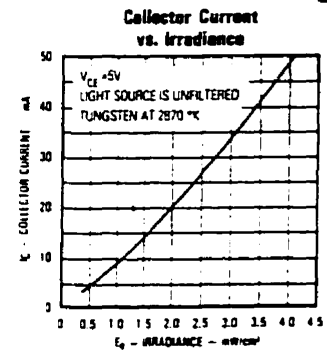
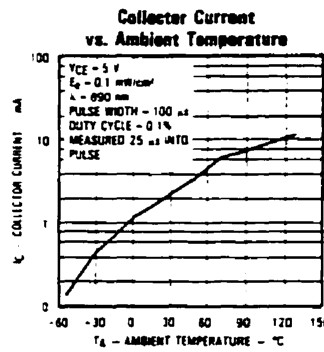
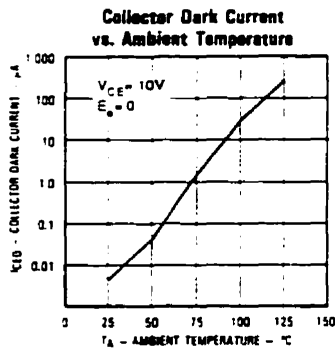
⁽¹⁾ See Condition 6.6B; T_A = T_C = 25°C; I_C = 100 mA
 I_C = 0.1A; P_D = 100 mW
 Peak Wavelength = 850 nm; λ_{1/2} = 2270 - 246 = 20 nm; Δλ_{1/2}
 Substrate = 800 ± 20 nm; Δλ_{1/2} GaAs = 620 ± 15 nm

Types OP300SL Thru OP305SL

Electrical Characteristics (T_A = 25°C unless otherwise noted)

SYMBOL	PARAMETER	MIN	TYP	MAX	UNITS	TEST CONDITIONS	
I _(ON) ⁽⁴⁾	On-State Collector Current	OP300SL	0.80			mA	V _{CE} =5.0V, E ₀ =1.00mW/cm ²⁽⁵⁾
		OP301SL	0.80	2.40		mA	V _{CE} =5.0V, E ₀ =1.00mW/cm ²⁽⁵⁾
		OP302SL	1.80	5.40		mA	V _{CE} =5.0V, E ₀ =1.00mW/cm ²⁽⁵⁾
		OP303SL	3.60	12.0		mA	V _{CE} =5.0V, E ₀ =1.00mW/cm ²⁽⁵⁾
		OP304SL	7.00	21.0		mA	V _{CE} =5.0V, E ₀ =1.00mW/cm ²⁽⁵⁾
		OP305SL	14.0			mA	V _{CE} =5.0V, E ₀ =1.00mW/cm ²⁽⁵⁾
I _{CEO}	Collector Dark Current			1.00	μA	V _{CE} = 10.0V, E ₀ = 0	
V _{BRICEO}	Collector-Emitter Breakdown Voltage	15.0			V	I _C = 100μA	
V _{BRIECO}	Emitter-Collector Breakdown Voltage	5.0			V	I _E = 100μA	
V _{CE(SAT)} ⁽⁴⁾	Collector-Emitter Saturation Voltage	OP300SL,301SL		1.10		V	I _C =0.40mA, E ₀ =1.00mW/cm ²⁽⁵⁾
		OP302SL,304SL,305SL		1.10		V	I _C =1.00mA, E ₀ =1.00mW/cm ²⁽⁵⁾

Typical Performance Curves



Optek reserves the right to make changes at any time in order to improve design and to supply the best product possible.

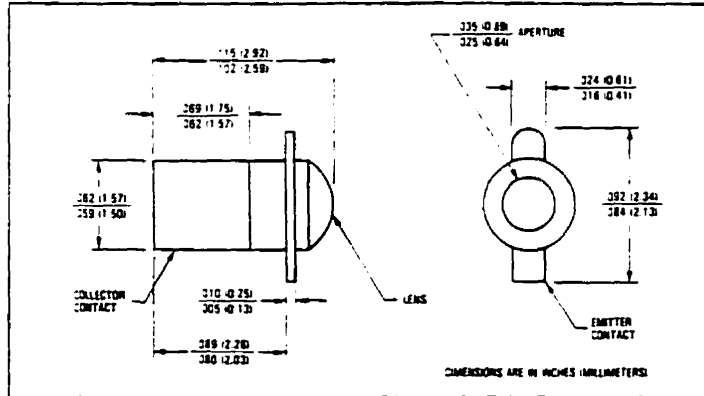
A.2

Product Bulletin OP641SL
July 1989 Replaces January 1985



NPN Silicon Phototransistors

Types OP641SL, OP642SL, OP643SL, OP644SL



Features

- Narrow receiving angle
- Variety of sensitivity ranges
- Enhanced temperature range
- Ideal for direct mounting in PC boards
- Mechanically and spectrally matched to the OP123 and OP223 series devices

Description

The OP641SL series devices consist of NPN silicon phototransistors mounted in hermetically sealed packages. The narrow receiving angle provides excellent on-axis coupling.

Replaces

OP600, OP640 series

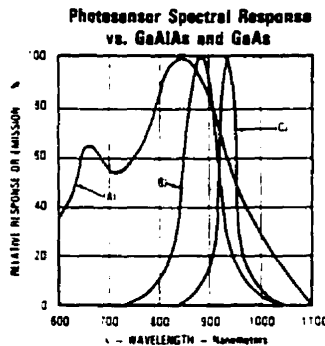
Absolute Maximum Ratings (T_A = 25°C unless otherwise noted)

Collector-Emitter Voltage	25V
Emitter-Collector Voltage	5.0V
Storage Temperature Range	-65°C to +150°C
Operating Temperature Range	-65°C to +125°C
Soldering Temperature (5 sec. with soldering iron)	260°C ⁽¹⁾⁽²⁾
Power Dissipation	50mW ⁽³⁾
Continuous Collector Current	50mA

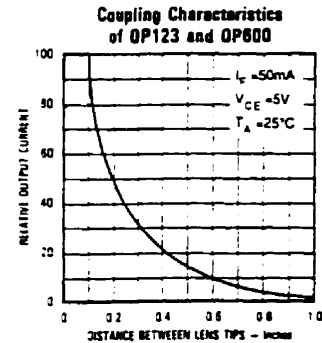
Notes:

- (1) Refer to Application Bulletin 111 which discusses proper techniques for soldering Pill type devices to PC boards.
- (2) RMA flux is recommended. Duration can be extended to 10 sec. max. when flow soldering.
- (3) Derate linearly 0.5mW/°C above 25°C.
- (4) Junction temperature maintained at 25°C.
- (5) Light source is an unfiltered tungsten bulb operating at CT = 2870°K or equivalent infrared source.

Typical Performance Curves



Test Conditions - LED: T_A = T_J = 25°C, I_C = 100 mA, DC - 0.1%, PW = 100 μs
 Peak Wavelength - Al_xIn_{1-x}As - 850 ± 30 nm, In LED
 GaAlAs - 880 ± 20 nm, In LED GaAs - 930 ± 15 nm

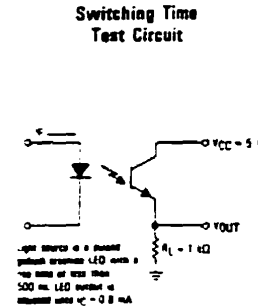
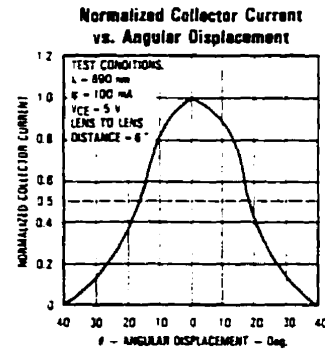
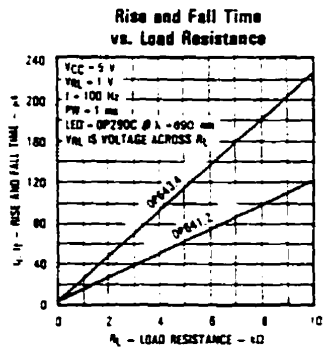
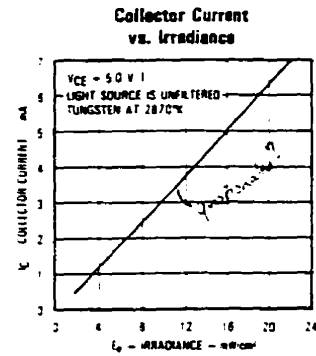
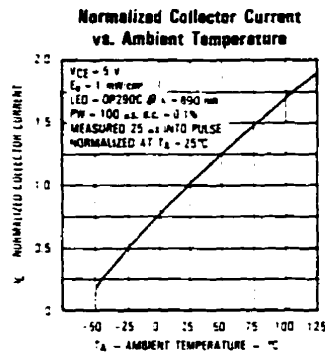
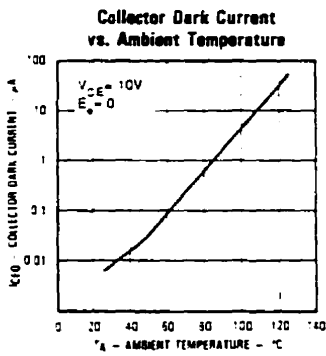


Types OP641SL, OP642SL, OP643SL, OP644SL

Electrical Characteristics (T_A = 25°C unless otherwise noted)

SYMBOL	PARAMETER	MIN	TYP	MAX	UNITS	TEST CONDITIONS
I _{C(ON)} ⁽⁴⁾	On-State Collector Current	OP641SL 0.5 OP642SL 2.0 OP643SL 4.0 OP644SL 7.0	3.0 5.0 8.0 22		mA	V _{CE} = 5.0V, E ₀ = 20mW/cm ²⁽⁵⁾ V _{CE} = 5.0V, E ₀ = 20mW/cm ²⁽⁵⁾ V _{CE} = 5.0V, E ₀ = 20mW/cm ²⁽⁵⁾ V _{CE} = 5.0V, E ₀ = 20mW/cm ²⁽⁵⁾
I _{CEO}	Collector Dark Current			100	nA	V _{CE} = 10.0V, E ₀ = 0
V _{BRICEO}	Collector-Emitter Breakdown Voltage	25			V	I _C = 100μA
V _{BRIECO}	Emitter-Collector Breakdown Voltage	5.0			V	I _E = 100μA
V _{CE(SAT)} ⁽⁴⁾	Collector-Emitter Saturation Voltage		0.40		V	I _C = 0.40mA, E ₀ = 20mW/cm ²⁽⁵⁾
t _r	Rise Time		2.5		μs	V _{CC} = 5.0V, I _C = 0.80mA,
t _f	Fall Time		2.5		μs	R _L = 1.00KΩ, (See Test Circuit)

Typical Performance Curves



Optek reserves the right to make changes at any time in order to improve design and to supply the best product possible.

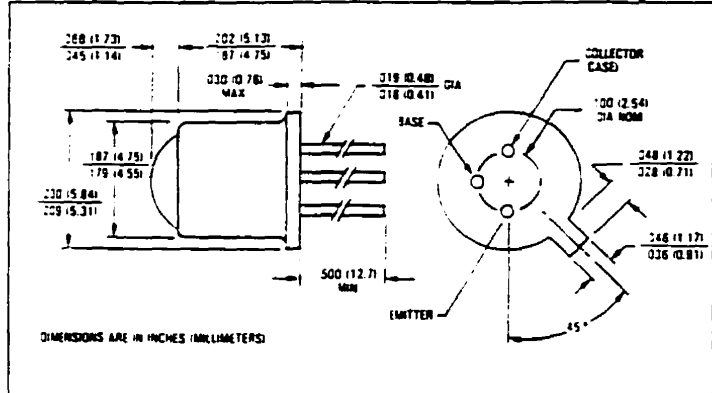
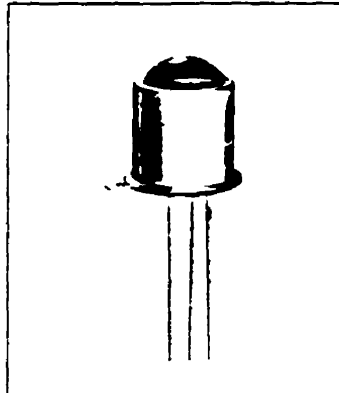
Optek Technology, Inc., 1215 West Crosby Road, Carrollton, Texas 75006 (214) 323-2200 TLX 215849 Fax (214) 323-2396
Printed in USA

A.3

Product Bulletin OP800SL
July 1989 Replaces January 1985



NPN Silicon Phototransistors
Types OP800SL, OP801SL, OP802SL, OP803SL, OP804SL, OP805SL



Features

- Narrow receiving angle
- Variety of sensitivity ranges
- Enhanced temperature range
- TO-18 hermetically sealed package
- Mechanically and spectrally matched to the OP130 and OP231 series of infrared emitting diodes.

Description

The OP800SL series devices consist of an NPN silicon phototransistor mounted in hermetically sealed packages. The narrow receiving angle provides excellent on-axis coupling. TO-18 packages offer high power dissipation and superior hostile environment operation. The base lead is bonded to enable conventional transistor biasing.

Replaces

OP800 and KS251 series

Absolute Maximum Ratings ($T_A = 25^\circ\text{C}$ unless otherwise noted)

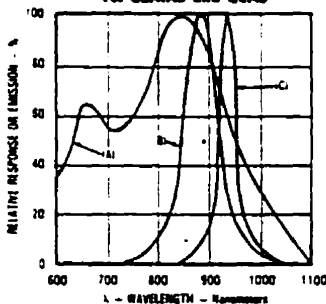
Collector-Base Voltage	30V
Collector-Emitter Voltage	30V
Emitter-Base Voltage	5.0V
Emitter-Collector Voltage	5.0V
Continuous Collector Current	50mA
Storage Temperature Range	-65°C to +150°C
Operating Temperature Range	-65°C to +125°C
Lead Soldering Temperature (1/16 inch (1.6mm) from case for 5 sec. with soldering iron)	260°C ⁽¹⁾
Power Dissipation	250mW ⁽²⁾

Notes:

- 1) RMA flux is recommended. Duration can be extended to 10 sec. max. when flow soldering.
- 2) Derate linearly 2.5mW/°C above 25°C.
- 3) Junction temperature maintained at 25°C.
- 4) Light source is an unfiltered tungsten bulb operating at $C_T = 2870^\circ\text{K}$ or equivalent infrared source.

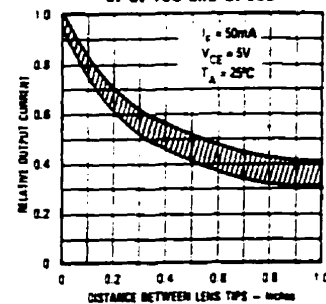
Typical Performance Curves

Spectral Response of OP800-OP805 vs. GaAlAs and GaAs



Test Conditions: LED, $T_A = T_J = 25^\circ\text{C}$, $I_C = 100\text{ mA}$, $V_{CE} = 0.1\text{V}$, $P_D = 100\text{ mW}$
 Peak Wavelength - Al: 650 nm, GaAs: 850 nm, LED: 900 nm, GaAlAs: 880 nm, 20 nm, Al: LED: GaAs: 830 nm, 15 nm

Coupling Characteristics of OP130 and OP800

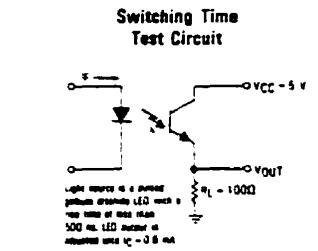
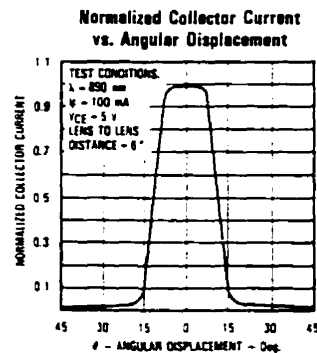
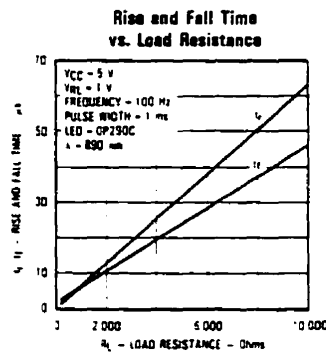
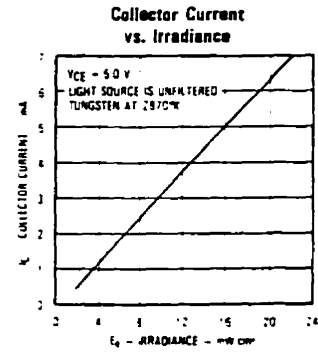
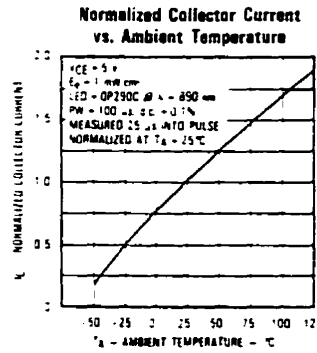
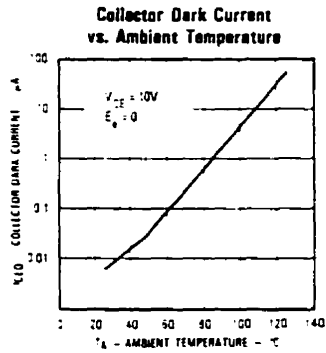


Types OP800SL thru OP805SL

Electrical Characteristics (T_A = 25°C unless otherwise noted)

SYMBOL	PARAMETER	MIN	TYP	MAX	UNITS	TEST CONDITIONS	
I _{C(OH)}	On-State Collector Current	OP800SL	0.50			mA	V _{CE} =5.0V, E _a =5.0mW/cm ² (3)(4)
		OP801SL	0.50	3.0		mA	V _{CE} =5.0V, E _a =5.0mW/cm ² (3)(4)
		OP802SL	2.0	5.0		mA	V _{CE} =5.0V, E _a =5.0mW/cm ² (3)(4)
		OP803SL	4.0	8.0		mA	V _{CE} =5.0V, E _a =5.0mW/cm ² (3)(4)
		OP804SL	7.0	22		mA	V _{CE} =5.0V, E _a =5.0mW/cm ² (3)(4)
		OP805SL	5.0			mA	V _{CE} =5.0V, E _a =5.0mW/cm ² (3)(4)
I _{CEO}	Collector Dark Current			100	nA	V _{CE} = 10.0V, E _a = 0	
V _{BR(CEO)}	Collector-Emitter Breakdown Voltage	30			V	I _C = 100μA	
V _{BR(CBO)}	Collector-Base Breakdown Voltage	30.0			V	I _C = 100μA	
V _{BR(ECO)}	Emitter-Collector Breakdown Voltage	5.0			V	I _E = 100μA	
V _{BR(EB0)}	Emitter-Base Breakdown Voltage	5.0			V	I _E = 100μA	
V _{CE(SAT)}	Collector-Emitter Saturation Voltage		0.4		V	I _C = 0.40mA, E _a = 5.0mW/cm ² (4)	
t _r	Rise Time		2.0		μs	V _{CC} = 5.0V, I _C = 0.80mA,	
t _f	Fall Time		2.0		μs	R _L = 100Ω. See Test Circuit	

Typical Performance Curves



Optek reserves the right to make changes at any time in order to improve design and to supply the best product possible.

Optek Technology, Inc., 1215 West Crosby Road, Carrollton, Texas 75006 (214) 323-2200 TLX 215849 Fax (214) 323-2396

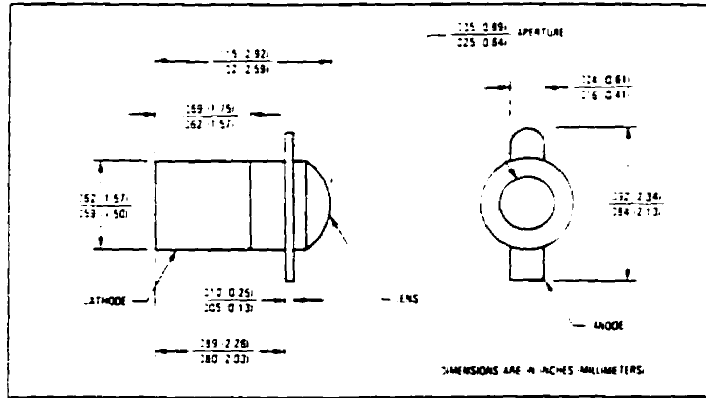
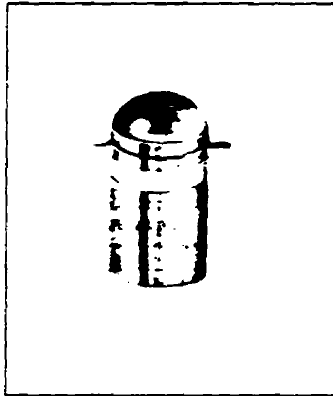
Printed in USA

A.4

Product Bulletin OP900SL
July 1989 Replaces January 1985



PN Junction Silicon Photodiode Type OP900SL



Features

- Narrow receiving angle
- Enhanced temperature range
- Ideal for direct mounting in PC boards
- Fast switching speed
- Mechanically and spectrally matched to the OP123 series devices
- Linear response vs irradiance

Description

The OP900SL consists of a PN junction silicon photodiode mounted in a miniature, glass lensed hermetically sealed "Pill" package. The lensing effect allows an acceptance half angle of 18° measured from the optical axis to the half power point.

Replaces

OP900 series

Absolute Maximum Ratings (T_A = 25°C unless otherwise noted)

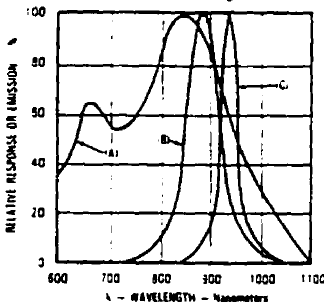
Reverse Voltage	100V
Storage Temperature Range	-65°C to +150°C
Operating Temperature Range	-65°C to +125°C
Soldering Temperature (5 sec. with soldering iron)	260°C ⁽¹⁾
Power Dissipation	50mW ⁽²⁾

Notes:

- (1) RMA flux is recommended. Duration can be extended to 10 sec. max. when flow soldering
- (2) Derate linearly 0.5mW/°C above 25°C
- (3) Junction temperature maintained at 25°C
- (4) Light source is an unfiltered tungsten bulb operating at CT = 2870°K or equivalent infrared source.

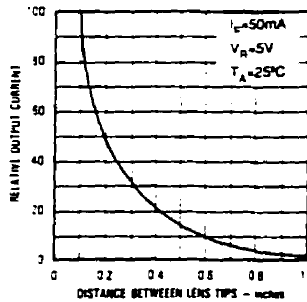
Typical Performance Curves

Spectral Response and Emission vs. Wavelength



Fast Continuous LED: T_A = T_J = 25°C, I_F = 100 mA
 DC = 0.1%, PW = 100 μs
 Peak Wavelength = 1.0 μm (STB) = 850 ± 20 nm, (B) LED
 GaAs = 800 ± 20 nm, (C) LED GaAs = 820 ± 15 nm

Coupling Characteristics of OP123 and OP900

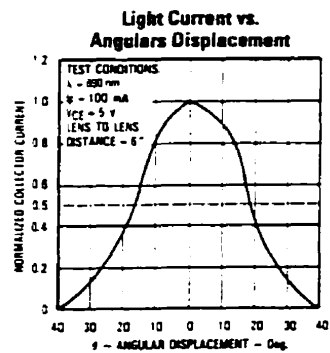
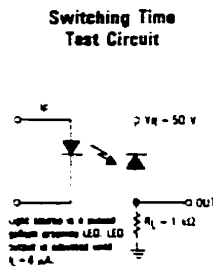
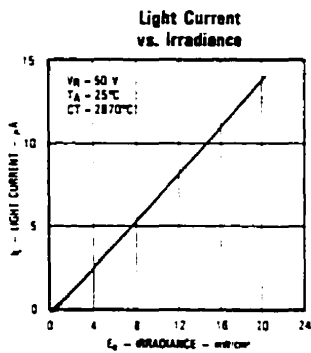
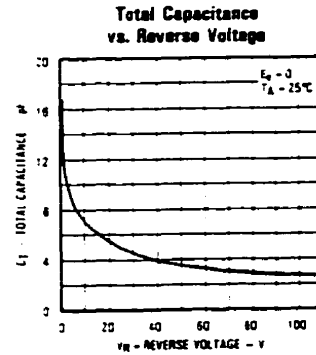
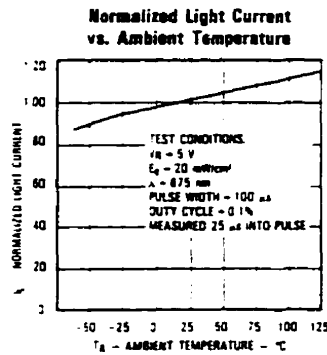
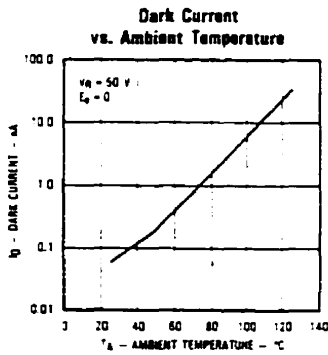


Type OP900SL

Electrical Characteristics (T_A 25°C unless otherwise noted)

SYMBOL	PARAMETER	MIN	TYP	MAX	UNITS	TEST CONDITIONS
I _L	Light Current	8.0	14.0		μA	V _R =10.0V, E _a =20mW/cm ² (3)(4)
I ₀	Dark Current			10.0	nA	V _R =10.0V, E _a =0 ⁽³⁾
V _{BR} /I _R	Reverse Voltage Breakdown	100	150		V	I _R = 100μA
t _r	Rise Time		100		ns	V _R = 50V, I _L = 8.0μA
t _f	Fall Time		100		ns	R _L = 1.00kΩ. (See Test Circuit)

Typical Performance Curves



Optek reserves the right to make changes at any time in order to improve design and to supply the best product possible.

Optek Technology, Inc., 1215 West Crosby Road, Carrollton, Texas 75006 (214) 323-2200 TLX 215849 Fax (214) 323-2396

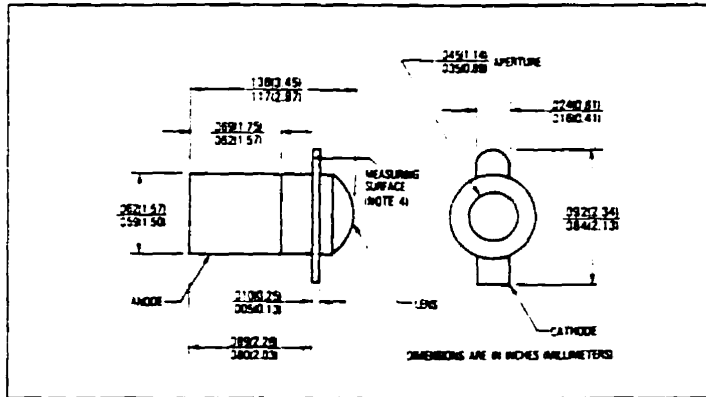
Printed in USA

A.5

Product Bulletin OP223
July 1989 Replaces January 1985



GaAlAs Hermetic Infrared Emitting Diodes Types OP223, OP224



Features

- Narrow irradiance pattern
- Enhanced temperature range
- Small package size permits high device density mounting
- Mechanically and spectrally matched to the OP640SL and OP300SL series devices
- Significantly higher power output than GaAs at equivalent drive currents
- Wavelength matched to silicon s peak response

Description

The OP223 and OP224 devices are 890nm gallium aluminum arsenide infrared emitting diodes mounted in hermetically sealed "Pill" type packages. The narrow irradiance pattern provides high on-axis intensity for excellent coupling efficiency.

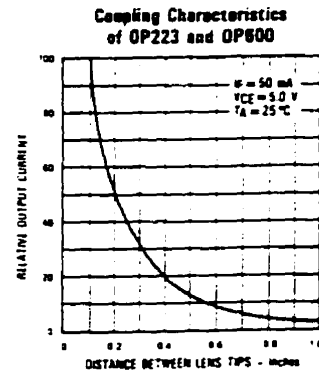
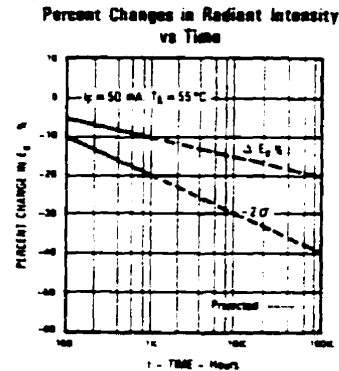
Absolute Maximum Ratings ($T_A = 25^\circ\text{C}$ unless otherwise noted)

Reverse Voltage	2.0V
Continuous Forward Current	100mA
Peak Forward Current (2 μs pulse width, 0.1% duty cycle)	1.0A
Storage Temperature Range	-65°C to +150°C
Operating Temperature Range	-55°C to +125°C
Soldering Temperature (5 sec. with soldering iron)	260°C ^(1,2)
Power Dissipation	150mW ⁽³⁾

Notes:

- 1) Refer to Application Bulletin 111 which discusses proper techniques for soldering Pill type devices into PC boards.
- 2) RMA flux is recommended. Duration can be extended to 10 sec. max. when flow soldering.
- 3) Derate linearly 1.50mW/°C above 25°C.
- 4) E_{measured} is measured using a 0.031" (0.787mm) diameter apertured sensor placed 0.50" (12.7mm) from the mounting plane. E_{measured} is not necessarily uniform within the measured area.

Typical Performance Curves



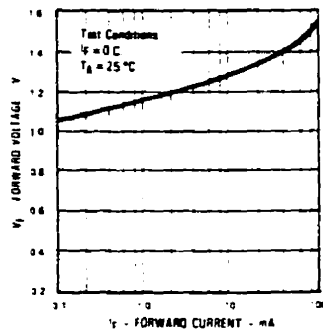
Types OP223, OP224

Electrical Characteristics (T_A = 25°C unless otherwise noted)

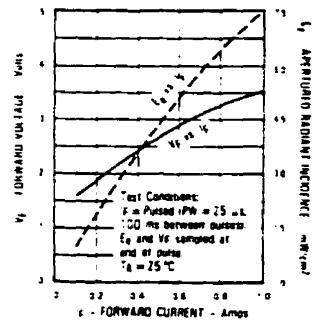
SYMBOL	PARAMETER	MIN	TYP	MAX	UNITS	TEST CONDITIONS
E _{APR}	Apertured Radiant Incidence	OP223 OP224	1.00 3.50		mW/cm ² mW/cm ²	I _F = 50mA ⁽⁴⁾ I _F = 50mA ⁽⁴⁾
V _F	Forward Voltage			1.80	V	I _F = 50mA
I _R	Reverse Current			100	μA	V _R = 2.0V
λ _P	Wavelength at Peak Emission		890		nm	I _F = 10mA
Δλ _{HP}	Spectral Bandwidth Between Half Power Points		80		nm	I _F = 10mA
Δλ _P /ΔT	Spectral Shift with Temperature		-0.18		nm/°C	I _F = Constant
θ _{HP}	Emission Angle at Half Power Points		24		Deg.	I _F = 50mA
t _r	Output Rise Time		500		ns	I _{F(PK)} = 100mA, PW = 10.0μs
t _f	Output Fall Time		250		ns	D.C. = 100%

Typical Performance Curves

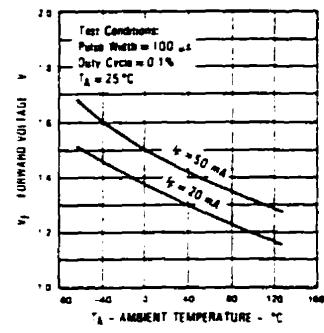
Forward Voltage vs Forward Current



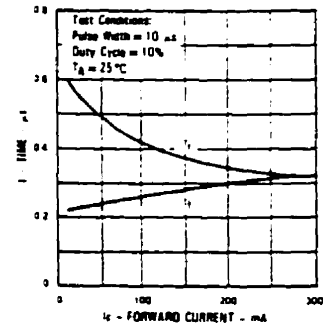
Forward Voltage and Radiant Incidence vs Forward Current



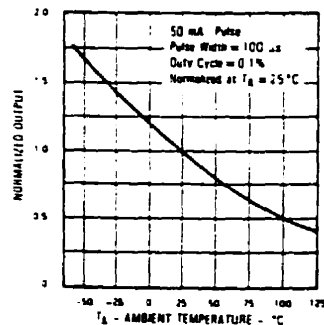
Forward Voltage vs Ambient Temperature



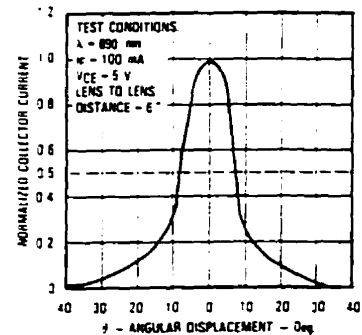
Rise Time and Fall Time vs Forward Current



Normalized Power Output vs Ambient Temperature



Relative Radiant Intensity vs Angular Displacement



Optek reserves the right to make changes at any time in order to improve design and to supply the best product possible.

Optek Technology, Inc., 1215 West Crosby Road, Carrollton, Texas 75006 (214) 323-2200 TLX 215849 Fax (214) 323-2396

Printed in USA

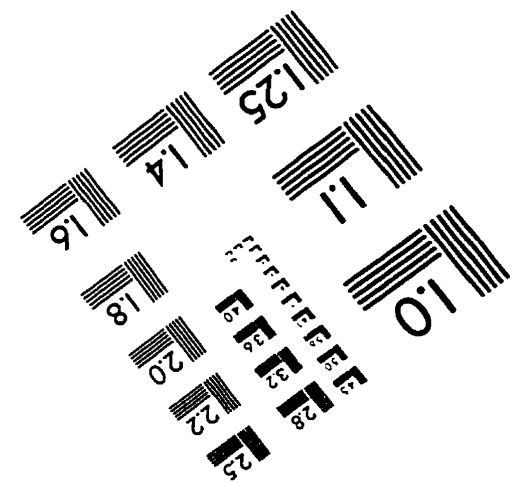
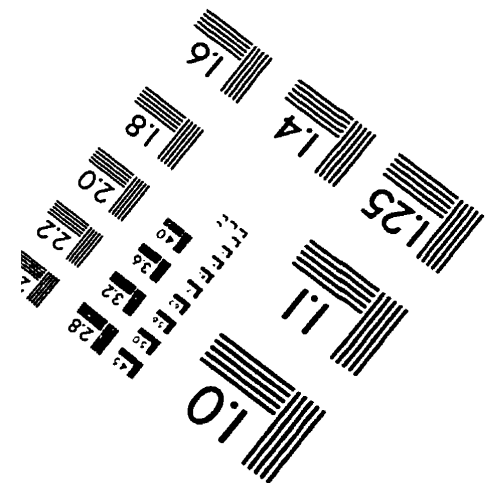
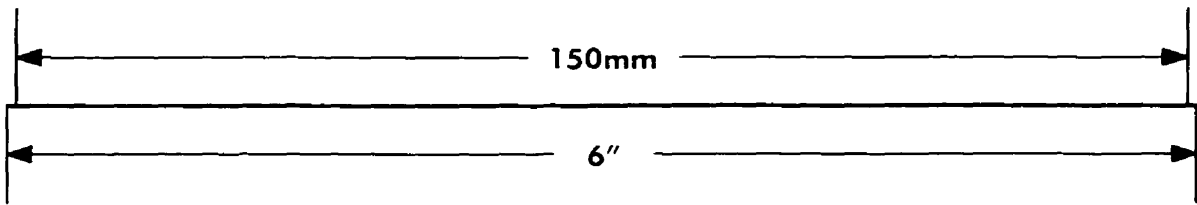
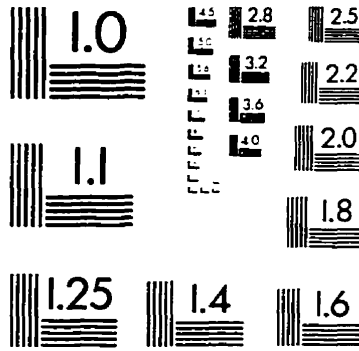
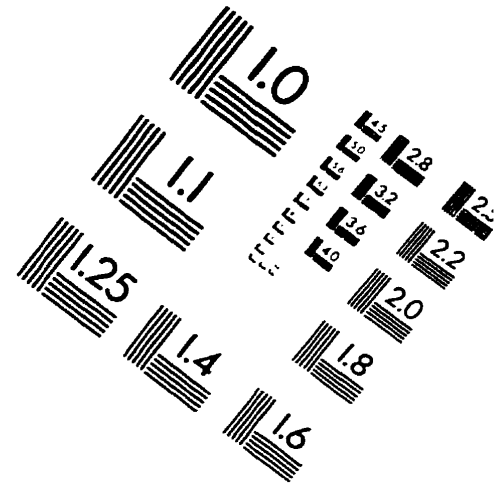
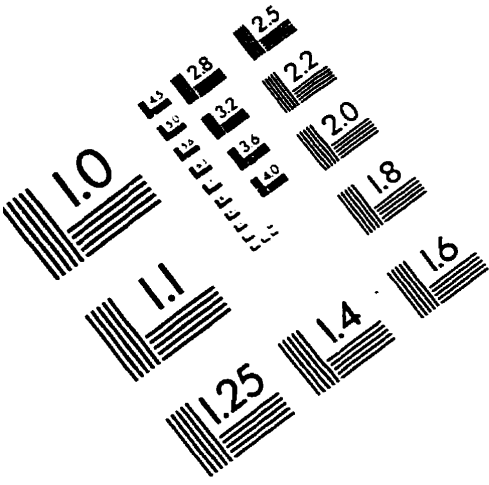
Bibliography

- [1] C. Archibald and C. Merritt. Pose determination of known objects from sparse range images. In *Proceedings of an International Conference. Intelligent Autonomous Systems 2*, volume 1, pages 185–95. Amsterdam, Netherlands, Dec 1990. IOS.
- [2] D.J. Balek and R.B. Kelley. Using gripper mounted infrared proximity sensors for robot feedback control. In *Proc. IEEE Int. Conf. Robotics and Automation*, pages 282–7. Silver Spring, MD, Mar 1985.
- [3] A. K. Bejczy. Effect of hand-based sensors on manipulator control performance. *Mechanism and Machine Theory*, 12(5):547–67, 1977.
- [4] A. Bonen, M. Parent, K.C. Smith, and B. Benhabib. Development of a robust electro-optical proximity sensor. In *IEEE/RSJ Intelligent Robots and Systems*, pages 986–990, Yokohama, Japan, Jul 1993.
- [5] J.Y. Catros, A. Dore, B. Espiau, and J.Y. Yclon. Automatic grasping using infrared sensors. In *Proceedings of the 8th International Symposium on Industrial Robots*, pages 132–42. Stuttgart, Germany, May 1978.
- [6] E. Cheung and V. Lumelsky. Development of sensitive skin for a 3d robot arm operating in an uncertain environment. In *Proc. IEEE Int. Conf. Robotics and Automation*, pages 1056–1061, Piscataway, NJ, 1989.

- [7] H.A. Ernst. *MH-1, a computer-operated mechanical hand*. PhD thesis, M.I.T., Dec 1961.
- [8] Thomas M. Frederiksen. *Intuitive IC Op Amps*. National Semiconductor Corporation, Santa Clara, CA, 1984.
- [9] G. Hirzinger. Multisensory shared autonomy and tele-sensor-programming-key issues in space robotics. In *IAS-2 Int. Conf. on Intelligent Autonomous Systems*, pages 1-29, Pittsburgh, Pa, Feb 1993.
- [10] Optek Technology Inc. *Emitter and Photosensor Chips Data Book*. Optek Technology Inc., Carrollton, TX, 1990.
- [11] A.R. Johnston. Proximity sensing technology for manipulator end effectors. *Mechanism and Machine Theory*, 12:95-109, 1977.
- [12] S.M. Juds. *Photoelectric Sensors and Controls*. Marcel Dekker, Inc., NY, 1988.
- [13] T. Kanade and T. Sommer. An optical proximity sensor for measuring surface position and orientation for robot manipulation. In M. Brady and R. Paul, editors, *Robotics Research: The First International Symposium*, pages 547-563. The MIT Press, 1984.
- [14] A.J. Koivo and Nasser Houshangi. Real-time vision feedback for servoing robotic manipulator with self-tuning controller. *IEEE Trans. Systems, Man, and Cybernetics*, 21(1):134-42, Jan.-Feb. 1991.
- [15] L. Korba, S. Elgazzar, and T. Welch. Active infrared sensors for mobile robots. *IEEE Trans. Instrumentation and Measurement*, 43(2):283-7, Apr 1994.
- [16] Y.F. Li. Characteristics and signal processing of a proximity sensor. *Robotica*, 12:335-41, 1994.
- [17] J. Marszalec. A proximity sensing system for an intelligent optically-powered robot gripper. *I. J. Optoelectronics*, 4(3/4):343-355, May-Aug 1989.

- [18] R. Masuda. Multifunctional optical proximity sensor using phase modulation. *J. Robotic Systems*, 3(2):137-147, 1986.
- [19] T.G. Murphy, D.M. Lyons, and A.J. Hendriks. Visually guided stable grasping with a multi-fingered robot hand: a behavior-based approach. *Proceedings of the SPIE - The International Society for Optical Engineering*, 2056:252-63, 1993.
- [20] T. Okada and U. Rembold. Proximity sensor using a spiral-shaped light-emitting mechanism. *IEEE Trans. Robotics and Automation*, 7(6):798-805, Dec 1991.
- [21] O. Partaatmadja, B. Benhabib, and A. Goldenberg. Analysis and design of a robotic distance sensor. *J. Robotic Systems*, 10(4):427-445, 1993.
- [22] G. Petryk and M. Buehler. Dynamic object localization via a proximity sensor network. In *IEEE/SICE/RSJ Int. Conf. Multisensor Fusion and Integration for Intelligent Systems*, pages 337-341, Washington, DC, Dec 1996.
- [23] G. A. Petryk. Dynamic object localization via a proximity sensor network. M.Eng. Thesis, McGill University, Aug 1996.
- [24] K. Rao, G. Medioni, H. Liu, and G.A. Bekey. Shape description and grasping for robot hand-eye coordination. *IEEE Control Systems Magazine*, 9(2):22-9, Feb. 1989.
- [25] G. Roth and D. O'Hara. A holdsite method for parts acquisition using a laser rangefinder mounted on a robot wrist. *Advances in CAD/CAM and robotics: NRC contributions*, pages 293-9, May 1987.
- [26] V.D. Sanchez and G. Hirzinger. Learning how to grasp under supervision. In *IJCNN International Joint Conference on Neural Networks*, pages 769-74, New York, NY, Jun 1992. IEEE.
- [27] S.A. Stansfield. Robotic grasping of unknown objects: a knowledge-based approach. *Int. J. Robotics Research*, 10(4):314-26, Aug 1991.

IMAGE EVALUATION TEST TARGET (QA-3)



APPLIED IMAGE, Inc
 1653 East Main Street
 Rochester, NY 14609 USA
 Phone: 716/482-0300
 Fax: 716/288-5989

© 1993, Applied Image, Inc., All Rights Reserved